

In Situ Characterization Of Single-Wall Carbon Nanotube Thin Film Growth Using
The Polarization Properties Of Tilted Fibre Bragg Gratings

by

MOHAMMAD ZAHIRUL ALAM

A thesis submitted to the Faculty of Graduate and Postdoctoral
Affairs in partial fulfillment of the requirements for the degree of

Master of Applied Science

in

Electrical and Computer Engineering

Ottawa-Carleton Institute of Electrical and Computer Engineering
Department of Electronics
Carleton University
Ottawa, Ontario

©2012

Mohammad Zahirul Alam



Library and Archives
Canada

Published Heritage
Branch

395 Wellington Street
Ottawa ON K1A 0N4
Canada

Bibliothèque et
Archives Canada

Direction du
Patrimoine de l'édition

395, rue Wellington
Ottawa ON K1A 0N4
Canada

Your file Votre référence

ISBN: 978-0-494-93494-4

Our file Notre référence

ISBN: 978-0-494-93494-4

NOTICE:

The author has granted a non-exclusive license allowing Library and Archives Canada to reproduce, publish, archive, preserve, conserve, communicate to the public by telecommunication or on the Internet, loan, distribute and sell theses worldwide, for commercial or non-commercial purposes, in microform, paper, electronic and/or any other formats.

The author retains copyright ownership and moral rights in this thesis. Neither the thesis nor substantial extracts from it may be printed or otherwise reproduced without the author's permission.

AVIS:

L'auteur a accordé une licence non exclusive permettant à la Bibliothèque et Archives Canada de reproduire, publier, archiver, sauvegarder, conserver, transmettre au public par télécommunication ou par l'Internet, prêter, distribuer et vendre des thèses partout dans le monde, à des fins commerciales ou autres, sur support microforme, papier, électronique et/ou autres formats.

L'auteur conserve la propriété du droit d'auteur et des droits moraux qui protègent cette thèse. Ni la thèse ni des extraits substantiels de celle-ci ne doivent être imprimés ou autrement reproduits sans son autorisation.

In compliance with the Canadian Privacy Act some supporting forms may have been removed from this thesis.

While these forms may be included in the document page count, their removal does not represent any loss of content from the thesis.

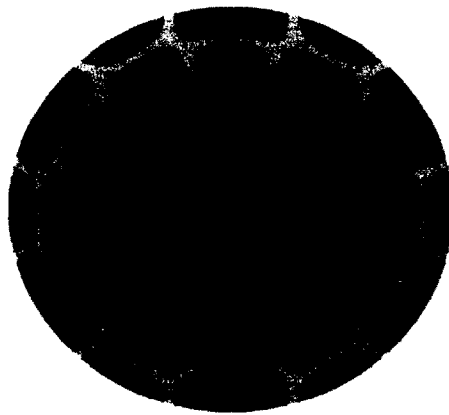
Conformément à la loi canadienne sur la protection de la vie privée, quelques formulaires secondaires ont été enlevés de cette thèse.

Bien que ces formulaires aient inclus dans la pagination, il n'y aura aucun contenu manquant.

Canada

IN SITU CHARACTERIZATION OF SINGLE-WALL CARBON
NANOTUBE THIN FILM GROWTH USING THE POLARIZATION
PROPERTIES OF TILTED FIBRE BRAGG GRATINGS

MOHAMMAD ZAHIRUL ALAM



Master of Applied Science (MASc)
Department of Electronics
Carleton University

September 28, 2012

Mohammad Zahirul Alam: *In Situ Characterization Of Single-Wall Carbon Nanotube Thin Film Growth Using The Polarization Properties Of Tilted Fibre Bragg Gratings*, Master of Applied Science (MAsc),
SUPERVISOR: Professor Jacques Albert
LOCATION: Ottawa, Canada

To my teachers, parents, and brother.

ABSTRACT

In this thesis, we explore the polarization dependent properties of the tilted fibre Bragg gratings for the in situ characterization of single-wall carbon nanotubes deposited on the cladding of a fibre using a layer-by-layer deposition technique.

First, we describe an exact analytical and fully-vectorial solution of the cladding modes of a standard telecom fibre. The cladding of an optical fibre is a multimode wave guide and can support many thousands of modes. We present an algorithm to efficiently solve the complex propagation constants of the cladding modes. Our analysis shows that based on the polarization properties, the cladding modes can be classified into two categories: dominant radial and dominant azimuthal. The formalism is then extended to an arbitrary four layer fibre structure.

Next, we present the polarization dependent coupling properties of the tilted fibre Bragg gratings: 1d periodic index modulation in the core of an optical fibre with a tilt with respect to the fibre axis that enhances coupling of light from the linearly polarized core mode to the contra-directional cladding modes. We prove that by controlling the orientation of the core mode electric vector with respect to the plane of the tilt of the gratings, one can couple either only to the radially polarized or to the azimuthally polarized cladding modes. This is the first ever comprehensive theoretical description of the polarization dependent guided cladding mode coupling properties of the tilted fibre Bragg gratings.

Finally, we report the first ever effort to investigate the polarization dependent optical properties of randomly oriented single-wall carbon nanotubes on the nanometre scale. The carbon nanotube films are grown on the cladding of the fibre using a layer-by-layer technique. Weakly tilted Bragg gratings in the core of the fibre allows in situ characterization of the film. We report that such a film exhibits strong polarization dependent loss: radially polarized cladding modes experience up to five times more loss than azimuthally polarized modes for films of up to tens of nanometres thickness. This is the first ever observation of the polarization dependent loss on a nanometre scale thin randomly oriented carbon nanotube film. However, the film exhibits no birefringence and the optical constants are strongly thickness dependent.

*I don't know half of you half as well as I should like;
and I like less, than half of you half as well as you deserve.*

— J. R. R. Tolkien, *The Fellowship of the Ring*

ACKNOWLEDGMENTS

I want to use these lines to thank and acknowledge all the people who made this thesis possible.

First, I would like to thank Dr. Michael Jakubinek, SIMS, National Research Council. He devised the technique of depositing carbon nanotubes on the fibre. He has spent countless hours in optimizing the process, confirming the deposition, taking images, and measuring thickness. Hence this thesis would not have been possible without his contribution and no gratitude would suffice.

I thank all my colleagues specially Aleksander Beliaev and Lingyun Xiong for the countless hours of discussions and help on matters involving both science and life; Dr. Liyang Shao for the help in the laboratory during my early days in the group; Dr. Yang Zhang and Wenjun Zhou for helping me with the TFBG fabrication; and the indispensable Ms. Albane Laronche without whom the much of my hands-on learning in the lab would have been impossible.

I would now like to thank some of my friends specially Dr. Nasim Sydee and Sylvia Jalal. They have been with me and gave constant inspiration and guidance during some of the most difficult time of my life. The demand of the research often dragged me down. Guilio Vampa, Chris Oosterhof, Laurence Boisvert, and Lieneke Bakker were my support during these times. The calculation of the coupling properties of the TFBG would not have been completed without the generous hospitality of Erfan Chowdhury in Montreal. The writing of this thesis was hard, and would not have been possible without the generosity and hospitality of my friend of many years Sanjid Anik in Toronto. A special thanks to Sanjid's friend Dominc Wang who lent me his bike during my stay in Toronto so that I can go the Ryerson library to write.

As a supervisor and a teacher Professor Jacques Albert sets a standard that I will always strive to attain. He took me to his group as an undergrad when few would have. I have been truly lucky to have learned from one so generous and so wise. I owe him every success over the last three years. He inspired me with kind words when the going was tough, and reminded me of the high standard one must attain and gave me the confidence through constant encouragement. Thanks for putting up with my tardiness, Jacques.

A special thanks to Dr Pavan Gunupudi for convincing me to enrol in the graduate program. It was a wonderful experience.

Finally, I am grateful to Carleton University for the financial support, and to the NSERC for an Alexander Graham Bell Canada Graduate Scholarship M.

CONTENTS

1	INTRODUCTION	1
2	VECTOR MODES AND EQUATIONS	7
2.1	The Core mode in a three-layered structure	8
2.2	Cladding Mode in a Three-layer Structure	10
2.2.1	Hybrid Mode Field Expressions and Dispersion Relation	11
2.2.2	TE and TM Mode Field Expressions	16
2.3	Solving the dispersion relation	17
2.3.1	For Lossless Case	17
2.3.2	For Lossy Cases	20
2.4	Mode field and the Polarization Properties	24
2.5	Cladding Mode in a four-layer structure	27
3	COUPLING COEFFICIENT AND TRANSMISSION RESPONSE	33
3.1	Coupling Coefficient	33
3.2	Transmission Response	39
3.3	Comments	46
4	CHARACTERIZATION OF THE SWCNT COATING ON OPTICAL FIBRE	49
4.1	CNT deposition	49
4.2	Analysis	54
5	CONCLUSION	65
	BIBLIOGRAPHY	67
A	APPENDIX	75

LIST OF FIGURES

Figure 1	The generalized three layer fibre structure	8
Figure 2	A graphical method for solving the eigenvalue equation	18
Figure 3	Typical solutions of the eigenvalue equation	19
Figure 4	The even and the odd azimuthal order solutions make nearly degenerate modes	19
Figure 5	The variation in the effective index as a function of n_3	20
Figure 6	The imaginary part of the guide index for azimuthal order $l = 0, 1$ $n_3 = 1.3 + i 0.5$	21
Figure 7	$\text{Im } n_{\text{eff}}$ for EH modes	22
Figure 8	Plots of the local Poynting vector magnitudes as a function of radius for few lowest order modes	23
Figure 9	Plots of the fraction of the total power carried by fields of cladding modes in the core	25
Figure 10	The vector electric field plots of transverse modes.	26
Figure 11	The intensity and the vector field plots of hybrid modes in the cladding.	27
Figure 12	The fraction of total power carried by the radial component of each mode.	28
Figure 13	The generalized four layer fibre structure	29
Figure 14	Intensity distribution of the TE_{01} cladding mode in a four layer structure	31
Figure 15	Configuration of the X-tilted gratings.	33
Figure 16	10 deg grating assisted modal overlap.	35
Figure 17	Coupling coefficient for the P-polarized core mode.	37
Figure 18	Coupling coefficient for the S-polarized core mode.	38
Figure 19	4° TFBG S-polarized transmission response	40
Figure 20	10° TFBG S-polarized transmission response	42
Figure 21	10° TFBG resonance exhibits polarization dependent resonance split	43
Figure 22	4° TFBG resonance depth as a function of n_3	44
Figure 23	The 10° TFBG resonance movement as a function of n_3	46
Figure 24	SWCNT deposition on the fibre surface	50
Figure 25	Measuring TFBG response	51
Figure 26	Monitoring the CNT deposition	52
Figure 27	SEM images of the CNT layer	53

Figure 28	Measuring the relative position of the cladding modes with respect to the Bragg resonance	56
Figure 29	The normalized change of the wavelength position of resonances during dipping cycles	57
Figure 30	Method for calculating nanotubes' thickness and real part of the index	58
Figure 31	Thickness and index as a function of the dipping cycle	59
Figure 32	Extracting $\text{Im}n_{\text{CNT}}$	62
Figure 33	CNT index as a function of thickness	63

NOMENCLATURE

β	Propagation constant, $2\pi/\lambda$
χ_3	Third Order Susceptibility
δn	Grating induced ac index modulation, $2n_1 \sigma v$
δ	Momentum mismatch or detuning vector, $\beta_u + \beta_v - 2K_g \cos \theta$
$\Delta\epsilon$	Grating induced dielectric perturbation
ϵ_0	Free space permittivity
ϵ_i	Permittivity of i'th layer
$\Gamma[l]$	Gamma function, $(l-1)!$
$\hat{r}, \hat{\phi}, \hat{z}$	Unit vector in Cylindrical coordinates
Λ	Grating period
λ	Wavelength
λ_B	Bragg wavelength
λ_D	Design wavelength
ω	Angular frequency
ϕ	Azimuthal angle with respect to the X-axis
Φ_i, Ψ_i	Debye potential associated with the i'th layer
ψ	$0, \pi/2$, Converts Odd modes to Even modes and vice versa
σ	Slowly varying envelope of the grating induced index modulation

σ_1	iln_{eff}/Z_0
σ_2	$iln_{eff}Z_0$
θ	Tilt angle of the gratings
a_1	Core radius
a_2	Cladding radius
c	The speed of light
E_{cl}^{lm}	Hybrid mode field normalization coefficient
$E_{cl}^{TE,m}$	Normalization constant for TE_{0m} mode
$E_{cl}^{TM,m}$	Normalization constant for TM_{0m} mode
E_{co}^{11}	Core mode normalization constant
EH	Hybrid Magnetic Mode
HE	Hybrid Electric Mode
I_l	Modified Bessel function of the first kind of order l
J_l	Bessel function of first kind of order l
k	Wave number = $\frac{2\pi}{\lambda}$
K_g	π/Λ
K_l	Modified Bessel function of the second kind of order l
κ_{12}^t	Transverse coupling coefficient between mode 1 and 2
l	Azimuthal order
n_1	Core index
n_2	Cladding index
n_g	Group index
n_i	Index of the i 'th layer
TE	Transverse Electric
TM	Transverse Magnetic
u_i	Phase parameter of a cladding mode in the i 'th layer = $\frac{2\pi}{\lambda} \sqrt{n_i^2 - n_{eff}^2}$
u_{core}	Core mode phase parameter in the core
v	Fringe visibility

v_g	Group velocity
w_i	Phase parameter of a cladding mode in the i'th layer = $\frac{2\pi}{\lambda} \sqrt{n_{eff}^2 - n_i^2}$
w_{core}	Core mode phase parameter in the cladding
Z_0	Free space impedance
APTES	3-Aminopropyltriethoxysilane
CNT	Carbon Nanotubes
DMF	N, N-dimethylformamide
SEM	Scanning electron microscope
SWCNT	Single-wall Carbon Nanotube
TFBG	Tilted Fibre Bragg Gratings

INTRODUCTION

Single-wall carbon nanotubes (SWCNT) are rolled up forms of graphene, a two dimensional honey comb structure of carbon, and were first discovered by Iijima [1, 2]. Carbon nanotubes (CNT) can be metallic or semiconducting depending on the orientation of the honey comb structure of the carbon atoms with respect to the tube axis, i.e. chirality. Nanotubes have exceptional electrical, optical, thermal, and mechanical properties [3]. The direct bandgap semiconducting nanotubes are in the very centre of the next generation transistor research [4–6]. Very recently researchers have reported the manufacturing of sub-10 nm CNT transistor which exhibits “unprecedented performance” and outperforms the best silicon based devices in key metrics, e.g. diameter-normalized current density at a low operating voltage of 0.5V, and small inverse sub-threshold slope of 94mV/decade [7]. Carbon nanotubes also have exceptional optical properties. Researchers have studied nano-scale light emitters, detectors, antenna, and photovoltaic devices made from the semiconducting nanotubes[3]. Carbon nanotubes have also been found to have exceptional nonlinear optical properties due to the resonant excitonic dynamics [8, 9]. In fact, the real part of the third order nonlinear susceptibility ($\text{Re}[\chi_3]$) has been theoretically predicted to be as high as 10^{-6} esu which is eight orders of magnitude higher than that of the silica glass [10]. We are interested in the fibre based linear and nonlinear optical devices utilizing the exceptional electrical and optical properties of the Single-wall Carbon nanotube. Hence we limit the following discussions within this scope.

The χ_3 is a complex quantity and is present in all materials. It gives rise to the intensity dependent refractive index change - known as the Kerr effect, saturable absorption, third harmonic generation, four-wave mixing, optical phase conjugation, optical bistability etc. [11]. Researchers have extensively studied Carbon nanotube based fibre lasers for ultrashort-pulse generation through mode-locking and Q-switching [12–20]. For these pulsed fibre laser applications, researchers have used the saturable absorption property of CNT film or CNT-polymer composite structure. Saturable absorption is a third order nonlinear process which reduces the absorption of high intensity light. Nanotubes exhibit two distinct wavelength dependent ultrafast saturation absorption recovery times of 1ps [10] and 110fs [21], a saturable absorption modulation depth of ~12% [16] and a low saturation intensity of $\sim 12.5\text{MW/cm}^2$ [10]. Exploiting these exceptional properties mode-locked laser with pulses as short as 113fs with 33.5 nm

spectral width has been reported [17]. Researchers have also incorporated carbon nanotubes in fibre structures for applications in wavelength conversion using 10Gb/s Non-Return-to-zero signal [20, 22] in four wave mixing process, in designing novel Kerr shutter for optical switching [23], and in nonlinear polarization rotators [22].

In all of these applications researchers have used two nanotube-light interaction mechanisms: either by placing a very thin nanotube or nanotube-composite perpendicular to the path of the optical field, or through a guided wave mechanism for evanescent interaction using tapered or D-shaped fibre. However optical power greater than few tens of mW damages the CNT film. For CNT-polymer composite structures this damage threshold is even lower, which fundamentally limits the long term stability and the maximum obtainable power [24]. Additionally, for applications such as wavelength conversion, the long interaction length between light and the CNT becomes important since the efficiency in these processes scales with the length of interaction. Hence high linear absorption and the damage threshold limit the use of the nanotube perpendicular to the path of the optical field. By using tapered and D-shaped fibre both problem can be circumvented since in these cases light interacts with the nanotube through the evanescent field, to the detriment of mechanical robustness, and additional processing, like polishing for the D-shaped fibre. It is in these contexts our group has become interested in the tilted fibre Bragg gratings (TFBG) mediated nonlinear interaction using the standard telecom fibre with the carbon nanotubes deposited on the cladding of the fibre. This technique gives precise control in tailoring the interaction between light and the CNT film by controlling the coupling mechanism using tilted gratings, without the need of any mechanical reshaping of the fibre.

In 2011, members of our research group have published- as a proof of concept- the results of two studies involving tilted Bragg gratings mediated nonlinear optical interactions in standard telecom fibre with Single-wall carbon nanotube deposited on the cladding of the fibre. In the first paper, Villanueva et al. have used a pico second pump-probe pulse experiment to show the ultrafast modulation of the probe beam through the nonlinear modification of the TFBG spectral response [25]. In the second paper, Shao et al. have shown the wavelength conversion through a four-wave mixing process in a TFBG inscribed fibre [26]. Both of these experiments have shown that indeed, the TFBG inscribed fibre can be an alternative technology in any fibre based nanotube mediated nonlinear optical interactions. To further improve the results of these experiments or to exploit TFBG in other nanotube based nonlinear applications we need to understand the fundamental interaction mechanisms between the TFBG response and the CNT deposited on the cladding of the fibre.

TFBGs are special kind of fibre Bragg gratings, in which the gratings are weakly tilted with respect to the fibre axis. The Fibre Bragg grating (FBG) is a fundamental technology in the modern optical communication[27] and many fibre based sensing platforms. Typically, the grating is written by side-exposing the fibre core to a UV beam diffracted off a phase mask [28]. Due to the photosensitive nature of the germanium doped core [29], the diffracted UV beam pattern gets inscribed into the core through the weak modulation of the core index, leaving the cladding unchanged. A tilt with respect to the normal of the incoming UV beam allows inscription of the Bragg gratings with a tilt with respect to the fibre axis [30].

A tilted fibre Bragg grating (TFBG) in a single mode fibre couples forward propagating core mode light to the backward propagating Bragg mode, the backward propagating cladding modes, and to the radiation modes [31]. The tilt enhances coupling to cladding modes. Researchers have utilized these unique properties in designing gain flatteners [32], gain equalizers [33], in-fibre polarizers [34], fibre based mode converters [35], and in-fibre spectrometers [36]. Laffont and Ferdinand reported the first evanescent refractive index sensor using TFBG in [37]. Since then researchers have reported a number of other sensing modalities using TFBG in refractive index sensing [38, 39], bend sensor [40], vector inclinometer [41], accelerometer [42], etc. In all of these sensing modalities researchers were interested in the response of the TFBG using unpolarized light. Polarization dependent properties of both TFBG and Long period gratings were utilized in designing bend sensors [40, 41, 43] and surface plasmon based sensors [44–46].

Erdogan and Sipe in [31] presented the first detailed theoretical treatment of the guided core mode to the radiation mode coupling properties. Y. Li presented two different methods of tackling the same problem in [47] and in [48]. In ref. [49] Dong et al presented a study regarding the effect of the grating tilt angle on the coupling properties of the guided core mode to the guided cladding modes. They used a number of assumptions including weakly guided approximation for both the core and the cladding modes. The weakly guiding approximation for the core mode in a single mode fibre is a widely accepted technique. However the cladding modes are guided strongly by the index difference of the cladding and the surrounding medium, and thus weakly guiding approximation does not hold for this waveguide. Hence, their work was only able to elucidate the coupling characteristics qualitatively. Lee and Erdogan in [50] presented a more comprehensive theoretical study of the coupling of the core mode to the guided cladding modes. The transmission spectrum of Bragg gratings with a weak tilt differs slightly depending on the relative orientation of the core mode polarization to the gratings tilt. This minor difference turned out to be a key factor in fulfilling the conditions

of plasmon excitation in a gold coated fibre with a TFBG [45]. However Lee and Erdogan's effort in [50] does not shed much light on the nature of the individual resonance structure. Lu et al. presented a numerical study in [51] in an effort to unify both the polarization dependent coupling characteristics of the core mode to the cladding modes and of the core mode to the radiation modes. For any sensing applications, including surface plasmon, it is the guided cladding modes which are of interest. [51] neither explicitly listed any polarization dependent coupling to modes nor elucidated the nature of the individual resonance structure. Hence their work does not provide any new insights into the coupling properties much beyond that of ref. [50]. Hence, in our view, the existing scientific papers fall short of presenting a complete polarization dependent description on the nature of the coupling to the guided cladding modes.

In this thesis we develop a comprehensive treatment of the polarization dependent TFBG coupling characteristic of the guided core modes to the cladding modes. We feel that the theoretical framework presented in the aforementioned references are exhaustive enough in treating polarization dependent coupling to the radiation modes and, hence, do not require any further investigation. However, the case of coupling to the cladding mode is entirely different. The cladding of a standard 1550 nm telecom fibre is a multimode waveguide and thus can support many thousands of modes. In this respect none of the previous studies explicitly lists the types and polarization nature of the cladding modes or the coupling nature of two orthogonally polarized core modes with respect to the grating tilt. Here we present such a comprehensive treatment of the polarization dependent response of the weakly tilted Bragg gratings by using exact field equations and utilizing numerical integration techniques. We show that a weak tilt differentiates between HE and EH modes and between TE and TM modes; thus TFBGs allow selective coupling to modes with radial or azimuthal polarization.

We also show that the hybrid cladding modes have preferential polarization orientation and by controlling the core mode polarization vector orientation with respect to the gratings plane, one could couple to modes of either polarization type. Moreover, there are spectral regions for any single mode fibre, where the resonances of these modes are spectrally well separated to be resolved.

Finally, we use this model to study the nanotube growth and to investigate the optical characteristics of nanotube films. Scientists have studied the property of an isolated single nanotube [8, 9, 52, 53], a highly aligned nanotube forest [54–58], or micrometer thick randomly oriented nanotubes [59]. However, to the best of our knowledge, there is no literature related to the nanotubes' optical response in the scale in between. Therefore, our work is the first effort studying the optical

response of the randomly oriented SWCNT from a few nanometres to a couple of hundreds nanometres thickness.

We begin our study by presenting the multilayer fibre model, dispersion relations, and field patterns in Chapter 2. We follow with presenting the polarization dependent coupling mechanisms in tilted Bragg gratings in Chapter 3. Armed with the knowledge of the these details we present the result of the layer-by-layer growth of the SWCNT in Chapter 4. We conclude our study with some after thoughts and comments on the future direction in Chapter 5.

VECTOR MODES AND EQUATIONS

*How do you solve a problem like $[\vec{\nabla} \times \frac{1}{\epsilon} \vec{\nabla} \times \vec{H} = (\frac{\omega}{c})^2 \vec{H}]$?
How do you hold a moonbeam in your hand?*

— Oscar Hammerstein II, *The Sound of Music*

The standard single mode telecom fibre is a three layer cylindrical structure which allows lossless propagation of a single mode in the core. The cladding modes excited by the TFBB are guided by the index difference between the cladding and the outer medium. Due to the minor index difference (~ 0.005) between the core and the cladding [49], the core mode dispersion relations and the field expressions can be very well represented by the weak guidance approximation [60]. In contrast, the cladding is a multimode waveguide and modes are in general strongly guided by the index difference between the cladding and the outer layer. Hence, for cladding modes, the weak guidance approximation which results in scalar modes does not hold. Moreover, in order to completely understand the polarization dependent interaction of modes with TFBB one needs to solve the exact vectorial solution. There are a number of simulation software capable of numerically computing the modal behaviour of any arbitrary structure using Finite Difference or Finite Element methods. However, the modal data obtained from these software is not readily suitable to study the modal interactions with the TFBB, and substantially more calculations are needed. Hence we develop a complete analytical approach in trying to understand the mode distributions and the field patterns. This chapter is devoted to presenting the mode solutions and the field patterns of the fibre mode guided by the cladding.

In general, a radially stratified dielectric waveguide has two types of mode: Transverse and Hybrid. The transverse modes have either the axial electric field or the axial magnetic field equal to zero, whereas for the hybrid modes both the axial electric and magnetic field components are present [60]. A number of authors over the years tried to develop the exact solutions of the guided modes in a three-layer dielectric waveguide. Belanov et al. made the first such attempt in references [61, 62] using the weak guidance approximation. Yeh and Lindgren [63] proposed an efficient matrix method to find the dispersion relation for any radially stratified dielectric waveguide. Tso et al. developed an exact vectorial solution of a three layer structure using the Debye potentials [60, 64]. Erdogan in [65] presented the field equations and the dispersion relation for hybrid modes with azimuthal order of one. The modifications of the equations as presented

by Erdogan for a generalized hybrid mode are not trivial. We use Erdogan's notations and Tsao's formalism to derive all equations. Our solutions are general and can be applied for any index distribution and for any guided mode of any order or type.

We begin this chapter with the presentation of the core mode field expressions followed by those of the cladding modes. The fundamental procedure to derive the expressions are the same for both the core and the cladding modes. Hence, we only show the detailed derivation for the cladding modes. We then present the algorithm of solving the dispersion relation in section 2.3. We present the polarization nature and field distribution of the cladding modes in the section 2.4. We conclude this chapter with the presentation of the equations for a four-layer structure in the section 2.5 that is used to analyse the behaviour of a coated fibre.

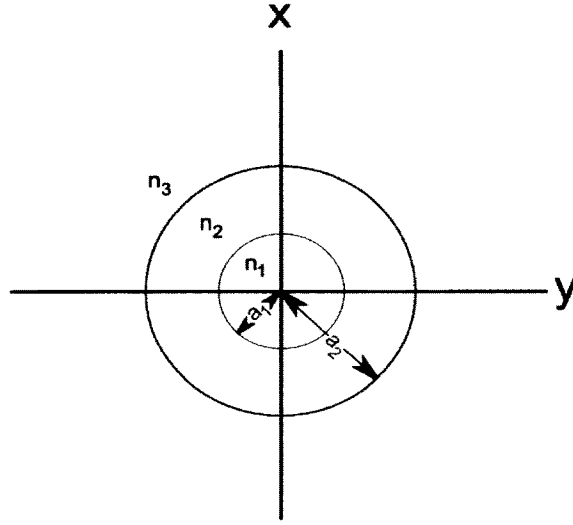


Figure 1: The generalized three layer fibre structure

2.1 THE CORE MODE IN A THREE-LAYERED STRUCTURE

We are interested in the interaction between the fundamental core mode and the cladding modes in a standard telecom fibre, e.g. Corning SMF-28. Such a fibre has a low index difference (~ 0.005) between the core and the cladding. Hence, the core mode expressions can be simplified using a weakly guiding approximation [66]. Figure 1 represents the generalized structure of a three layer cylindrical waveguide. For such a structure, with a_1 , a_2 and n_1 , n_2 as core and cladding

radii and refractive indexes respectively, the fundamental HE_{11} mode eigenvalue equation is [64]

$$\frac{J_0[a_1 u_{\text{core}}]}{a_1 u_{\text{core}} J_1[a_1 u_{\text{core}}]} - \frac{K_0[a_1 w_{\text{core}}]}{a_1 w_{\text{core}} 2K_0[a_1 w_{\text{core}}]} = 0 \quad (2.1.1)$$

where, J is the Bessel function of the first kind and K is the modified Bessel function of the second kind, $u_{\text{core}} = (2\pi/\lambda)(n_1^2 - n_{\text{effcore}}^2)^{\frac{1}{2}}$, and $w_{\text{core}} = (2\pi/\lambda)(n_{\text{effcore}}^2 - n_2^2)^{\frac{1}{2}}$ are the phase parameters of the fundamental core mode with the effective guide index of n_{effcore} at a wavelength of λ . This equation in general contains many roots (n_{effcore}), and can be solved once the value of all parameters are known. However, in a single mode fibre the core is deliberately designed to be small enough to allow the lossless propagation of only the fundamental mode (HE_{11}) in the designed wavelength of operation. The fields for the weakly guiding approximation, in the cylindrical coordinates ($\hat{r}, \hat{\phi}, \hat{z}$) for the HE_{11} mode can be expressed as

Core region: $r \leq a_1$

$$E_r^{\text{core}} = E_{\text{co}}^{11} u_{\text{core}} J_0[u_{\text{core}} r] \cos[\phi + \psi] \quad (2.1.2a)$$

$$E_{\phi}^{\text{core}} = -E_{\text{co}}^{11} u_{\text{core}} J_0[u_{\text{core}} r] \sin[\phi + \psi] \quad (2.1.2b)$$

$$H_r^{\text{core}} = E_{\text{co}}^{11} \frac{n_1}{Z_0} u_{\text{core}} J_0[u_{\text{core}} r] \sin[\phi + \psi] \quad (2.1.2c)$$

$$H_{\phi}^{\text{core}} = E_{\text{co}}^{11} \frac{n_1}{Z_0} u_{\text{core}} J_0[u_{\text{core}} r] \cos[\phi + \psi] \quad (2.1.2d)$$

Cladding region: $a_1 \leq r \leq a_2$

$$E_r^{\text{core}} = E_{\text{co}}^{11} B w_{\text{core}} (-K_0[w_{\text{core}} r]) \cos[\phi + \psi] \quad (2.1.3a)$$

$$E_{\phi}^{\text{core}} = -E_{\text{co}}^{11} B w_{\text{core}} (-K_0[w_{\text{core}} r]) \sin[\phi + \psi] \quad (2.1.3b)$$

$$H_r^{\text{core}} = E_{\text{co}}^{11} \frac{n_1}{Z_0} B w_{\text{core}} (-K_0[w_{\text{core}} r]) \sin[\phi + \psi] \quad (2.1.3c)$$

$$H_{\phi}^{\text{core}} = E_{\text{co}}^{11} \frac{n_1}{Z_0} B w_{\text{core}} (-K_0[w_{\text{core}} r]) \cos[\phi + \psi] \quad (2.1.3d)$$

where $B = -u_{\text{core}}^2 J_1[a_1 u_{\text{core}}] / w_{\text{core}}^2 K_1[a_1 w_{\text{core}}]$, $Z_0 = 377 \Omega$ is the impedance of the free space and the azimuthal angle ϕ is measured with respect to the vertical X-axis. The Field amplitude coefficient is set to

$$E_{\text{co}}^{11} = \left[\frac{2Z_0 b}{u_0^2 a_1^2 J_1^2[u_0 a_1]} \right]^{\frac{1}{2}} \quad (2.1.4)$$

where

$$b = \frac{n_{\text{effcore}}^2 - n_2^2}{n_1^2 - n_2^2} \quad (2.1.5)$$

in order to set the total power carried by the mode to 1 Watt [67] using

$$P = 0.5 \operatorname{Re} \left\{ \int_0^{2\pi} \int_0^{\infty} (E_r H_{\phi}^* - E_{\phi} H_r^*) r dr d\phi \right\} = 1 \text{ W} \quad (2.1.6)$$

The integral in the radial direction is the summation of two integrals involving the field expressions in the core using relations in equation set 2.1.2 and in the cladding using those of equation set 2.1.3 respectively. Since the field of a core guided mode exponentially decays in the cladding and the cladding diameter normally is much larger than the penetration depth of any such field, the upper limit of the radial integration reduces from ∞ to a_2 . The axial field components of a well guided HE_{11} mode are negligible in comparison to the transverse components. Accordingly, the HE_{11} field has linearly polarized X- or Y- polarization state. For $\psi = 0$ ($\psi = \pi/2$) the expressions in equations 2.1.2 and 2.1.3 expresses X-polarized (Y- polarized) field corresponding to even and odd mode respectively. In general due to the cylindrical symmetry any arbitrary value of ψ corresponds to a valid solution. We identify the two orthogonal polarizations by taking $\psi = 0$ or $\psi = \pi/2$.

2.2 CLADDING MODE IN A THREE-LAYER STRUCTURE

Cladding modes are not weakly guiding and hence a full vectorial description of these modes are required. Due to the cylindrical symmetry of the structure we adopt the polar coordinate system $(\hat{r}, \hat{\phi}, \hat{z})$ with its \hat{z} -axis aligned to the waveguide axis. In general, the electric and the magnetic fields in polar coordinates for each layer can be represented by [60]

$$\begin{aligned} \vec{E} = & \hat{r}[\partial\Psi/r\partial\phi - (\beta/\omega\epsilon_i)\partial\Phi/\partial r] - \hat{\phi}[\partial\Psi/\partial r \\ & + (\beta/\omega\epsilon_i)\partial\Phi/r\partial\phi] - \hat{z}[(k^2n_i^2 - \beta^2)/i\omega\epsilon_i]\Phi \end{aligned} \quad (2.2.1a)$$

$$\begin{aligned} \vec{H} = & \hat{r}[\partial\Phi/r\partial\phi + (\beta/\omega\mu)\partial\Psi/\partial r] - \hat{\phi}[\partial\Phi/\partial r \\ & - (\beta/\omega\mu)\partial\Psi/r\partial\phi] + \hat{z}[(k^2n_i^2 - \beta^2)/i\omega\mu]\Psi \end{aligned} \quad (2.2.1b)$$

where Ψ and Φ denote the scalar Debye potentials and $i = \sqrt{-1}$. The \vec{E} and \vec{H} satisfy the following wave equation [60]

$$\{\nabla^2 + k^2n_i^2 - \beta^2\} \begin{Bmatrix} \vec{E} \\ \vec{H} \end{Bmatrix} = 0 \quad \{i = 1, 2, 3\} \quad (2.2.2)$$

The solution to the wave equation above for a cylindrical structure is [60]

$$\Phi_1 = A_1 J_l[u_1 r] \text{Exp}[il\phi] \quad (2.2.3a)$$

$$\Phi_2 = \{A_2 J_l[u_2 r] + B_2 Y_l[u_2 r]\} \text{Exp}[il\phi] \quad (2.2.3b)$$

$$\Phi_3 = B_3 K_l[w_3 r] \text{Exp}[il\phi] \quad (2.2.3c)$$

$$\Psi_1 = C_1 J_l[u_1 r] \text{Exp}[il\phi] \quad (2.2.3d)$$

$$\Psi_2 = \{C_2 J_l[u_2 r] + D_2 Y_l[u_2 r]\} \text{Exp}[il\phi] \quad (2.2.3e)$$

$$\Psi_3 = D_3 K_l[w_3 r] \text{Exp}[il\phi] \quad (2.2.3f)$$

Where the subscript (1, 2, 3) denotes the layer number and A, B, C, D are amplitude coefficients. In the above equations $J_l[u_i r]$ is associated with the convergent wave and is singular at the infinity $r = \infty$; $Y_l[u_i r]$ and $K_l[w_i r]$ are associated with the divergent wave and are singular at the centre $r = 0$. l is the azimuthal index and is a non negative integer due to the symmetry consideration. The cladding supports rotationally symmetric TE and TM modes [68]. However, no ϕ dependent transverse mode can exist due to the non vanishing E_z and H_z components. These modes are known as hybrid modes. Hence the cladding modes consist of TE_{0m} , TM_{0m} , HE_{lm} , and EH_{lm} modes. In our formalism "l" refers to the azimuthal order and "m" refers to the radial order of a mode. The exact expression for each vector components is found using the appropriate boundary conditions.

2.2.1 Hybrid Mode Field Expressions and Dispersion Relation

Hybrid modes have both E_z and H_z components. The substitution of expressions for both scalar Debye potentials Φ and Ψ from the eqn 2.2.3 into the eqn 2.2.1 gives

Core region: $r \leq a_1$

$$E_r = \frac{l}{ln_1^2 r} (C_1 l^2 n_1^2 J_l[u_1 r] + A_1 r u_1 \sigma_2 J'_l[u_1 r]) \text{Exp}[il\phi] \quad (2.2.4a)$$

$$E_\phi = -\frac{1}{n_1^2 r} (A_1 \sigma_2 J_l[u_1 r] + C_1 n_1^2 r u_1 J'_l[u_1 r]) \text{Exp}[il\phi] \quad (2.2.4b)$$

$$E_z = \frac{A_1}{ln_1^2 \beta} u_1^2 \sigma_2 J_l[u_1 r] \text{Exp}[il\phi] \quad (2.2.4c)$$

$$H_r = \frac{l}{lr} (A_1 l^2 J_l[u_1 r] - C_1 r u_1 \sigma_1 J'_l[u_1 r]) \text{Exp}[il\phi] \quad (2.2.4d)$$

$$H_\phi = \frac{1}{r} (C_1 \sigma_1 J_l[u_1 r] - A_1 r u_1 J'_l[u_1 r]) \text{Exp}[il\phi] \quad (2.2.4e)$$

$$H_z = -\frac{1}{l\beta} u_1^2 \sigma_1 J_l[u_1 r] \text{Exp}[il\phi] \quad (2.2.4f)$$

Cladding region: $a_1 \leq r \leq a_2$

$$E_r = \frac{1}{\ln_2^2 r} (C_2 l^2 n_2^2 J_1[u_2 r] + D_2 l^2 n_2^2 Y_1[u_2 r] + r u_2 \sigma_2 (A_2 J_1'[u_2 r] + B_2 Y_1'[u_2 r])) \text{Exp}[i l \phi] \quad (2.2.5a)$$

$$E_\phi = -\frac{1}{n_2^2 r} (A_2 \sigma_2 J_1'[u_2 r] + B_2 \sigma_2 Y_1'[u_2 r] + n_2^2 r u_2 (C_2 J_1'[u_2 r] + D_2 Y_1'[u_2 r])) \text{Exp}[i l \phi] \quad (2.2.5b)$$

$$E_z = \frac{u_2^2 \sigma_2}{\ln_2^2 \beta} (A_2 J_1[u_2 r] + B_2 Y_1[u_2 r]) \text{Exp}[i l \phi] \quad (2.2.5c)$$

$$H_r = \frac{1}{l r} (A_2 l^2 J_1[u_2 r] + B_2 l^2 Y_1[u_2 r] - r u_2 \sigma_1 (C_2 J_1'[u_2 r] + D_2 Y_1'[u_2 r])) \text{Exp}[i l \phi] \quad (2.2.5d)$$

$$H_\phi = \frac{1}{r} (C_2 \sigma_1 J_1[u_2 r] + D_2 \sigma_1 Y_1[u_2 r] - r u_2 (A_2 J_1'[u_2 r] + B_2 Y_1'[u_2 r])) \text{Exp}[i l \phi] \quad (2.2.5e)$$

$$H_z = -\frac{u_2^2 \sigma_1}{l \beta} (C_2 J_1[u_2 r] + D_2 Y_1[u_2 r]) \text{Exp}[i l \phi] \quad (2.2.5f)$$

Outer region: $r \geq a_2$

$$E_r = \frac{1}{\ln_3^2 r} (D_3 l^2 n_3^2 K_1[w_3 r] + B_3 r w_3 \sigma_2 K_1'[w_3 r]) \text{Exp}[i l \phi] \quad (2.2.6a)$$

$$E_\phi = -\frac{1}{n_3^2 r} (B_3 \sigma_2 K_1[w_3 r] + D_3 n_3^2 r w_3 K_1'[w_3 r]) \text{Exp}[i l \phi] \quad (2.2.6b)$$

$$E_z = -\frac{B_3 w_3^2 \sigma_2}{\ln_3^2 \beta} K_1[w_3 r] \text{Exp}[i l \phi] \quad (2.2.6c)$$

$$H_r = \frac{1}{l r} (B_3 l^2 K_1[w_3 r] - D_3 r w_3 \sigma_1 K_1'[w_3 r]) \text{Exp}[i l \phi] \quad (2.2.6d)$$

$$H_\phi = \frac{1}{r} (D_3 \sigma_1 K_1[w_3 r] - B_3 r w_3 K_1'[w_3 r]) \text{Exp}[i l \phi] \quad (2.2.6e)$$

$$H_z = \frac{D_3 w_3^2 \sigma_1}{l \beta} K_1[w_3 r] \text{Exp}[i l \phi] \quad (2.2.6f)$$

where the following relationships hold

$$\sigma_1 = i\ln_{eff}/Z_0 \quad (2.2.7)$$

$$\sigma_2 = i\ln_{eff}Z_0 \quad (2.2.8)$$

$$u_{21} = \frac{1}{u_2^2} - \frac{1}{u_1^2} \quad (2.2.9)$$

$$u_{32} = \frac{1}{u_2^2} + \frac{1}{w_3^2} \quad (2.2.10)$$

$$u_j = \frac{2\pi}{\lambda} \sqrt{n_j^2 - n_{eff}^2}, \quad [j \in (1, 2)] \quad (2.2.11)$$

$$w_3 = \frac{2\pi}{\lambda} \sqrt{n_{eff}^2 - n_3^2} \quad (2.2.12)$$

$$\beta = \frac{2\pi n_{eff}}{\lambda} \quad (2.2.13)$$

The field amplitude coefficients $A_1, A_2, B_2, B_3, C_1, C_2, D_2$ and D_3 weigh the contribution of each term. The exact field expressions can only be determined after relationships between these coefficients are derived. The field expressions in equation 2.2.1 are correct for each individual layer. A consistent solution for the whole structure requires these relations to satisfy the electromagnetic boundary conditions, i.e. H_ϕ, E_ϕ, H_z , and E_z must be continuous at each interface. The boundary continuity conditions at each radii $r = a_1$ and $r = a_2$ result in a total of eight equations corresponding to eight tangential components. For a non trivial solution to exist for the wave equation 2.2.2, the determinant of the coefficient matrix of the amplitude coefficients must be equal to zero [60]. This gives the following expression

$$\zeta_0 = \zeta' \quad (2.2.14a)$$

$$\zeta_0 = \frac{u_2 p_1[a_2] \left(\frac{\sigma_1 \sigma_2 u_{21} u_{32}}{a_1 a_2 n_1^2} + JK \right) + J r_1[a_2] - K q_1[a_2] - \frac{s_1[a_2]}{u_2}}{\sigma_2 \left(u_2 p_1[a_2] \left(\frac{K u_{21}}{a_1 n_1^2} - \frac{J u_{32}}{a_2 n_2^2} \right) + \frac{u_{21} r_1[a_2]}{a_1 n_1^2} + \frac{u_{32} q_1[a_2]}{a_2 n_1^2} \right)} \quad (2.2.14b)$$

$$\zeta' = \frac{\sigma_1 \{ u_2 p_1[a_2] \left(\frac{J u_{32}}{a_2} - \frac{K n_3^2 u_{21}}{a_1 n_2^2} \right) - \frac{u_{21} r_1[a_2]}{a_1} - \frac{u_{32} q_1[a_2]}{a_2} \}}{p_1[a_2] u_2 \left(\frac{\sigma_1 \sigma_2 u_{21} u_{32}}{a_1 a_2 n_1^2} + \frac{JK n_3^2}{n_2^2} \right) + J r_1[a_2] - \frac{K n_3^2 q_1[a_2]}{n_1^2} - \frac{n_2^2 s_1[a_2]}{n_1^2 u_2}} \quad (2.2.14c)$$

where the following relationships hold

$$J = \frac{J'_l[a_1 u_1]}{u_1 J_l[a_1 u_1]}, \quad (2.2.15a)$$

$$K = \frac{K'_l[a_2 w_3]}{w_3 K_l[a_2 w_3]}, \quad (2.2.15b)$$

The derivatives of the Bessel functions are with respect to the arguments. The four Bessel function cross products used here are expressed as

$$p_l[r] = J_l[ru_2]Y_l[a_1u_2] - J_l[a_1u_2]Y_l[ru_2] \quad (2.2.15c)$$

$$q_l[r] = J_l[ru_2]Y'_l[a_1u_2] - J'_l[a_1u_2]Y_l[ru_2] \quad (2.2.15d)$$

$$r_l[r] = J'_l[ru_2]Y_l[a_1u_2] - J_l[a_1u_2]Y'_l[ru_2] \quad (2.2.15e)$$

$$s_l[r] = J'_l[ru_2]Y'_l[a_1u_2] - J'_l[a_1u_2]Y'_l[ru_2] \quad (2.2.15f)$$

We then derive relationships between amplitude coefficients of field equations by solving the system of linear equation involving the electromagnetic boundary conditions. Fields as expressed by equations (2.2.4), (2.2.5), and (2.2.6) are complex. Only the real or the imaginary parts of these complex quantities represent the real field. By using Euler's identity and defining all relations in terms of $E_{cl}^{lm} = C_l$ the field expressions become

Core region: $r \leq a_1$

$$E_r^{cl} = E_{cl}^{lm} \left\{ \frac{\zeta_0 \sigma_2 u_1 J'_l[ru_1]}{ln_1^2} + \frac{l J_l[ru_1]}{r} \right\} \cos[l\phi + \psi] \quad (2.2.16a)$$

$$E_\phi^{cl} = E_{cl}^{lm} \left\{ -\frac{\zeta_0 \sigma_2 J_l[ru_1]}{n_1^2 r} - u_1 J'_l[ru_1] \right\} \sin[l\phi + \psi] \quad (2.2.16b)$$

$$H_r^{cl} = E_{cl}^{lm} \left\{ \frac{i\zeta_0 l J_l[ru_1]}{r} - \frac{i\sigma_1 u_1 J'_l[ru_1]}{l} \right\} \sin[l\phi + \psi] \quad (2.2.16c)$$

$$H_\phi^{cl} = E_{cl}^{lm} \left\{ i\zeta_0 u_1 J'_l[ru_1] - \frac{i\sigma_1 J_l[ru_1]}{r} \right\} \cos[l\phi + \psi] \quad (2.2.16d)$$

Cladding region: $a_1 \leq r \leq a_2$

$$E_r^{cl} = E_{cl}^{lm} \pi a_1 u_1^2 J_l[a_1 u_1] \left\{ -\frac{l(F_2 u_2 p_l[r] - q_l[r])}{2ru_2} - \frac{\sigma_2(G_2 n_1^2 u_2 r_l[r] - \zeta_0 n_2^2 s_l[r])}{2ln_1^2 n_2^2} \right\} \cos[l\phi + \psi] \quad (2.2.17a)$$

$$E_\phi^{cl} = E_{cl}^{lm} \pi a_1 u_1^2 J_l[a_1 u_1] \left\{ \frac{1}{2}(F_2 u_2 r_l[r] - s_l[r]) + \sigma_2 \left(\frac{G_2 p_l[r]}{2n_2^2 r} - \frac{\zeta_0 q_l[r]}{2n_1^2 ru_2} \right) \right\} \sin[l\phi + \psi] \quad (2.2.17b)$$

$$H_r^{cl} = E_{cl}^{lm} \pi a_1 u_1^2 J_l[a_1 u_1] \left\{ \frac{i\sigma_1(F_2 u_2 r_l[r] - s_l[r])}{2l} + l \left(\frac{i\zeta_0 n_2^2 q_l[r]}{2n_1^2 ru_2} - \frac{iG_2 p_l[r]}{2r} \right) \right\} \sin[l\phi + \psi] \quad (2.2.17c)$$

$$H_\phi^{cl} = E_{cl}^{lm} \pi a_1 u_1^2 J_l[a_1 u_1] \left\{ \frac{i\sigma_1(F_2 u_2 p_l[r] - q_l[r])}{2ru_2} - \frac{1}{2}iG_2 u_2 r_l[r] + \frac{i\zeta_0 n_2^2 s_l[r]}{2n_1^2} \right\} \cos[l\phi + \psi] \quad (2.2.17d)$$

Outer region: $a_2 \leq r$

$$E_r^{cl} = E_{cl}^{lm} \frac{\pi a_1 u_1^2 u_2^2 J_l[a_1 u_1]}{K_l[a_2 w_3]} \left\{ -\frac{F_3 l K_l[rw_3]}{2rw_3^2} - \frac{G_3 \sigma_2 K_l'[rw_3]}{2ln_3^2 w_3} \right\} \cos[l\phi + \psi] \quad (2.2.18a)$$

$$E_\phi^{cl} = E_{cl}^{lm} \frac{\pi a_1 u_1^2 u_2^2 J_l[a_1 u_1]}{K_l[a_2 w_3]} \left\{ \frac{F_3 K_l'[rw_3]}{2w_3} + \frac{G_3 \sigma_2 K_l[rw_3]}{2n_3^2 rw_3^2} \right\} \sin[l\phi + \psi] \quad (2.2.18b)$$

$$H_r^{cl} = E_{cl}^{lm} \frac{\pi a_1 u_1^2 u_2^2 J_l[a_1 u_1]}{K_l[a_2 w_3]} \left\{ \frac{iF_3 \sigma_1 K_l'[rw_3]}{2lw_3} - \frac{iG_3 l K_l[rw_3]}{2rw_3^2} \right\} \sin[l\phi + \psi] \quad (2.2.18c)$$

$$H_\phi^{cl} = E_{cl}^{lm} \frac{\pi a_1 u_1^2 u_2^2 J_l[a_1 u_1]}{K_l[a_2 w_3]} \left\{ \frac{iF_3 \sigma_1 K_l[rw_3]}{2rw_3^2} - \frac{iG_3 K_l'[rw_3]}{2w_3} \right\} \cos[l\phi + \psi] \quad (2.2.18d)$$

where

$$F_2 = J - \frac{u_{21} \zeta_0 \sigma_2}{a_1 n_1^2} \quad (2.2.19a)$$

$$G_2 = J \zeta_0 + \frac{u_{21} \sigma_1}{a_1} \quad (2.2.19b)$$

$$F_3 = -F_2 p_l[a_2] + \frac{q_l[a_2]}{u_2} \quad (2.2.19c)$$

$$G_3 = n_3^2 \left[-\frac{G_2 p_l[a_2]}{n_2^2} + \frac{\zeta_0 q_l[a_2]}{n_1^2 u_2} \right] \quad (2.2.19d)$$

In these equations E_{cl}^{lm} is the cladding mode amplitude coefficient. The value of this coefficient is chosen in a manner as to allow the total power carried by the mode to be 1W using equation (2.1.6). Once the mode index is calculated from the dispersion relation of equation (2.2.14), E_{cl}^{lm} can be easily calculated using a standard numerical integration technique. For the cladding modes, the radial part of the integration is the summation of three integrals for core, cladding, and outer regions. All integrals involving field equations are highly oscillatory in nature and need a careful selection of right numerical techniques for fast computation. We computed all numerical integrations using Gauss-Kronrod quadrature rule and a global adaptive algorithm [69].

For $\psi = 0$ equations (2.2.16), (2.2.17), and (2.2.18) express the odd modes. For $\psi = \pi/2$ these equations represent the even modes. Hence, a hybrid mode is degenerate between even and the odd mode. The field pattern of the even and the odd modes are rotated with respect to each other by $\pi/2l$, where l is the azimuthal order of the mode.

2.2.2 TE and TM Mode Field Expressions

TE mode has no \hat{z} component of the electric field, whereas TM mode has no H_z component. These are represented by choosing the Debye potential $\Phi = 0$ for the TE case and $\Psi = 0$ for the TM case in equation (2.2.3). By using these two values in equations (2.2.4), (2.2.5), and (2.2.6) and utilising the boundary continuity conditions we can solve the equations for the TE and for the TM cases respectively. After developing the relations between the amplitude coefficients we set $l = 0$ to obtain the final expressions for both TE_{0m} and TM_{0m} cases.

For TE_{0m} modes the radial and the axial components of the electric field and azimuthal component of the magnetic field are zero. For TE modes, the field expressions for the rest of the components are as follows

Core region: $r \leq a_1$

$$E_\phi = -E_{cl}^{TE,m} u_1 J'_0[u_1 r] \quad (2.2.20a)$$

$$H_r = E_{cl}^{TE,m} u_1 \frac{n_{eff}}{Z_0} J'_0[u_1 r] \quad (2.2.20b)$$

Cladding region: $a_1 \leq r \leq a_2$

$$E_\phi = E_{cl}^{TE,m} \frac{1}{2} \pi u_1^2 J_0[u_1 a_1] u_2 a_1 (J_1[r] - \frac{s_1[r]}{u_2}) \quad (2.2.20c)$$

$$H_r = E_{cl}^{TE,m} \frac{n_{eff}}{2Z_0} \pi u_1^2 J_0[u_1 a_1] u_2 a_1 (-J_1[r] + \frac{s_1[r]}{u_2}) \quad (2.2.20d)$$

Outer region: $a_2 \leq r$

$$E_\phi = -E_{cl}^{TE,m} \frac{\pi u_1^2 u_2^2 J_0[u_1 a_1] a_1}{2w_3 K_0[w_3 a_3]} \left(\frac{q_1[a_2]}{u_2} - J_1[a_2] \right) K'_0[w_3 r] \quad (2.2.20e)$$

$$H_r = E_{cl}^{TE,m} \frac{\pi n_{eff} u_1^2 u_2^2 J_0[u_1 a_1] a_1}{2Z_0 w_3 K_0[w_3 a_3]} \left(\frac{q_1[a_2]}{u_2} - J_1[a_2] \right) K'_0[w_3 r] \quad (2.2.20f)$$

$E_{cl}^{TE,m}$ is the normalization factor for TE_{0m} modes and can be numerically calculated using equation 2.1.6.

For TM_{0m} modes, the radial and the axial components of the magnetic field and the azimuthal component of the electric field are zero. The field expressions for the rest of the components are as follows

Core region: $r \leq a_1$

$$E_r = -E_{cl}^{TM,m} \frac{x u_1 Z_0 J'_0[ru_1]}{n_1^2} \quad (2.2.21a)$$

$$H_\phi = -E_{cl}^{TM,m} u_1 J'_0[u_1 r] \quad (2.2.21b)$$

Cladding region: $a_1 \leq r \leq a_2$

$$E_r = E_{cl}^{TM,m} \frac{a_1 n_{eff} \pi u_1^2 Z_0 J_0[a_1 u_1] (J_1^2 u_2 r_l[r] - n_2^2 s_l[r])}{2 n_1^2 n_2^2} \quad (2.2.21c)$$

$$H_\phi = E_{cl}^{TM,m} \frac{a_1 \pi u_1^2 J_0[a_1 u_1] (J_1^2 u_2 r_l[r] - n_2^2 s_l[r])}{2 n_1^2} \quad (2.2.21d)$$

Outer region: $a_2 \leq r$

$$E_r = E_{cl}^{TM,m} \frac{a_1 n_{eff} \pi u_1^2 Z_0 J_0[a_1 u_1] (J_1^2 u_2 r_l[a_2] - n_2^2 s_l[a_2]) K_0'[rw_3]}{2 K n_1^2 n_3^2 w_3 K_0'[a_2 w_3]} \quad (2.2.21e)$$

$$H_\phi = E_{cl}^{TM,m} \frac{a_1 \pi u_1^2 J_0[a_1 u_1] (J_1^2 u_2 r_l[a_2] - n_2^2 s_l[a_2]) K_0'[rw_3]}{2 K n_1^2 w_3 K_0[a_2 w_3]} \quad (2.2.21f)$$

Here, $E_{cl}^{TM,m}$ is the normalization factor for TM_{0m} mode.

2.3 SOLVING THE DISPERSION RELATION

In general, a well guided mode is lossless if there is no material absorption. For a lossless case the guide index, n_{eff} , for any mode is a real number. However, a well guided mode can become lossy due to the presence of the material absorption or near and beyond cutoff even without the presence of any lossy material. Under these circumstances the guide index, n_{eff} becomes a complex quantity, where the complex part is proportional to the loss coefficient of the mode. We adopt a mode searching mechanism which is capable of handling both scenarios.

2.3.1 For Lossless Case

The dispersion relations in equation (2.2.14) is transcendental and contains many solutions. Typically, the challenge is to know which solution corresponds to which kind of mode for the given waveguide. Snitzer in [68] was first to propose a mode classification scheme for an all dielectric optical waveguide. His scheme was based on the sign of the coefficient ratio which expresses the relative strength of E_z and H_z components in a mode. Safaai-Jazi and Yip [70] revealed that Snitzer's scheme is only consistent for the core modes; for cladding modes the sign changes arbitrarily and hence can not be used for the classification of the hybrid modes in the cladding region. A number of other authors including Safaai-Jazi and Yip took on this issue and proposed various techniques for the classification of modes in cylindrical waveguides with different index distributions [71, 72]. Kapoor and Singh presented a detailed comparative study of various mode

classification schemes in [73] and proposed a universal technique of mode designation which is consistent with the specific solutions proposed by Safaai-Jazi and Yip, Morishita, and Yeh for different cylindrical waveguide structures. We follow this technique to seek the appropriate modal solutions. According to ref. [73], the dispersion relation in equation (2.2.14) is a quadratic equations of both J (equation (2.2.15a)) and K (equation (2.2.15b)). The root of the quadratic equation in terms of K containing the positive sign(negative sign) describes the HE modes (EH modes). For $l = 0$ the root containing the positive sign(negative sign)describes the TE modes (TM modes).

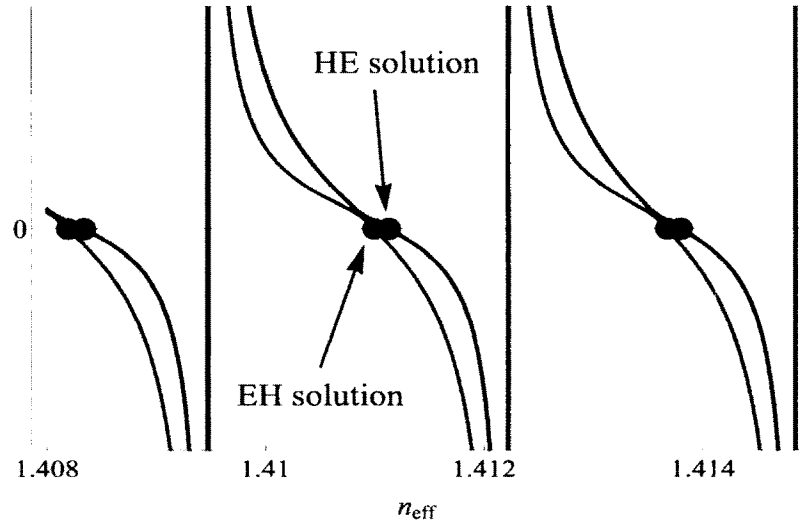


Figure 2: A graphical method for solving the eigenvalue equation (2.2.14)

The basic idea of the mode solution technique is to look for a guided index, n_{eff} which is smaller than the highest index in the structure, generally the core index (n_1), and bigger than the lowest index of the structure, generally the index of the out most medium (n_3). There are many ways the transcendental dispersion equation (2.2.14) can be solved. We adopted numerical techniques using Newton's method. In Newton's method a "guess" root is used as a seed to find the root of interest. The speed of convergence in Newton's method depends on the quality of the guess root. We use the "MeshFunctions" of the "Plot" command of Mathematica to extract zero crossing of the dispersion equation, and use these zero crossing points as the seed solutions. Since the values returned by the "MeshFunctions" are very close to the actual solution, this technique guarantees fast convergence to the highly accurate (20 digit precision) solution. Figure 2 shows schematically the solution of the dispersion relations for the hybrid modes with $l = 1$.

Figure 3 shows a typical solution for the HE modes of the first six azimuthal orders. The solution was obtained using $a_1 = 4.1\mu m$, $a_2 =$

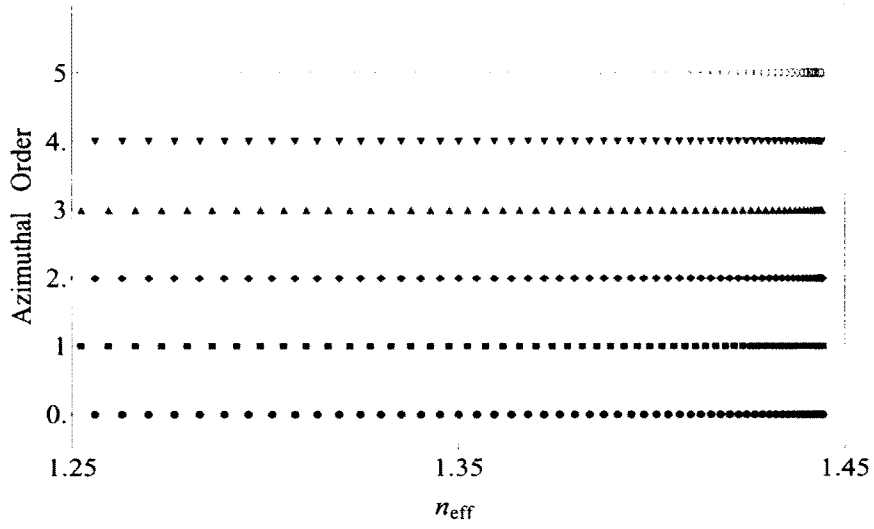


Figure 3: Typical solutions of the eigenvalue equation (2.2.14)

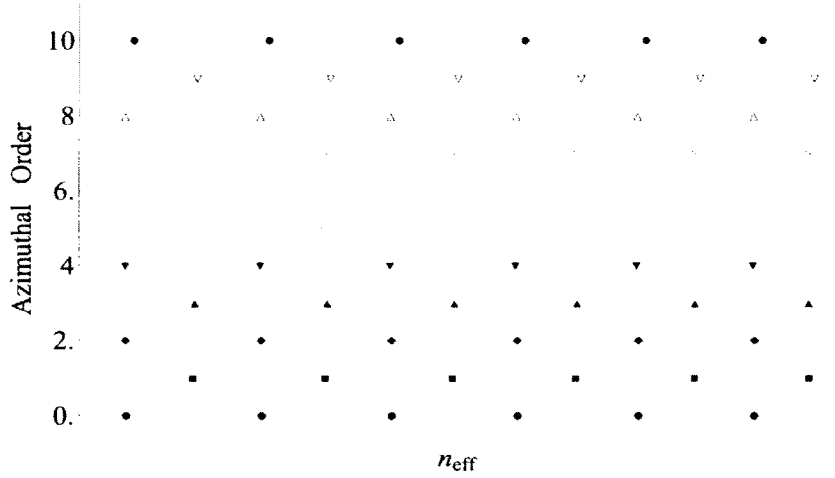


Figure 4: The even and the odd azimuthal order solutions are nearly degenerate

62.5 μm , $n_1 = 1.450699$, $n_2 = 1.444024$, $n_3 = 1.0$ at $\lambda = 1566\text{nm}$. It is evident from the plot that the lower order radial modes, i.e. modes with higher effective indexes, have less spacing than the higher order radial modes. Figure 4 shows a part of the same solution. This plot shows that the modes of even azimuthal order (including 0 order modes) are nearly degenerate, so is true for modes of odd azimuthal orders.

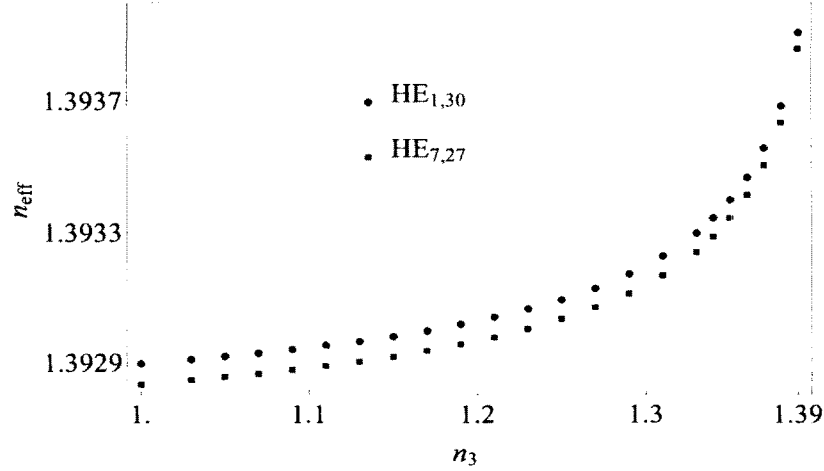


Figure 5: The variation in the effective index as a function of n_3

We also check the consistency of the solution by varying the index of the out-most medium, n_3 , from that of air to index close to the cutoff of two arbitrary HE modes ($l = 1$ and 7) with nearly equal effective index in the air. The result is plotted in Figure 5. The effective guide indices of both modes change with n_3 . The sensitivity of the modes, i.e. the rate of change of the guide index as a function of n_3 , is not constant for the entire range and in this case modes become maximally sensitive close to the cutoff, i.e. when n_3 approaches the guide index of these modes. Moreover, the sensitivities of these modes are nearly equal despite being of two different azimuthal order.

2.3.2 For Lossy Cases

The approach to find the complex index is similar to that of the lossless case. The mode index for a lossy case, due to the material absorption or beyond cutoff, is complex. The material absorption for the core and the cladding in the telecom band are negligible and are ignored. Hence only an absorptive outer medium can introduce loss factor to a well guided cladding mode. Since the evanescent part of a mode overlaps in the outer lossy medium, the effective imaginary part of the mode guide index should remain at least a couple of orders of magnitude smaller than the imaginary part of n_3 . Similarly, the per-

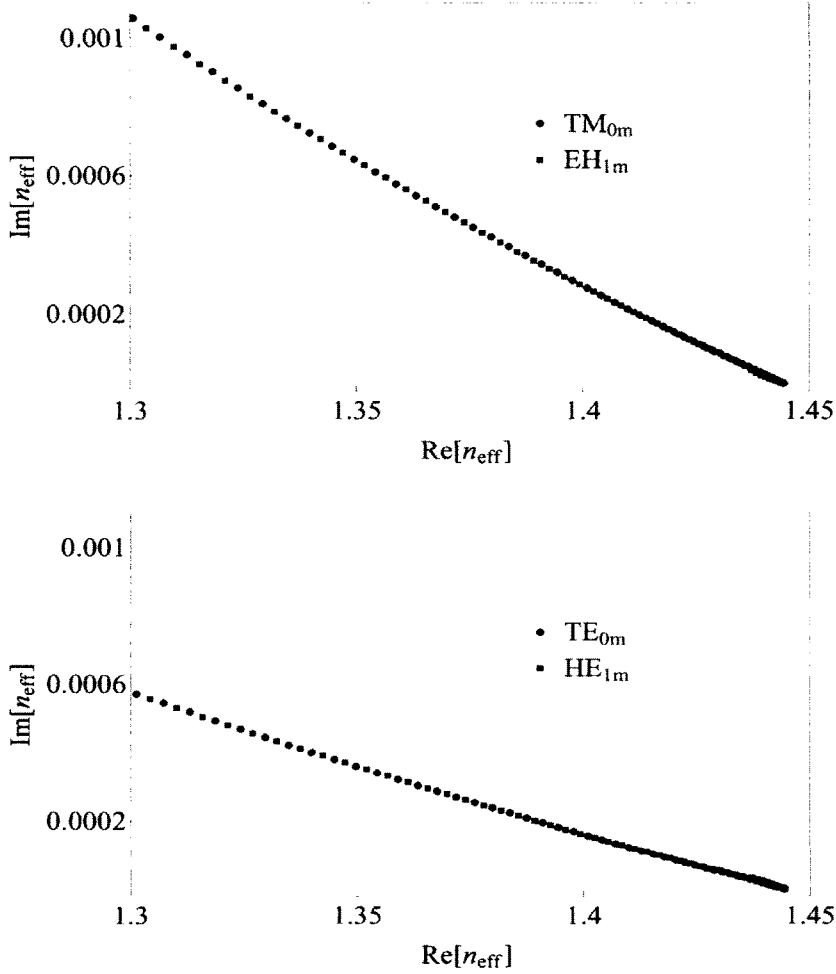


Figure 6: The imaginary part of the guide index for azimuthal order $l = 0, 1$; $n_3 = 1.3 + i 0.5$

turbation to the real part of the guide index due to the presence of absorption is negligible in most cases. However, while the perturbation on the imaginary part of a mode index is small, it still has a large effect on the resonance amplitude of the TFBG transmission spectrum. When there is a strong absorption due to certain resonance conditions, e.g. in case of the surface plasmon based sensors with over 40% of the modal light propagating in the outer layer, the strong interaction between the modal field and the lossy medium modifies even the real part of the index significantly as expected according to the Kramers-Kronig relation [74].

Like the lossless case, we employ Newton's method to find the transcendental roots for the lossy case. However, there is a key difference: the graphical method is not readily suitable to find the first approximation of the complex root of interest. Complex n_3 makes

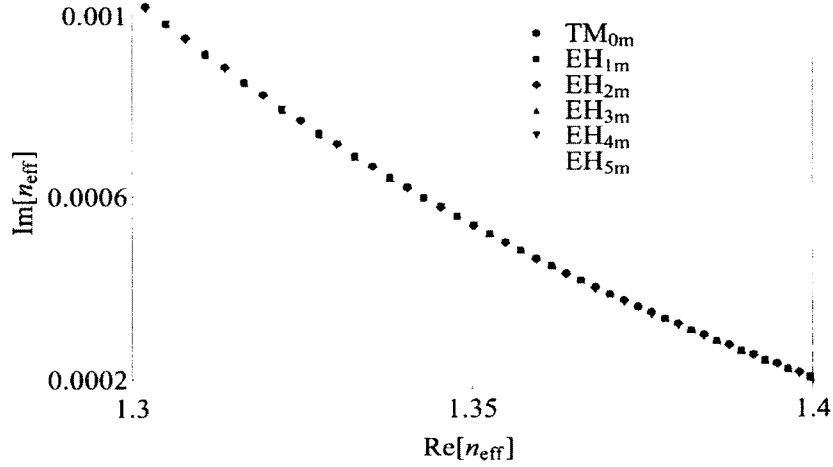


Figure 7: $\text{Im } n_{\text{eff}}$ for EH modes with $n_3 = 1.3 + i 0.1$

the phase parameter w_2 complex and results in a complex value for the dispersion relation. However in the case of a weak interaction, the first guess of the real part of the guide index can be found using the graphic method described in the previous section which still remains very close to the real part of the final solution. Once the first guess of the real part is found taking the real part of the dispersion equation, the Newton's method is then used to find simultaneous solutions involving the real and the imaginary part of the dispersion relation. In case of strong interaction, or if higher precision is needed, we take an iterative approach: we use the complex index found by using steps above as the guess root for successive iterations and again simultaneous solutions for the real and imaginary part of the dispersion relation are sought.

Figures 7 and 6 show two example cases with lossy third layer. In both cases the imaginary part of the n_3 is very large and corresponds to large loss coefficients of $\alpha = 4\pi n_{\text{img}}/\lambda = 40122.5\text{cm}^{-1}$ ($n_3 = 1 + 0.5i$) and 8024.5cm^{-1} ($n_3 = 1 + 0.1i$). The reason for choosing such a large imaginary index is to show the consistency and the accuracy of the model. We make two interesting observations here: first, for the same imaginary value of n_3 , the EH modes (and TM modes) are more lossy than the HE modes (and TE modes). This is consistent with the observation made in reference [75] for the planar waveguide. Second, the higher order radial modes carry more power in the evanescent tail than the low order modes and hence acquire higher loss factors as expected [39]; however, the azimuthal order of modes has negligible effect on the imaginary part of the index. Hence, nearly degenerate odd azimuthal order modes and nearly degenerate even azimuthal order modes can be thought of as having the same imaginary guide index.

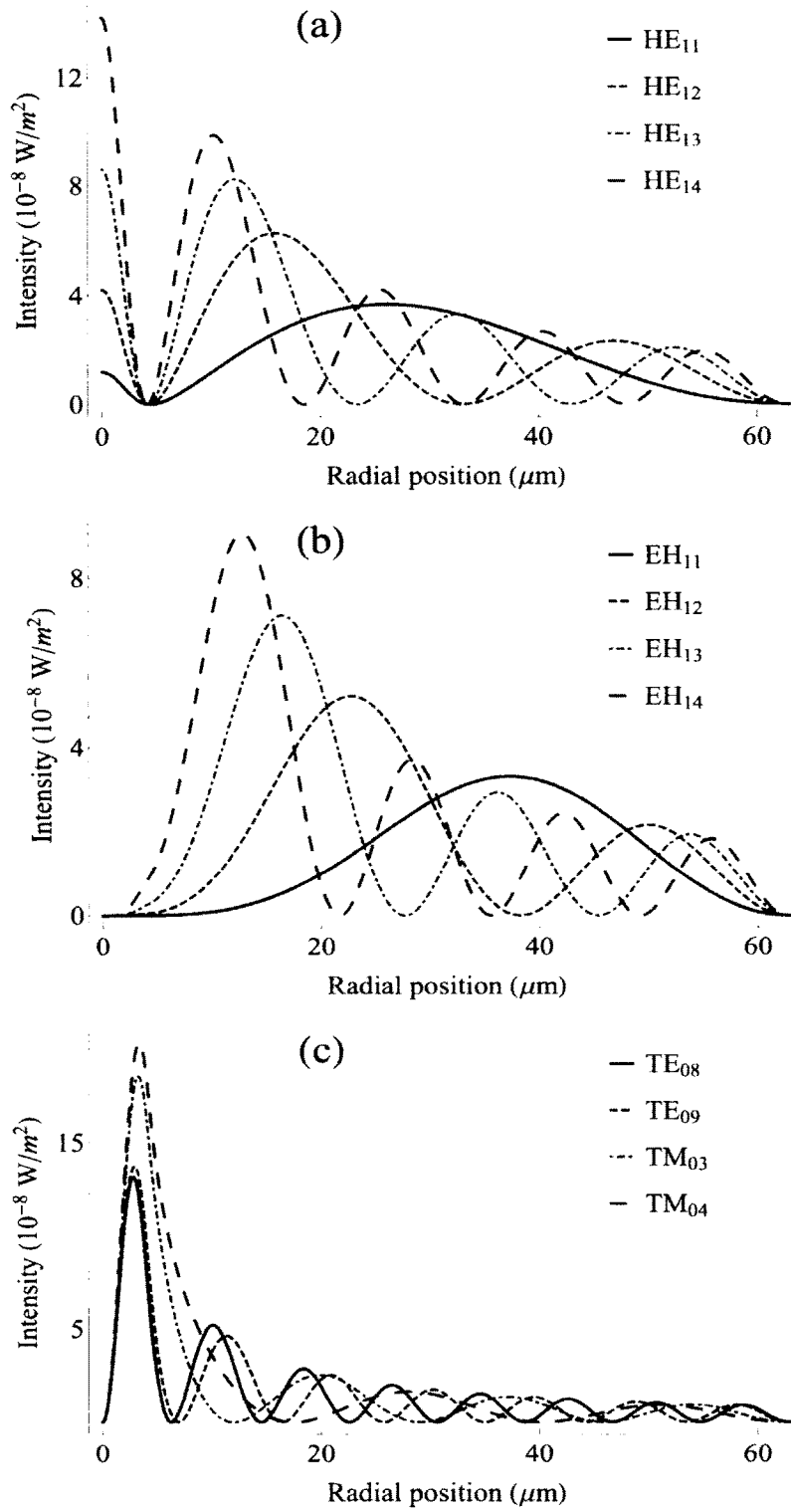


Figure 8: Plots of the local Poynting vector magnitudes as a function of radius of (a) $\text{HE}_{1m=1 \text{ to } 4}$, (b) $\text{EH}_{1m=1 \text{ to } 4}$, (c) TE_{08} , TE_{09} , TM_{03} , TM_{04} modes.

2.4 MODE FIELD AND THE POLARIZATION PROPERTIES

In Figure 8 we present the local Poynting vector magnitude of a few low order ($l = 1$ and 0) modes. The values were calculated using the following parameters: $a_1 = 4.1\mu\text{m}$, $a_2 = 62.5\mu\text{m}$, $n_1 = 1.45005$, $n_2 = 1.44359$, $n_3 = 1$ at $\lambda = 1586\text{nm}$. In this case, HE modes have a peak localized in the core whereas EH modes have very little light in the core. Transverse modes also have significant light in the core. In general, the coupling characteristics of any guided mode to another guided mode depends on the modal overlaps of the modes of interest. It will be shown in the next chapter that modal overlaps, and by extension, the coupling coefficient, depends on the amplitude of the field. In general, coupling coefficients, from core to the cladding modes in this case, are directly proportional to the field amplitudes in the core. Figure 9 depicts the fraction of power carried by each mode for the first ten azimuthal orders in the core. TE_{0m} and TM_{0m} modes have comparable power in the core. The situations are entirely different for hybrid modes. The fraction of power in the core for HE and EH modes are comparable only for high radial orders; for modes with low radial orders, the fraction of power in the core changes arbitrarily. These characteristics infer the necessity to treat such a structure as an exact three layer structure. Clearly, a perturbation approach for mode solution [76] (where the three layer structure is reduced to a multimode two layer one) or weakly guiding approximation would fail to elucidate the effect of the core on the cladding modes field distribution and coupling coefficient.

At this point we want to discuss the polarization properties of the cladding modes. As mentioned in the previous section, azimuthally non-variant, i.e. no Φ dependence, the TE_{0m} modes have no radial electric field component, hence the modes are always azimuthally polarized and as a result the electric field vector in the cladding outer layer is always tangent to the surface. The TM_{0m} modes have no azimuthal electric field components and as a result modes are always radially polarized. In this case the field at the cladding outer boundary is perpendicular to the interface. Figure 10 presents the vector field plot of TE_{010} and TM_{010} modes in the cladding region.

Hybrid modes have both radial and azimuthal components. Hence, by default, these classes of modes have no preferred polarization. The classification of hybrid modes based on the polarization properties was first proposed in [77]. However this view is problematic and is particularly inconsistent for the cladding region [70, 72]. Morishita noted that the polarization properties change remarkably based on the index distribution for the same structure [71] and proposed a new classification scheme by further dividing the mode types. In our view such a scheme provides nothing beyond negligible taxonomical advantages at the price of added complication. Hence we adopted

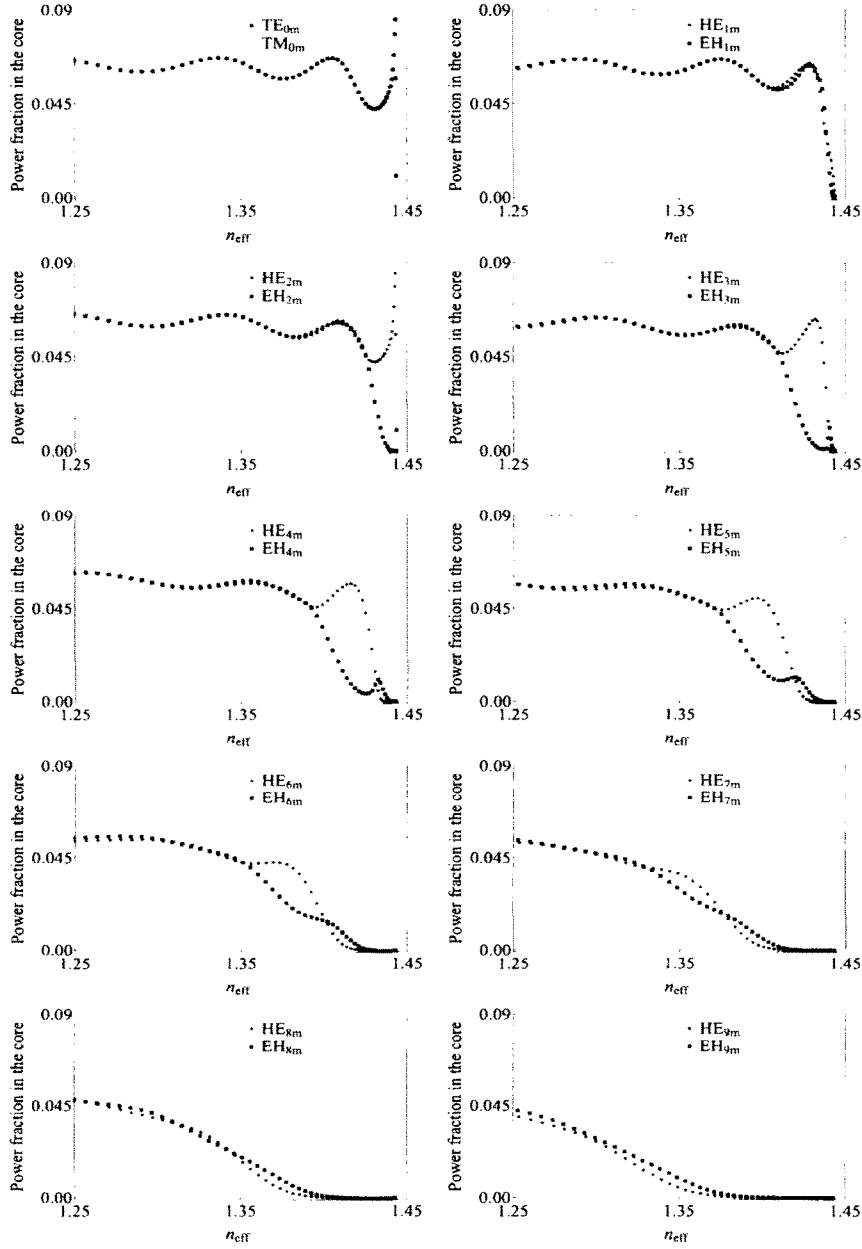


Figure 9: Plots of the fraction of the total power carried by fields of cladding modes in the core. Modes with high azimuthal order have less power in the core than modes with low azimuthal order. In general, only higher order radial modes for identical azimuthal order HE and EH modes carries similar amount of power. This generalization breaks down for low order radial modes.

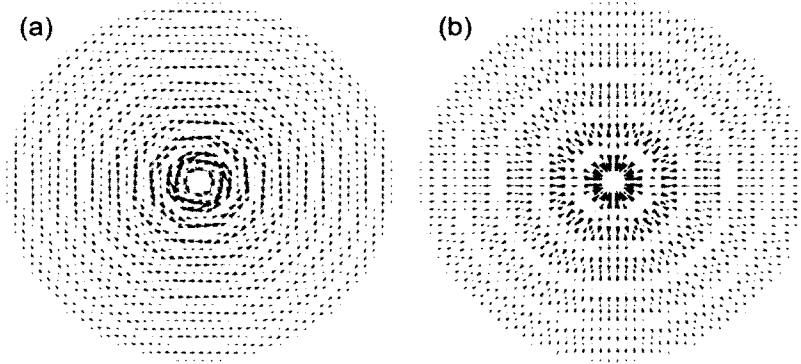


Figure 10: The vector field plot of the electric field of (a) TE_{010} and (b) TM_{010} cladding modes in the cladding. A transverse electric cladding mode is always azimuthally polarized whereas a transverse magnetic mode is always radially polarized.

the universal classification scheme solely based on the sign of the solution of the dispersion equation [73]. To understand the dominant polarization behaviour of the hybrid modes we calculate the fraction of the total power carried by the radial components of the electric field. By default, then, the azimuthal electric field component carries the remaining power based on the definition of the Poynting vector in the axial direction. The more dominant the radial component is, the more “TM-like” the mode is. Power in the radial component can be calculated using the following equation

$$\text{Fraction of power carried by } E_r = \frac{\int_0^\infty \int_0^{2\pi} E_r H_\phi^* r dr d\phi}{\text{TotalPower}} \quad (2.4.1)$$

Due to our choice of the normalization conditions the total power carried by each mode is 1W. In Figure 12 we present our calculations for hybrid modes with $l = 1$ to 8. The plot shows that, in a step index standard telecom fibre, in case of EH modes (HE modes) with lower effective indexes, i.e. higher order radial modes, for any azimuthal order, most of the power is carried by the radial component (azimuthal component) of the electric field vector. This remains consistent regardless of the wavelength of interest. Hence for all practical purpose HE modes (EH) modes in these fibres could be thought of primarily azimuthally (radially) polarized.

Another useful mechanism to visualize the polarization properties of the modes is to plot the vector field orientation at the cladding-outer layer interfaces. Figure 11 shows such a plot for $HE_{1,25}$ and $EH_{1,25}$. In this case $\psi = \pi/2$. It is clear from the image that for the HE (EH) mode the electric field vector is tangent (normal) to the surface. This view is consistent for any higher order radial modes for any azimuthal order. In fact, the polarization vector for HE modes at

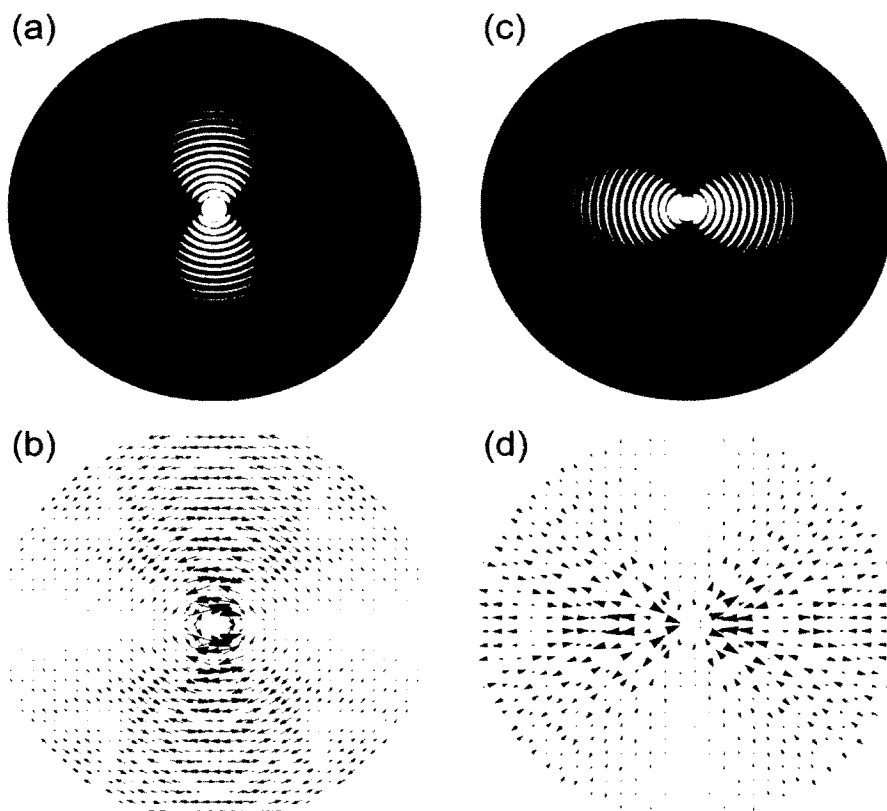


Figure 11: The intensity (a & c) and the vector field plots (b & d) in the cladding region for HE_{125} and EH_{125} respectively for $\Psi = \pi/2$. A pair of HE and EH modes of same radial and azimuthal order have exactly same intensity distribution and are mutually orthogonal. However, the underlying field pattern is very different from each other: HE is more TE like and EH more TM like

the cladding outer boundary at the intensity maximums are always tangential whereas for the EH case the vector is normal to the surface. As shown in Fig 12, for low order modes with guide index close to the core for each azimuthal order, HE modes contain a maximum of 50% TM and vice versa.

2.5 CLADDING MODE IN A FOUR-LAYER STRUCTURE

Figure 13 shows a generalized structure of a four layer fibre. There is nothing special about a four layer structure compared to a three layer structure. The field equations still need to satisfy the wave equation (2.2.2). The Debye potentials Φ and Ψ are now expressed as

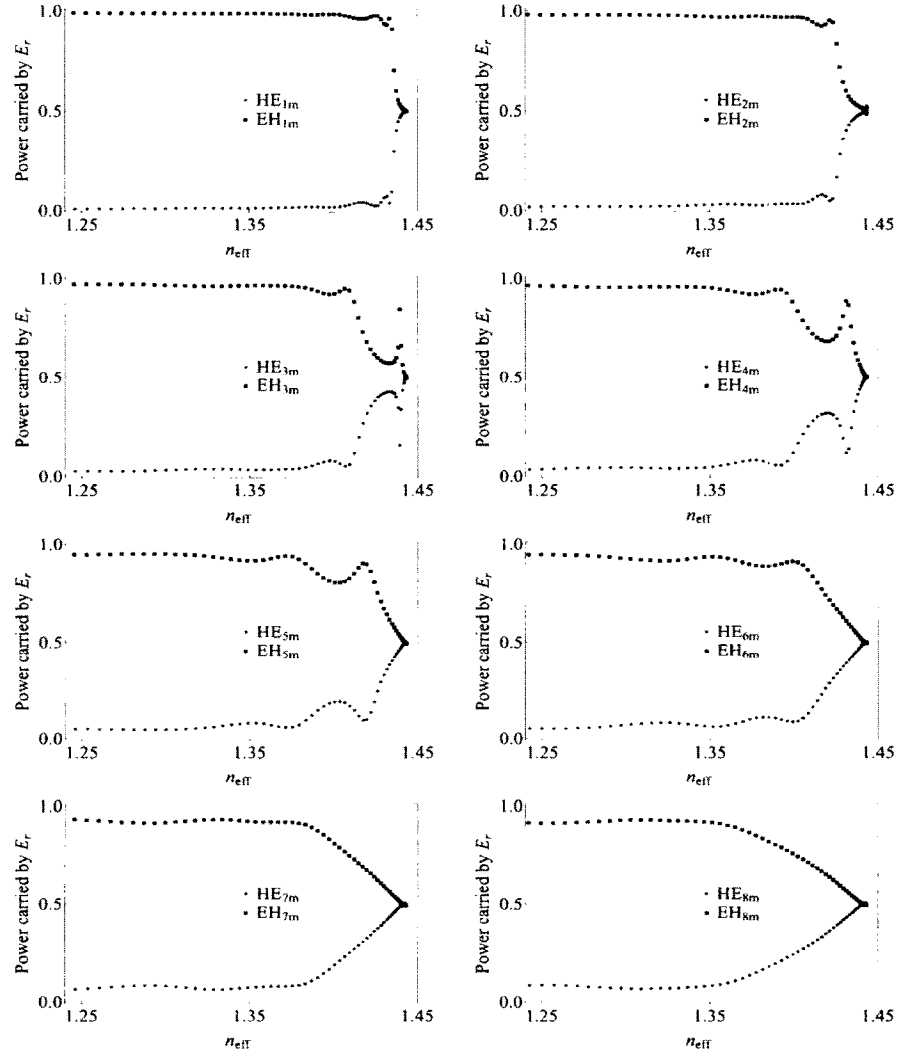


Figure 12: The fraction of total power carried by the radial component of each mode. For all practical purpose, apart from the low order radial modes, HE modes can be generalized to be azimuthally polarized and EH modes to be radially polarized

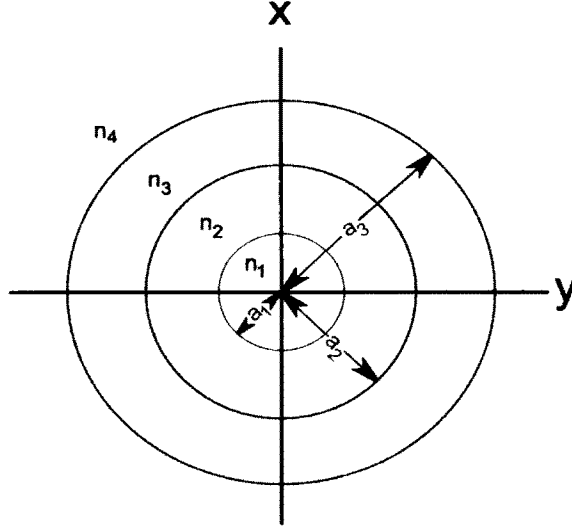


Figure 13: The generalized four layer fibre structure

$$\Phi_1 = A_1 J_1[u_1 r] \text{Exp}[il\phi] \quad (2.5.1a)$$

$$\Phi_2 = \{A_2 J_1[u_2 r] + B_2 Y_1[u_2 r]\} \text{Exp}[il\phi] \quad (2.5.1b)$$

$$\Phi_3 = \{A_3 J_1[u_3 r] + B_3 Y_1[u_3 r]\} \text{Exp}[il\phi] \quad (2.5.1c)$$

$$\Phi_4 = B_4 K_1[w_4 r] \text{Exp}[il\phi] \quad (2.5.1d)$$

$$\Psi_1 = C_1 J_1[u_1 r] \text{Exp}[il\phi] \quad (2.5.1e)$$

$$\Psi_2 = \{C_2 J_1[u_2 r] + D_2 Y_1[u_2 r]\} \text{Exp}[il\phi] \quad (2.5.1f)$$

$$\Psi_3 = \{C_3 J_1[u_3 r] + D_3 Y_1[u_3 r]\} \text{Exp}[il\phi] \quad (2.5.1g)$$

$$\Psi_4 = D_4 K_1[w_4 r] \text{Exp}[il\phi] \quad (2.5.1h)$$

In terms of Debye potentials field expressions then become

Core region: $r \leq a_1$

$$E_r = \frac{1}{ln_1^2 r} (C_1 l^2 n_1^2 J_1[u_1 r] + A_1 r u_1 \sigma_2 J_1'[u_1 r]) \text{Exp}[il\phi] \quad (2.5.2a)$$

$$E_\phi = -\frac{1}{n_1^2 r} (A_1 \sigma_2 J_1[u_1 r] + C_1 n_1^2 r u_1 J_1'[u_1 r]) \text{Exp}[il\phi] \quad (2.5.2b)$$

$$E_z = \frac{A_1}{ln_1^2 \beta} u_1^2 \sigma_2 J_1[u_1 r] \text{Exp}[il\phi] \quad (2.5.2c)$$

$$H_r = \frac{1}{lr} (A_1 l^2 J_1[u_1 r] - C_1 r u_1 \sigma_1 J_1'[u_1 r]) \text{Exp}[il\phi] \quad (2.5.2d)$$

$$H_\phi = \frac{1}{r} (C_1 \sigma_1 J_1[u_1 r] - A_1 r u_1 J_1'[u_1 r]) \text{Exp}[il\phi] \quad (2.5.2e)$$

$$H_z = -\frac{1}{l\beta} u_1^2 \sigma_1 J_1[u_1 r] \text{Exp}[il\phi] \quad (2.5.2f)$$

Cladding region: $a_1 \leq r \leq a_2$

$$E_r = \frac{1}{\ln_2^2 r} (C_2 l^2 n_2^2 J_1[u_2 r] + D_2 l^2 n_2^2 Y_1[u_2 r] + r u_2 \sigma_2 (A_2 J_1'[u_2 r] + B_2 Y_1'[u_2 r])) \text{Exp}[i l \phi] \quad (2.5.3a)$$

$$E_\phi = -\frac{1}{n_2^2 r} (A_2 \sigma_2 J_1'[u_2 r] + B_2 \sigma_2 Y_1'[u_2 r] + n_2^2 r u_2 (C_2 J_1'[u_2 r] + D_2 Y_1'[u_2 r])) \text{Exp}[i l \phi] \quad (2.5.3b)$$

$$E_z = \frac{u_2^2 \sigma_2}{\ln_2^2 \beta} (A_2 J_1[u_2 r] + B_2 Y_1[u_2 r]) \text{Exp}[i l \phi] \quad (2.5.3c)$$

$$H_r = \frac{1}{l r} (A_2 l^2 J[u_2 r] + B_2 l^2 Y_1[u_2 r] - r u_2 \sigma_1 (C_2 J_1'[u_2 r] + D_2 Y_1'[u_2 r])) \text{Exp}[i l \phi] \quad (2.5.3d)$$

$$H_\phi = \frac{1}{r} (C_2 \sigma_1 J_1[u_2 r] + D_2 \sigma_1 Y_1[u_2 r] - r u_2 (A_2 J_1'[u_2 r] + B_2 Y_1'[u_2 r])) \text{Exp}[i l \phi] \quad (2.5.3e)$$

$$H_z = -\frac{u_2^2 \sigma_1}{l \beta} (C_2 J_1[u_2 r] + D_2 Y_1[u_2 r]) \text{Exp}[i l \phi] \quad (2.5.3f)$$

Second cladding region: $a_2 \leq r \leq a_3$

$$E_r = \frac{1}{\ln_3^2 r} (C_3 l^2 n_3^2 J_1[u_3 r] + D_3 l^2 n_3^2 Y_1[u_3 r] + r u_3 \sigma_2 (A_3 J_1'[u_3 r] + B_3 Y_1'[u_3 r])) \text{Exp}[i l \phi] \quad (2.5.4a)$$

$$E_\phi = -\frac{1}{n_3^2 r} (A_3 \sigma_2 J_1'[u_3 r] + B_3 \sigma_2 Y_1'[u_3 r] + n_3^2 r u_3 (C_3 J_1'[u_3 r] + D_3 Y_1'[u_3 r])) \text{Exp}[i l \phi] \quad (2.5.4b)$$

$$E_z = \frac{u_3^2 \sigma_2}{\ln_3^2 \beta} (A_3 J_1[u_3 r] + B_3 Y_1[u_3 r]) \text{Exp}[i l \phi] \quad (2.5.4c)$$

$$H_r = \frac{1}{l r} (A_3 l^2 J[u_3 r] + B_3 l^2 Y_1[u_3 r] - r u_3 \sigma_1 (C_3 J_1'[u_3 r] + D_3 Y_1'[u_3 r])) \text{Exp}[i l \phi] \quad (2.5.4d)$$

$$H_\phi = \frac{1}{r} (C_3 \sigma_1 J_1[u_3 r] + D_3 \sigma_1 Y_1[u_3 r] - r u_3 (A_3 J_1'[u_3 r] + B_3 Y_1'[u_3 r])) \text{Exp}[i l \phi] \quad (2.5.4e)$$

$$H_z = -\frac{u_3^2 \sigma_1}{l \beta} (C_3 J_1[u_3 r] + D_3 Y_1[u_3 r]) \text{Exp}[i l \phi] \quad (2.5.4f)$$

Outer region: $r \geq a_3$

$$E_r = \frac{1}{\ln_4^2 r} (D_3 l^2 n_4^2 K_l[w_4 r] + B_4 r w_4 \sigma_2 K_l'[w_4 r]) \text{Exp}[il\phi] \quad (2.5.5a)$$

$$E_\phi = -\frac{1}{n_4^2 r} (B_4 \sigma_2 K_l[w_4 r] + D_4 n_4^2 r w_4 K_l'[w_4 r]) \text{Exp}[il\phi] \quad (2.5.5b)$$

$$E_z = -\frac{B_4 w_4^2 \sigma_2}{\ln_4^2 \beta} K_l[w_4 r] \text{Exp}[il\phi] \quad (2.5.5c)$$

$$H_r = \frac{1}{lr} (B_4 l^2 K_l[w_4 r] - D_4 r w_4 \sigma_1 K_l'[w_4 r]) \text{Exp}[il\phi] \quad (2.5.5d)$$

$$H_\phi = \frac{1}{r} (D_4 \sigma_1 K_l[w_4 r] - B_4 r w_4 K_l'[w_4 r]) \text{Exp}[il\phi] \quad (2.5.5e)$$

$$H_z = \frac{D_4 w_4^2 \sigma_1}{l\beta} K_l[w_4 r] \text{Exp}[il\phi] \quad (2.5.5f)$$

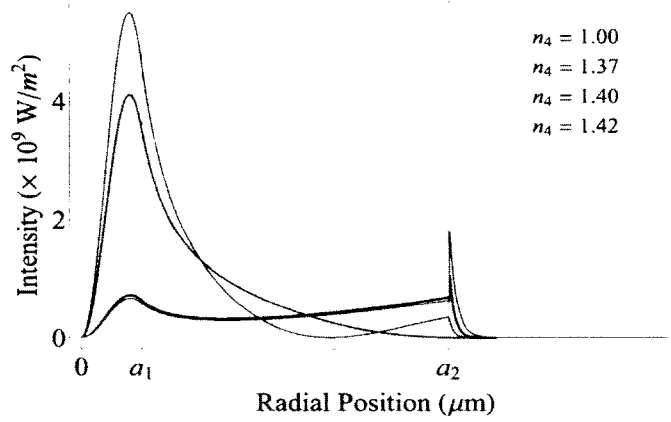


Figure 14: Intensity distribution of the TE_{01} cladding mode in a four layer structure. Here $a_1 = 4.1\mu\text{m}$, $a_2 = 25\mu\text{m}$, $a_3 = 25.05\mu\text{m}$. The refractive index (n_3) for the third layer is 2.1. Please note that smaller radii are chosen for the ease of visualization of the field intensity in the third layer. The third layer is too thin to be observable in the figure, however the effect on the field is clearly visible.

The rest of the procedure remains exactly the same as the three layered case. There is, however, one notable difference. For the three layer case, in general, we seek a cladding mode effective index value which lies between n_3 and n_1 . However, in a four layer case the index of the third layer can be lower, equal, or higher than the guided index of interest. This is especially of interest when we try to use this model for finding the unknown index of a very thin third layer. The above

expressions are valid for case when $n_{eff} \geq n_3$. A very thin high index ($n_3 \geq n_1$) third layer does not result in the cutoff of the guided mode in the cladding. If the $n_3 \geq n_{eff}$, the phase parameter u_3 becomes imaginary. To mitigate this problem we utilize the phase parameter $w_3 = 2\pi/\lambda(n_{eff}^2 - n_3^2)^{\frac{1}{2}}$ which is real in this case. Accordingly, we choose Bessel functions I and K for the third layer in equation 2.5.1 instead of Bessel functions J and Y along with phase parameter w_3 as argument [60] of these Bessel functions. This choice keeps all elements real and the field expressions and dispersion relations get modified accordingly. At the cross over point corresponding to $n_{eff} = n_3$ the solution for these two distinct expressions must agree with the either choices of the Bessel functions and the phase parameters for the continuity of the model. Mathematically at the crossover points the following asymptotic expressions are used, where $p \rightarrow 0$

$$I_l[p] = (\frac{p}{2})^l / \Gamma[l+1] \quad (2.5.6a)$$

$$I'_l[p] = 0.5(\frac{p}{2})^{l-1} / \Gamma[l] \quad (2.5.6b)$$

$$K_l[p] = 0.5\Gamma[l](\frac{p}{2})^{-l} \quad (2.5.6c)$$

$$K'_l[p] = -0.25\Gamma[l+1](\frac{p}{2})^{-l+1} \quad (2.5.6d)$$

$$J_l[p] = (\frac{p}{2})^l / \Gamma[l+1] \quad (2.5.6e)$$

$$J'_l[p] = 0.5(\frac{p}{2})^{l-1} / \Gamma[l] \quad (2.5.6f)$$

$$Y_l[p] = -(\frac{1}{\pi})\Gamma[l](\frac{p}{2})^{-l} \quad (2.5.6g)$$

$$Y'_l[p] = -(\frac{1}{2\pi})\Gamma[l+1](\frac{p}{2})^{-l+1} \quad (2.5.6h)$$

Here, $\Gamma[x]$ denotes the Gamma function and is equal to $(x-1)!$

COUPLING COEFFICIENT AND TRANSMISSION RESPONSE

The gratings tilt breaks the azimuthal symmetry of the fibre structure and enhances coupling to the cladding modes even with higher azimuthal order. TFBG couples the forward propagating core mode to the backward propagating cladding modes. In this chapter we utilize the field expressions presented in the previous chapter to show that, the cladding mode coupling can be controlled by controlling the orientation of the linearly polarized core modes with respect to the plane of the tilt of the grating. We present the coupling mechanism in section 3.1. We then present the transmission response of a TFBG using the coupled-mode theory and show that the two orthogonal polarization states (X- or Y-polarized) of the core mode excite a pair of spectrally separated cladding mode resonances made of either EH or HE modes, and thus TFBG allows for the selective excitation of modes with the radial or the azimuthal polarization.

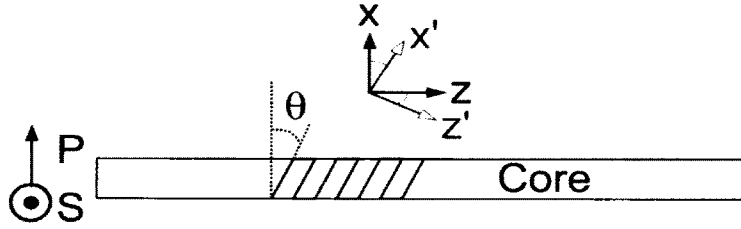


Figure 15: Configuration of the X-tilted gratings. "P" and "S" refers to the orientation of the P-polarized and S-polarized core mode electric vector respectively.

3.1 COUPLING COEFFICIENT

Due the weak index modulation of the gratings the coupling mechanism can be well modelled by the coupled mode theory. Following the definitions of Erdogan and Sipe [31], the coupling coefficient between two interacting modes in the presence of dielectric perturbations $\Delta\epsilon$ can be expressed by

$$\kappa_{12}^t(z) = (\omega/4) \int_0^{2\pi} \int_0^\infty \Delta\epsilon(r, \phi, z, \theta) \mathbf{E}_1(r, \phi) \cdot \mathbf{E}_2^*(r, \phi) r dr d\phi \quad (3.1.1)$$

where the superscript t denotes the transverse coupling coefficient and ω is the angular frequency in the free space. The gratings introduce only weak perturbation, hence the longitudinal coupling coefficient is two orders of magnitude smaller than the transverse components. Therefore, in this analysis we ignore all longitudinal interactions. Also we assume that our grating tilt is in the x - z plane. The dielectric perturbation due to the presence of the gratings $\Delta\epsilon(x, y, z, \theta)$ for the TFBG can be expressed as [31]

$$\begin{aligned}
 \Delta\epsilon(x, y, z, \theta) &= 2\epsilon_0 n_1 \delta n(x, y, z) \\
 &= 2\epsilon_0 n_1^2 \sigma v \cos(2K_g z') \\
 &= 2\epsilon_0 n_1^2 \sigma v \cos(2K_g(z \cos \theta - x \sin \theta)) \\
 &= \epsilon_0 n_1^2 \sigma \{ \exp[i2K_g(z \cos \theta - x \sin \theta)] \\
 &\quad + \exp[-i2K_g(z \cos \theta - x \sin \theta)] \}
 \end{aligned} \tag{3.1.2}$$

Converting all elements to the cylindrical coordinates

$$\begin{aligned}
 \Rightarrow \Delta\epsilon(r, \phi, z, \theta) &= \epsilon_0 n_1^2 \sigma \{ \exp[i2K_g(z \cos \theta - r \cos \phi \sin \theta)] \\
 &\quad + \exp[-i2K_g(z \cos \theta - r \cos \phi \sin \theta)] \} \\
 &= \frac{\pi n_1 \Delta n}{\lambda \omega Z_0} \{ \exp[i2K_g(z \cos \theta - r \cos \phi \sin \theta)] \\
 &\quad + \exp[-i2K_g(z \cos \theta - r \cos \phi \sin \theta)] \} \tag{3.1.3}
 \end{aligned}$$

Here $\delta n(x, y, z) = n_1 \sigma v \cos(2K_g z')$ is the induced index change at the core, σ is the slowly varying gratings profile and taken to be a constant for the uniform grating, z' is the axis of the grating which makes an angle, the grating tilt angle, θ with the fibre axis z , and $z' = z \cos \theta - x \sin \theta$ (Figure 15); v is the fringe visibility and taken to be unity; $K_g = \pi/\Lambda$ with Λ is the pitch of the gratings; $\Delta n = 2n_1 \sigma v$ is the ac index modulation; and θ is the tilt angle of the gratings. For simplicity we ignore the constant UV induced background dc index change and take ac index modulation to be of constant amplitude, i.e. no apodization. Using this expression for $\Delta\epsilon(r, \phi, z, \theta)$ in equation (3.1.1), the κ_{12} can then be expressed as summation of two components

$$\kappa_{12} = g_{12}^+ \exp(2iK_g z \cos \theta) + g_{12}^- \exp(-2iK_g z \cos \theta) \tag{3.1.4}$$

where,

$$g_{12}^\pm = \frac{\pi n_1 \Delta n}{4\lambda Z_0} \int_0^{2\pi} \int_0^{a_1} (\mathbf{E}_1 \cdot \mathbf{E}_2^*) \exp(\mp 2iK_g r \cos \phi \sin \theta) r dr d\phi \tag{3.1.5}$$

Higher Fourier components of the gratings are of negligible importance within the bandwidth of interest and hence we neglect those terms.

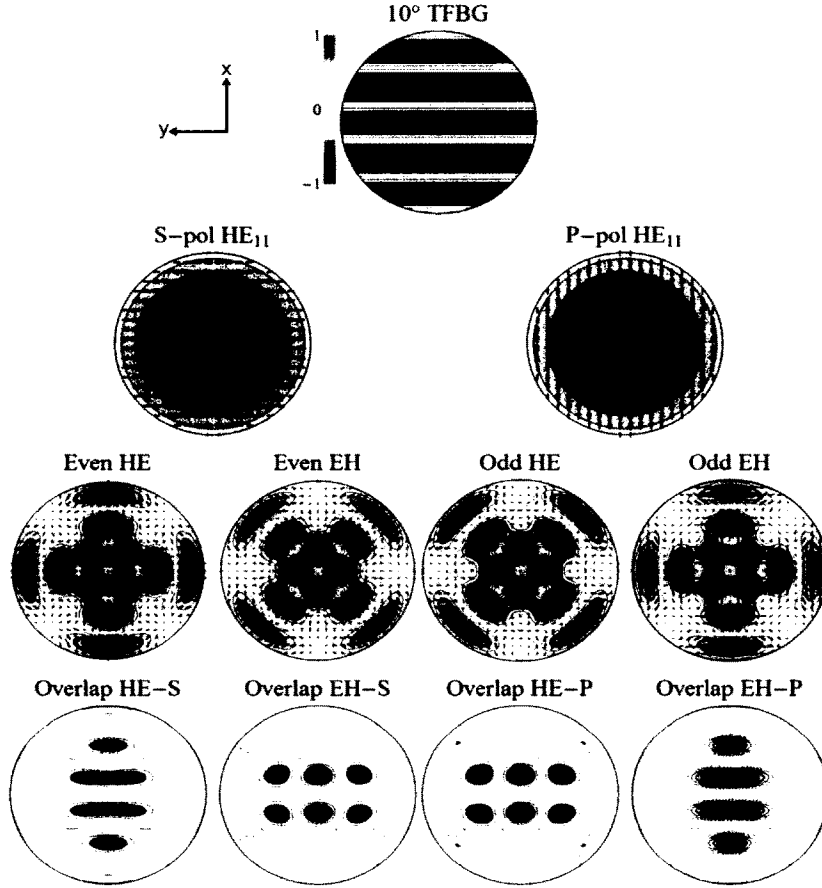


Figure 16: In the presence of the 10 deg tilted grating, P-polarized core mode (HE_{11}) couples dominantly to the odd EH_{2m} mode whereas the S-polarized core mode couples to the even HE_{2m} modes. The grating assisted overlap in other two cases are oscillatory and result in negligible integral value according to equation 3.1.5.

Under weakly guiding approximation, the core HE_{11} can be expressed as X- or Y- linearly polarized modes. In our core mode equations these two scenarios correspond to the cases where $\psi = 0$ and $\psi = \frac{\pi}{2}$ respectively. We assumed our gratings to be X-tilted by virtue of choosing $\cos \phi$ dependence in our gratings equations. Hence X-polarized (Y-polarized) HE_{11} mode is P-polarized (S-polarized) with respect to the grating (Figure 15). In reality, the core mode is not exactly linearly polarized, i.e. X-polarized (Y-polarized) core mode always contains some components in the y direction(x direction). However, such components are rather very small and we ignore them. The

magnitude of the coupling coefficient is the result of the interplay not only between the electric field intensities of the cladding modes in the core but also on the vectorial distributions of the modes of interest. The vectorial distribution ensures that the S-polarized core mode couples primarily to the odd HE modes and P-polarized core mode couples to the even EH modes. As an example, the Figure 16 shows the 10 deg grating assisted coupling interactions between HE_{11} core mode and HE_{243} ($n_{eff} = 1.3333$), and between HE_{11} core mode and EH_{244} ($n_{eff} = 1.3329$) for both P and S polarization. These two cladding modes are two consecutive solutions of the dispersion relation equation 2.2.14. In the presence of the dielectric perturbation S-polarized HE_{11} has maximum overlap with the even HE_{243} and minimum overlap with the even EH_{244} modes. The overlap with the even EH_{244} mode is oscillatory and hence results in a small value through the integral relationship of equation 3.1.5. The scenario is completely reversed for the P-polarized case where the maximum coupling happens for the EH_{244} odd mode.

More interestingly, even the weakest tilt distinguishes completely between the circularly symmetric TE_{0m} and TM_{0m} cases. In this case the P-polarized (S-polarized) core mode couples only to the radially polarized TM_{0m} (TE_{0m}) and no cross couplings are allowed. The coupling to the hybrid modes with any azimuthal or radial order also depends on the polarization nature of the mode, i.e. how "TE" or "TM" like the mode is.

As examples we include the coupling for the 10° tilt angles in Figures 17 and 18. In both cases the magnitude of the index perturbation is taken to be 5×10^{-3} . As shown in the previous chapter, modes with ($l \neq 0$) effective guide index close to the core index have weak preferential polarization, i.e. radial and azimuthal electric field components are equally strong. Therefore, the core mode couples strongly with these modes regardless of the polarization orientation. However, a 10° tilted grating suppresses coupling to most of these modes. Moreover the strongest coupling occurs for modes of the first ten azimuthal orders only. This is not surprising and is consistent with the Figure 9 which shows that higher order modes have less power in the core. Hence, coupling coefficients of modes of a particular azimuthal order are function of grating tilt, power in the core, and the relative strength of the azimuthal (or radial) component of the electric field of the mode. This feature is also evident in the coupling coefficient plots. Modes with no preferential polarization, i.e. with both strong radial and azimuthal electric field components, couple equally strongly for both P and S-polarized cases. However modes with index away from the core have strong preferential polarization resulting in the strong polarization dependent coupling.

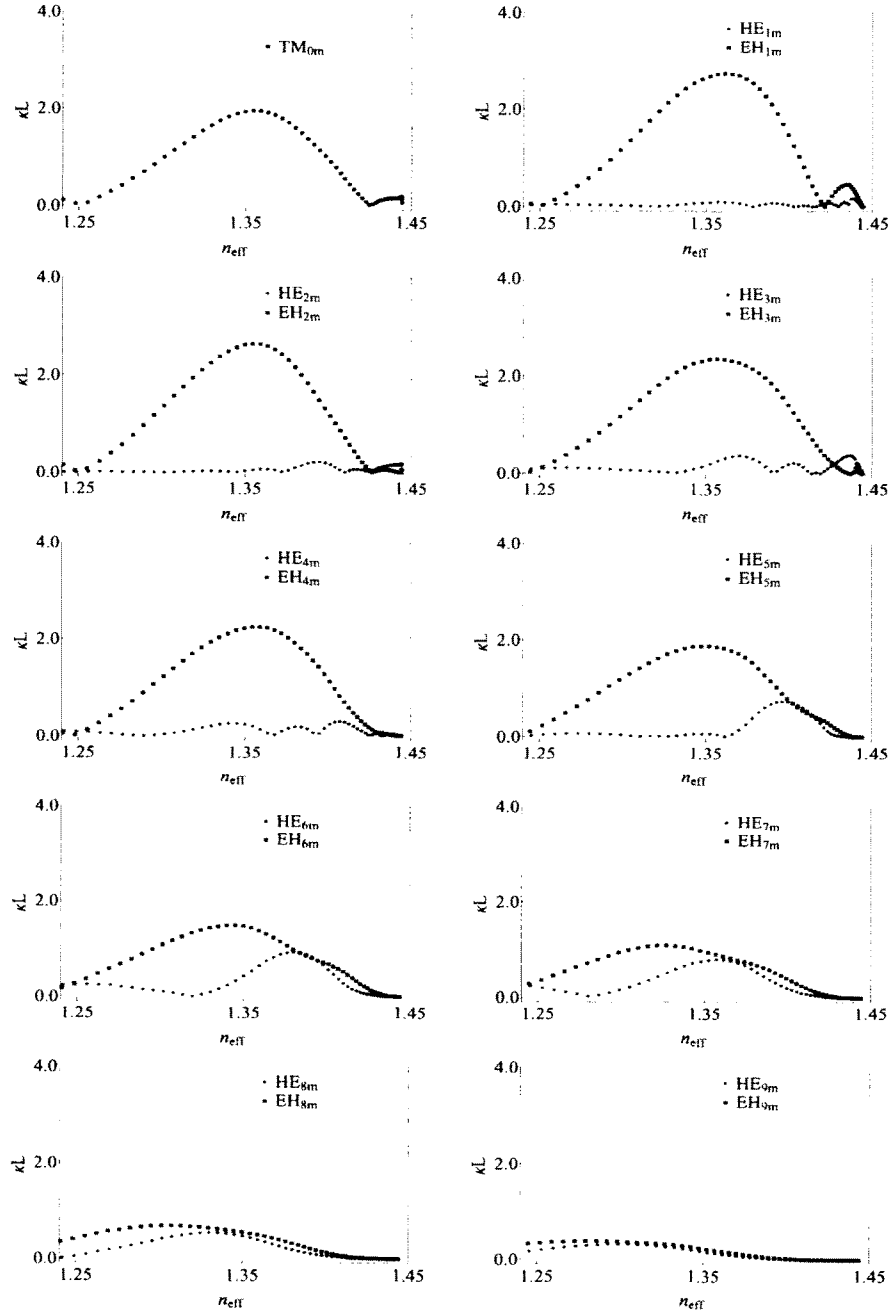


Figure 17: The coupling coefficients for the P-polarized core mode for 1 cm long grating with 10° tilt.

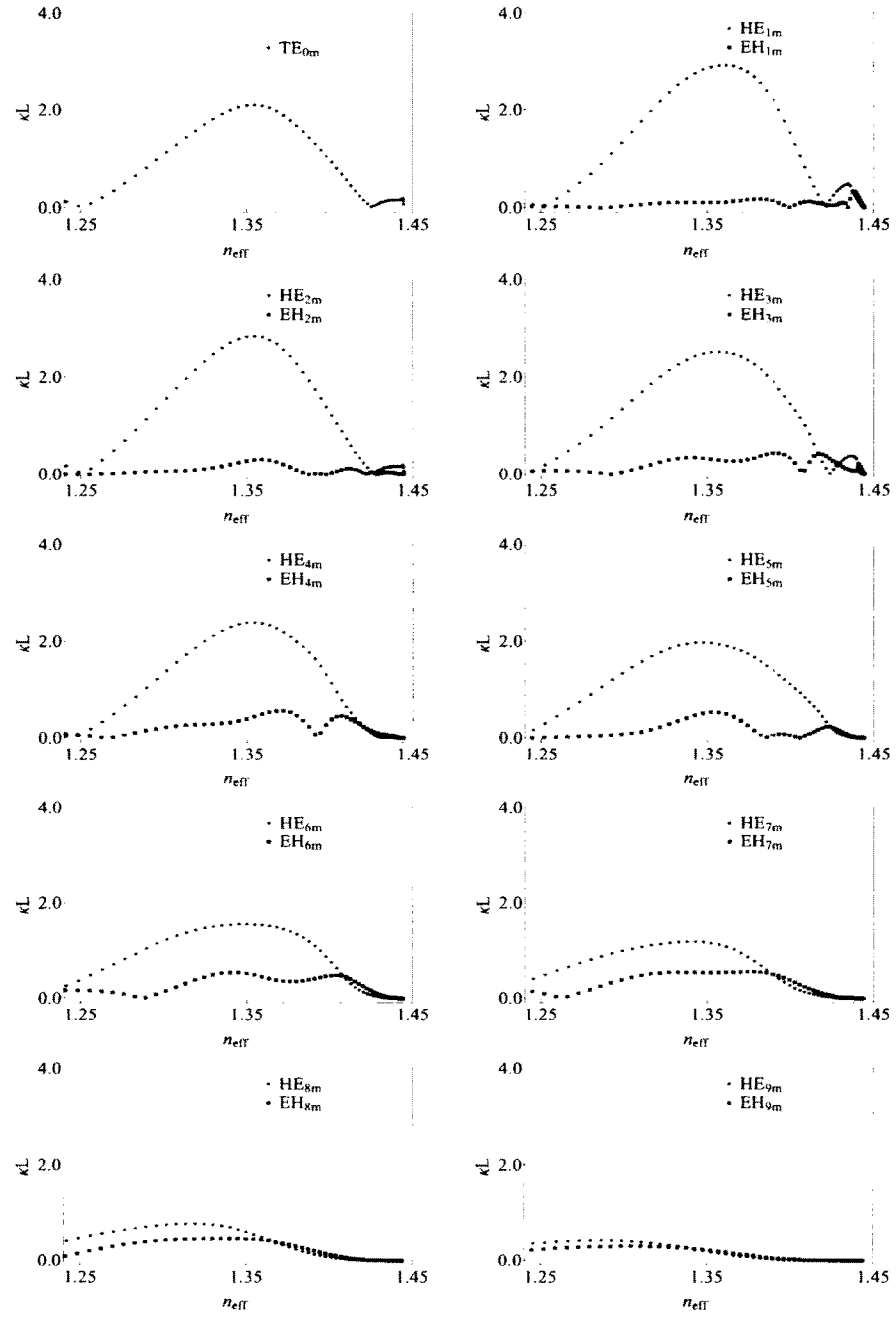


Figure 18: The coupling coefficients for the S-polarized core mode for 1 cm long grating with 10° tilt.

3.2 TRANSMISSION RESPONSE

Once the coupling coefficients are determined, the transmission spectra can be calculated by solving a set of simple coupled equations which describe how the slowly varying amplitude of the core mode $u(z)$ couples to any cladding mode with amplitude $v_{lm}(z)$ in the presence of the grating induced dielectric perturbation. By ignoring all losses and utilizing slowly varying wave approximations and appropriate relations, the coupled-mode equations can be expressed into the following simple form [78]

$$\frac{du}{dz} = - \sum_{l,m} jg^+ v_{lm} \exp(j2\delta z) \quad (3.2.1)$$

$$\sum_{l,m} \left[\frac{dv_{lm}}{dz} \right] = jg^- u \exp(-j2\delta z) \quad (3.2.2)$$

where $u(z)$ and $v(z)$ denote the forward travelling core mode and the backward travelling cladding modes respectively, and $2\delta = \beta_u + \beta_v - 2K_g \cos \theta$ is the grating assisted phase matching parameters, and β is the propagation constant of a mode. At $\delta = 0$, grating period $\Lambda = \lambda(n_{eff,core} + n_{eff,clad})$ dictate the phase matching wavelengths for the cladding modes. The boundary conditions for a grating of length L are: $u(z = -L/2) = 1$, $v(z = L/2) = 0$.

The set of equations 3.2.1 describes the interaction of a large number of modes through coupled first order differential equations. In the previous chapter we showed that for 10° tilted gratings the core mode interacts strongly with cladding modes with azimuthal order upto 10. Hence the calculation of the transmission spectrum requires the solution of the first order differential equations with at least over 1000 modes. Moreover the solutions need to be computed at each wavelength. Hence the difficulty of solving the coupled-mode equations depend on the strength and the spectral density of resonances [65]. However this computational problem is greatly simplified by recognising that the discrete modal solutions for the cladding modes results in modes which are nearly degenerate. Thus, for any wavelength modes with the smallest detuning parameter δ are of interest. Even then, if the material dispersion cannot be ignored, which is the case for a 10° tilted gratings since the spectral response spans over 100 nm bandwidth, the calculation still remains challenging.

We calculate the transmission spectrum using the following procedure:

1. First we look for the modal solution of using the dispersion relation. If the material dispersion can be ignored, this can be done only at the Bragg wavelength for modes of all radial and azimuthal order. If the material dispersion cannot be ignored, or

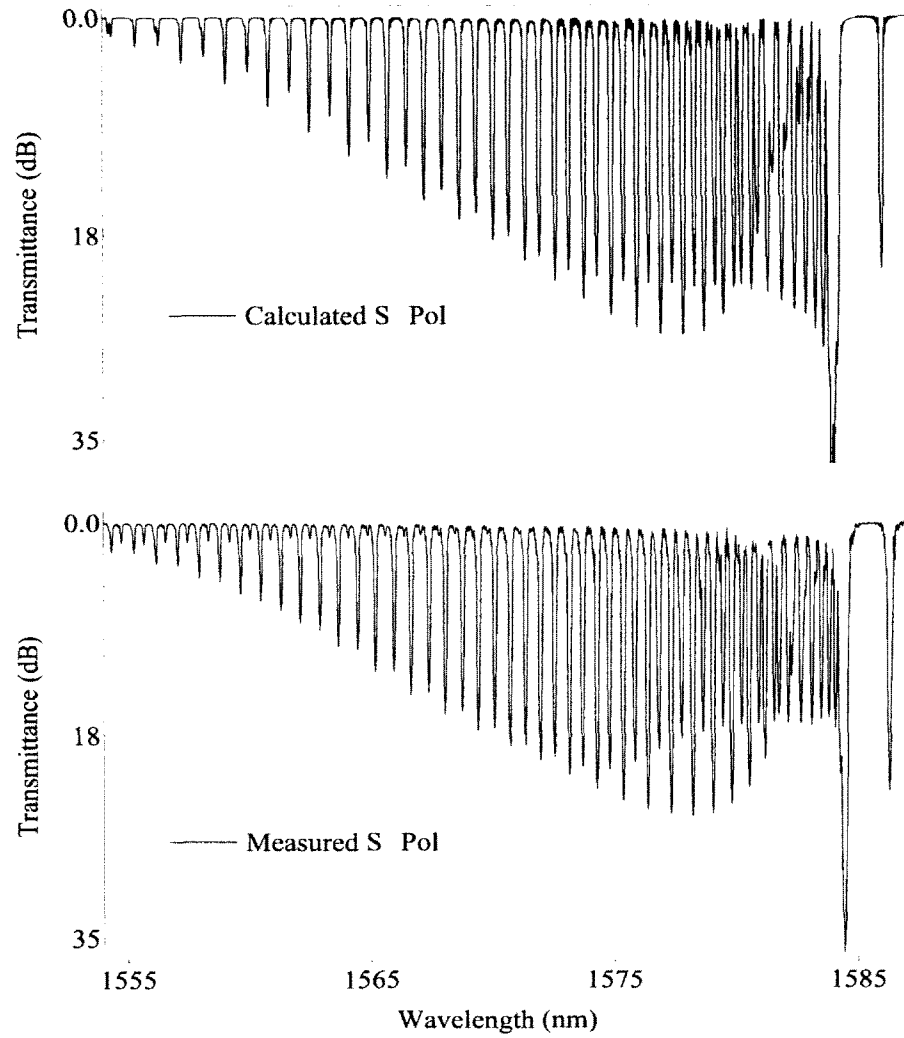


Figure 19: The calculated and the measured spectra of 1 cm long 4° TFBG with S-polarized core mode. We obtain the calculated spectrum by ignoring material dispersion and including modes with azimuthal order of $l = 0$ to 5.

high accuracy is desired we look for modes at each wavelength (pm) that satisfy the momentum conservation requirement of the gratings interaction, i.e., $\delta = 0$.

2. We calculate the coupling coefficient of each of these modes
3. We estimate the bandwidth of a resonance for each mode based on the closed-form expression of the coupled-mode equations involving two modes [65]:

$$\frac{\Delta\lambda_0}{\lambda} = \frac{\delta n}{n_{eff}} \sqrt{1 + \left(\frac{\lambda_D}{\delta n L}\right)^2} \quad (3.2.3)$$

where λ_D is the design wavelength, i.e. the wavelength where for the mode of interest $\delta = 0$; L is the length of the gratings; and $\frac{\Delta\lambda_0}{\lambda}$ is the normalized bandwidth.

4. Knowing the bandwidth, we can group the modes for which the resonances overlap. This allows us to include only the modes which are of interest.
5. We subsequently solve a set of coupled mode equations involving all modes of interest in a particular wavelength.

Figure 19 shows the calculated and the experimental spectra of a 4° TFBG for the S-polarized core mode. Figure 20 shows the calculated spectra of 10° gratings for both S- and P-polarized core modes. For the case of 4° TFBG, we calculate the spectra using modes of azimuthal order less than 6 whereas for the 10° case we include modes up to azimuthal order of 13, that is including a total of over 1600 modes. We ignore material dispersion for both cases and assume gratings to be of 1 cm in length.

In Figure 21 we present the dispersion compensated partial transmission spectra of a 10° tilted 4mm long grating. The cladding mode index distribution has a chirp i.e. high index modes of the same azimuthal order are more closely spaced together. This along with the preferential polarization properties of the higher radial order hybrid modes introduces a complete split in the resonance transmission spectra of the TFBG at shorter wavelengths depending on the core mode polarization orientation with respect to the plane of the tilt of the gratings. TFBG with 10° tilt allows strong coupling into these higher order radial modes. Figure 21 shows the split in a group of cladding mode resonances. For these classes of resonances P-polarized core mode couples dominantly to EH_{lm} and TM_{0m} modes and S-polarized core mode couples to HE_{lm} and TE_{0m} modes. The coupling to the HE_{lm} (EH_{lm}) for P-polarized (S-polarized) core mode are, at least, an order of magnitude smaller, and hence can be totally ignored for all practical purpose. Moreover for both P- and S-polarized cases, odd

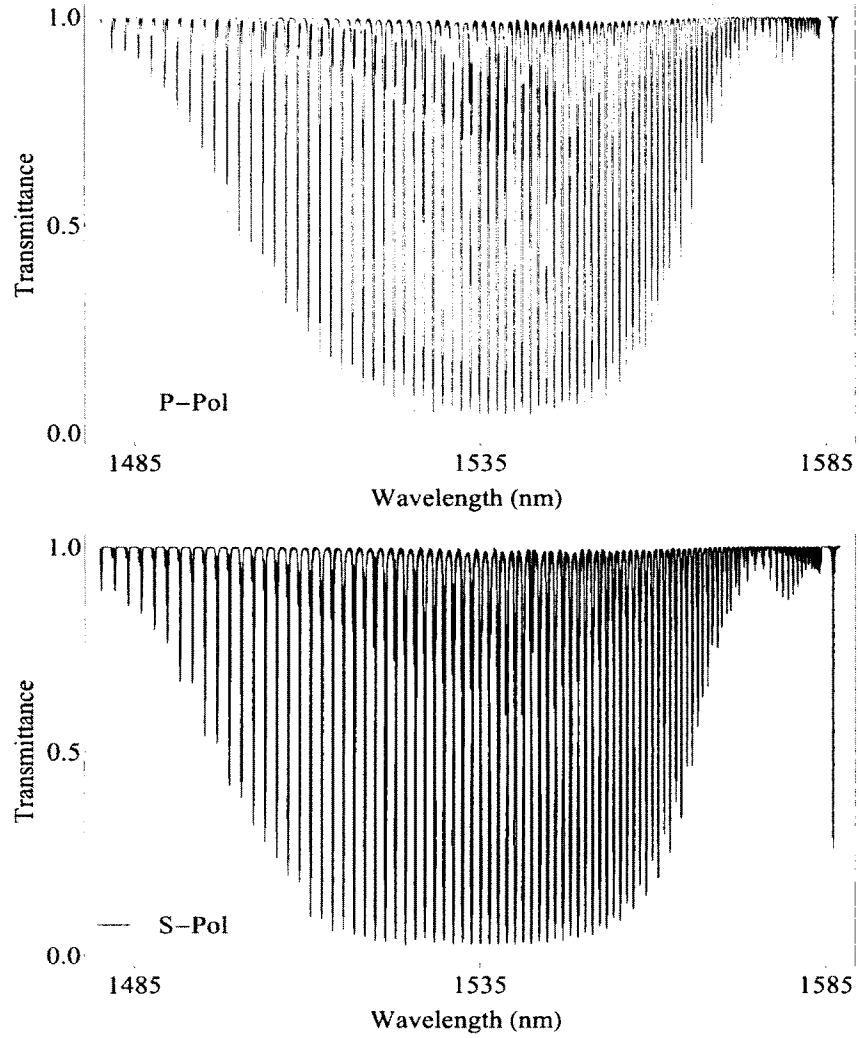


Figure 20: The calculated transmission spectra of a 1 cm long 10° TFBG for the S- and P-polarized cases. We obtain the calculated spectra by ignoring material dispersion and including modes with azimuthal order $l = 0$ to 13 using over 1600 modes.

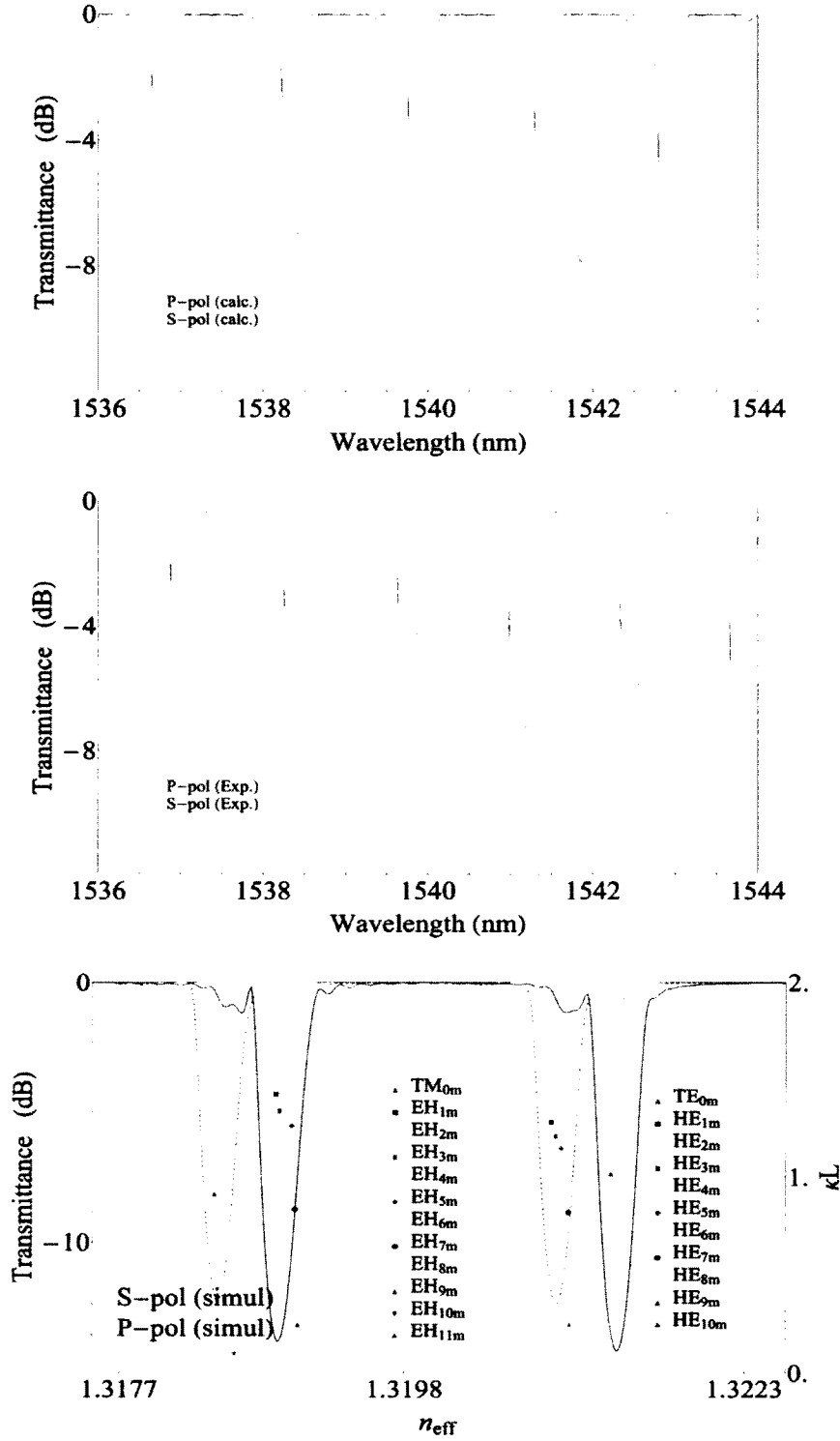


Figure 21: First two panel shows the calculated and the experimental partial transmission spectra of 10° tilted 0.4 cm long TFBG with $\lambda_{\text{Bragg}} = 1610$ nm. S- and P-polarized resonances are spectrally well separated. Bottom image shows the dominant modes and typical coupling coefficient for 1 cm long gratings.

azimuthal order and even azimuthal order (including zero) modes are nearly degenerate and form alternating resonance dips.

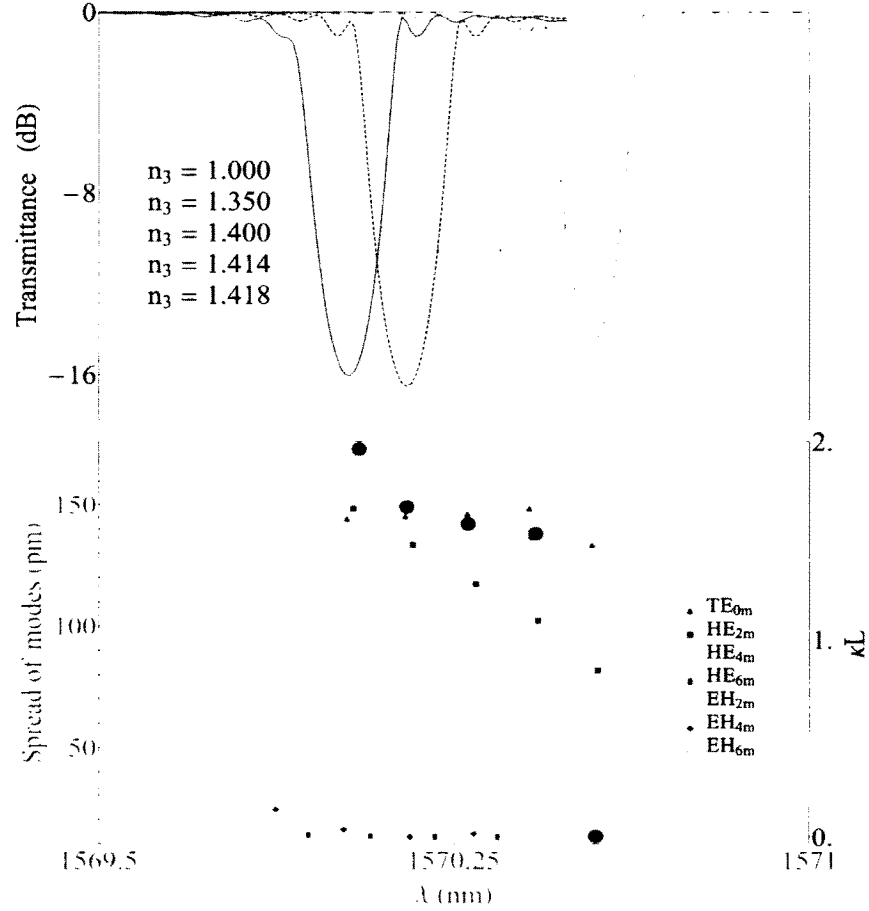


Figure 22: Evolution of a cladding resonance ($n_{eff} = 1.4169$), coupling coefficient of the constitutive modes, and the maximum index variation of the constitutive modes (spread of modes) as a function of surrounding medium index for a 4° TFBG. The slight sharpening of the resonances with high n_3 occurs despite decreasing coupling coefficient due to bunching of modes.

Our result is consistent with the experimental evidences put forward in [45]. In the reference [45] the authors demonstrated the excitation of the surface plasmon in a gold coated cladded fiber with a TFBG. They experimentally demonstrated that the plasmon could only be excited when the polarization of the core mode at the gratings are P-polarized with respect to the plane of the tilt of the gratings and as a result the transmission spectrum exhibits strong suppressions of cladding resonances. To excite plasmon on the gold coated surface one requires radial polarization. Since S-polarized modes couple to the azimuthally polarized HE and TE cladding modes, these sets of

modes, despite being spectral neighbours to EH and TM modes respectively, are unable to excite surface plasmon.

We now want to briefly examine the effect of the index change on the cladding mode resonance. Chan et al. in the ref. [39] reported that with the change in the external index, the sharpness of cladding mode resonances increases and then right before the cutoff, the resonance amplitude decreases. We investigate this effect in a 4° tilted grating by varying the value of n_3 , i.e. the index of the outside medium. We present the results of our calculation in the Figure 22. Each resonance is made of modes of many different azimuthal orders. A higher azimuthal order mode is slightly more sensitive, hence it gets perturbed more with the change in the index compared to a low azimuthal order mode. However the difference in sensitivity can be appreciated only either near cutoff, or especially for modes with large azimuthal order mismatch, e.g. $l = 1$ to $l = 7$. The variation in the n_3 value has two folded effect: first, the coupling coefficient of some of the constitutive modes decreases with the increasing index. As n_3 increases, fraction of power in that layer increases, this decreases power in the core for this mode, resulting in the lower overlap value, i.e. the coupling coefficient goes down. Second: due to the difference in sensitivity among the constitutive modes of a resonance, the overall effective index spread of these modes goes down, i.e. modes become closely packed in the effective index space, or become more degenerate. This subtle change in the modal effective index spread over compensates the drop in the coupling coefficient and the overall resonances gets slightly sharper. As the value of n_3 increases further and approaches the cutoff value of the modes, sensitivity between modes of different azimuthal order gets more prominent, and as a result, higher azimuthal order modes satisfy the cutoff conditions with lower n_3 value. Thus near cutoff the resonance depth decreases since now, both the number of the constitutive modes and coupling coefficient of each modes are lower.

Finally in Figure 23 we plot the simulated response of a pair of P and S resonances with effective index of 1.3042 and 1.3047 respectively with respect to the change in outside index. In this plot the Y-axis corresponds to the relative position change with respect to the Bragg wavelength and the X-axis corresponds to the index change in the outer medium. These two resonances are made of modes of same azimuthal order, but of different polarization; despite being immediate neighbour in terms of the wavelength location in the TFBG transmission spectra, the resonances excited by the P-polarized core modes shows slightly more sensitivity to the external index change than the resonances excited by the S-polarized core mode. As the modes approaches cut-off both resonances overlap each other. This can be understood by the fact as the index difference between the

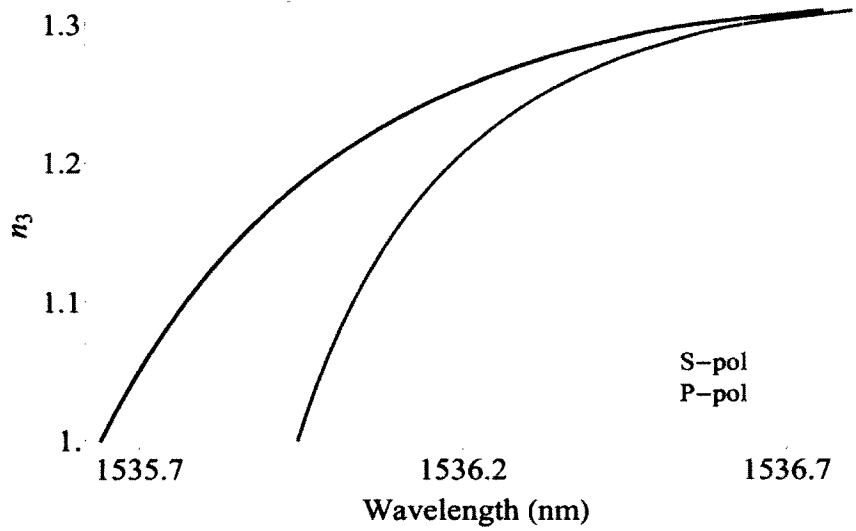


Figure 23: The Response of the (10°) S-pol and the P-pol resonances as functions of n_3 . The resonances contain modes with effective indexes of ~ 1.3042 (P-polarized) and ~ 1.3047 (S-polarized) respectively and the resonances lie beside each other in the transmission spectra. Resonances excited through P-polarized modes move more and near cutoff overlaps with S-polarized modes

cladding and the outside medium decreases, the effect of the boundary becomes weak, i.e. modes become weakly guided and degenerate.

3.3 COMMENTS

In the last two chapters we have presented the complete vectorial mode coupling properties of weakly tilted fiber Bragg gratings. We started the discussion by solving the dispersion equation of a three layer fibre structure for the cladding modes. We have presented a simple sign convention to distinguish between the hybrid nature of the cladding modes and then investigated the polarization properties of these cladding modes. The four classes of cladding modes are radially polarized TM_{0m} modes, azimuthally polarized TE_{0m} modes, and hybrid HE and EH modes. Hybrid modes with high radial order have preferential polarization in a sense that over 95% of total power is carried by the radial or the azimuthal components. Hence for all practical purpose these modes can be regarded as completely radially or azimuthally polarized.

The tilted grating break the symmetry of the fibre structure and show a complete preferential coupling properties for the TE_{0m} and TM_{0m} modes based on the orientation of the polarization vector of the core mode with respect to the plane of the tilt of the gratings. Coupling to any hybrid modes is also a function of the polarization orientation of the core mode. The HE and EH modes of a particular

radial order are the two orthogonally polarized nearly degenerate solutions of the eigenvalue equation for the same azimuthal order. However, their separation increases with the radial order; so does the absolute polarization preference. More interestingly, tilted gratings even with a relatively weak tilt allows selective coupling to either the azimuthally polarized HE or to the radially polarized EH modes. Therefore, each resonance excited by the core mode is either radially or azimuthally polarized. In the next chapter we use this property to investigate carbon nanotube thin film growth on the cladding of the fibre.

CHARACTERIZATION OF THE SWCNT COATING ON OPTICAL FIBRE

In this chapter we present the study of the interaction between the single-wall carbon nanotube deposited on the cladding of standard telecom fibre and the TFBG. We investigate the evolution of the linear optical properties and the thickness of the SWCNT thin-film growth using the spectral response of TFBG. We begin the chapter by presenting the deposition technique and, then, proceed to present the results of our analysis. Interestingly, our experimental results show high polarization dependent loss of randomly oriented carbon nanotube thin films; and more importantly, the difference in polarization dependent loss decreases rapidly and after a certain critical thickness the difference is negligible. However the film shows no birefringence.

4.1 CNT DEPOSITION

We deposit SWCNT on the cladding of fibres using the “dip-coating” method. We use high purity, greater than 90 mass%, SWCNT's of approximately 1.3 nm in diameter and about 1 μm in length for this purpose. Nanotubes are produced using the laser-oven method at the National Research Council, Canada [79]. The mixture has a ratio of semiconducting nanotubes to metallic nanotubes of roughly 2 : 1. The deposition process requires the preparation of the CNT suspension in DMF (N, N-dimethylformamide) solution. We deposit SWCNT on the cladding of the fibre with 1cm long 4° tilted gratings with Bragg wavelength at $\sim 1586\text{ nm}$. The gratings are fabricated by side exposing the fibre to a 248nm pulsed KrF (Krypton fluoride) Excimer laser beam diffracted off a phase mask [30].

The “dip-coating” process involves the following steps (Figure 24):

1. We functionalized $\sim 10\text{mg}$ of SWCNT's using bath sonication in 70% nitric acid for 2 hours. This acid treatment creates defect sites in the CNT structure.
2. We recover the nanotubes by filtration.
3. To get rid of excess nitric acid, we rinse the SWCNTs using nanopure water ($18.2\text{M}\Omega - \text{cm}$ ionic purity) through sonication for ~ 2 hours.
4. We then re-disperse the SWCNTs in 10mL DMF solution. The acid treated nanotubes disperse readily in the DMF solution

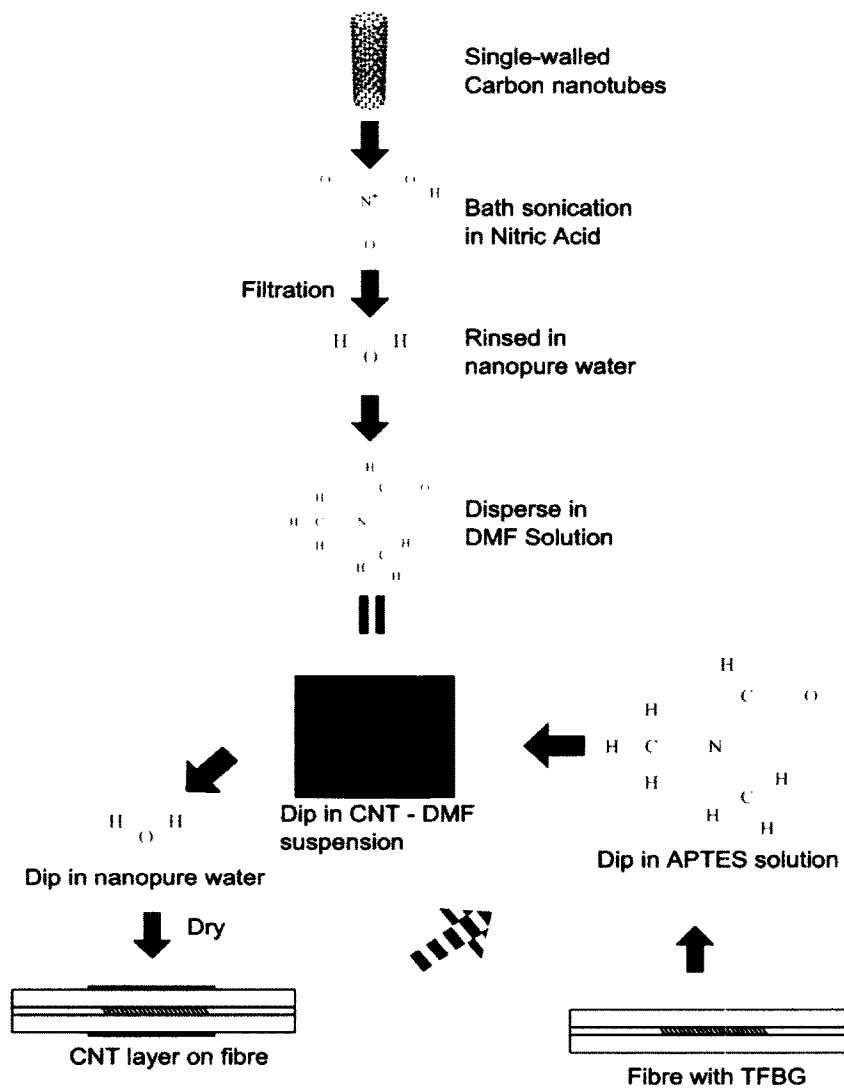
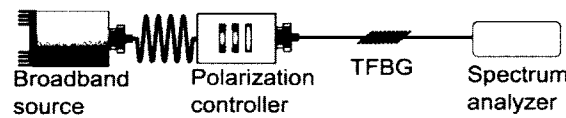


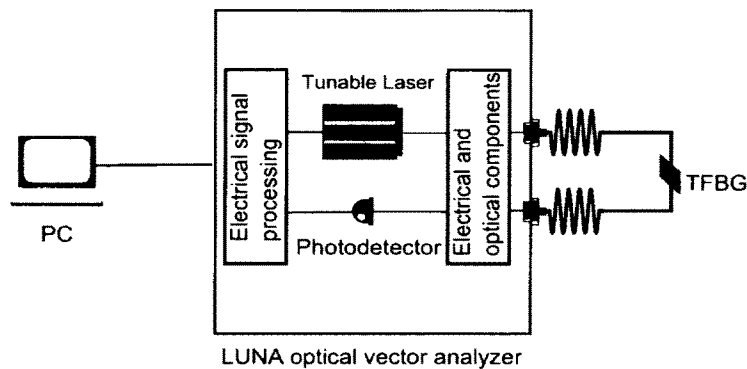
Figure 24: Preparation of the SWCNT-DMF suspension. We deposit CNT on the fibre surface through repeated sequential dipping in APTES solution, CNT-DMF suspension, and in nanopure water.

and produce optically black thick suspension. This process creates COOH-functionalized negatively charged SWCNTs.

5. To introduce adsorption of the SWCNTs, we need to functionalize the surface of the fibre. We accomplish this by dipping the fibre in 0.1wt% aqueous APTES (3-Aminopropyltriethoxysilane) solution for ~30 seconds. This process produces amino-terminated, silanized positively charged surface.
6. We submerge the functionalize fibre in the DMF-CNT suspension for ~1 minute. The positively charged fibre surface readily adsorbs negatively charged functionalized SWCNTs.
7. In the final step we submerge the fibre into the nanopure water to homogenize the distribution and to get rid of any loosely connected nanotubes and then finally air dry the fibre.
8. We then repeat the entire dipping cycle to increase the thickness of the nanotube layer.



(a)



(b)

Figure 25: The polarization dependent response can be measured two ways: (a) using a broadband source, polarization controller and a spectrum analyzer; or (b) using a LUNA's Optical Vector Analyzer

In general, the polarization dependent response of the TFBG can be obtained experimentally by launching polarized light in the fibre and ensuring the proper electric vector orientation at the TFBG. We let the light from a broadband source pass through a polarization controller (made of a polarizer, half wave plate and a quarter wave

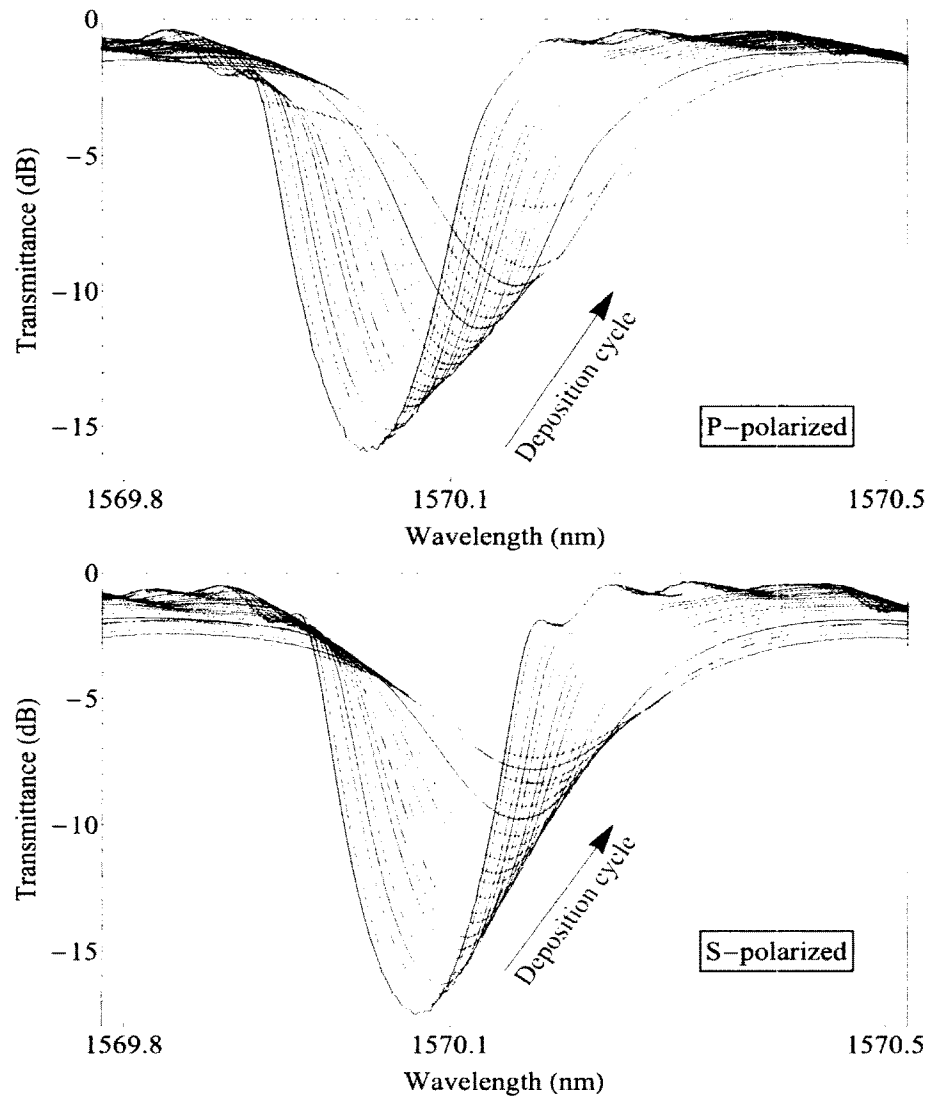


Figure 26: The cladding mode response of a pair of S- and P-resonances during the 23 dipping cycle of the SWCNT deposition on the cladding of the optical fibre (Sample 1).

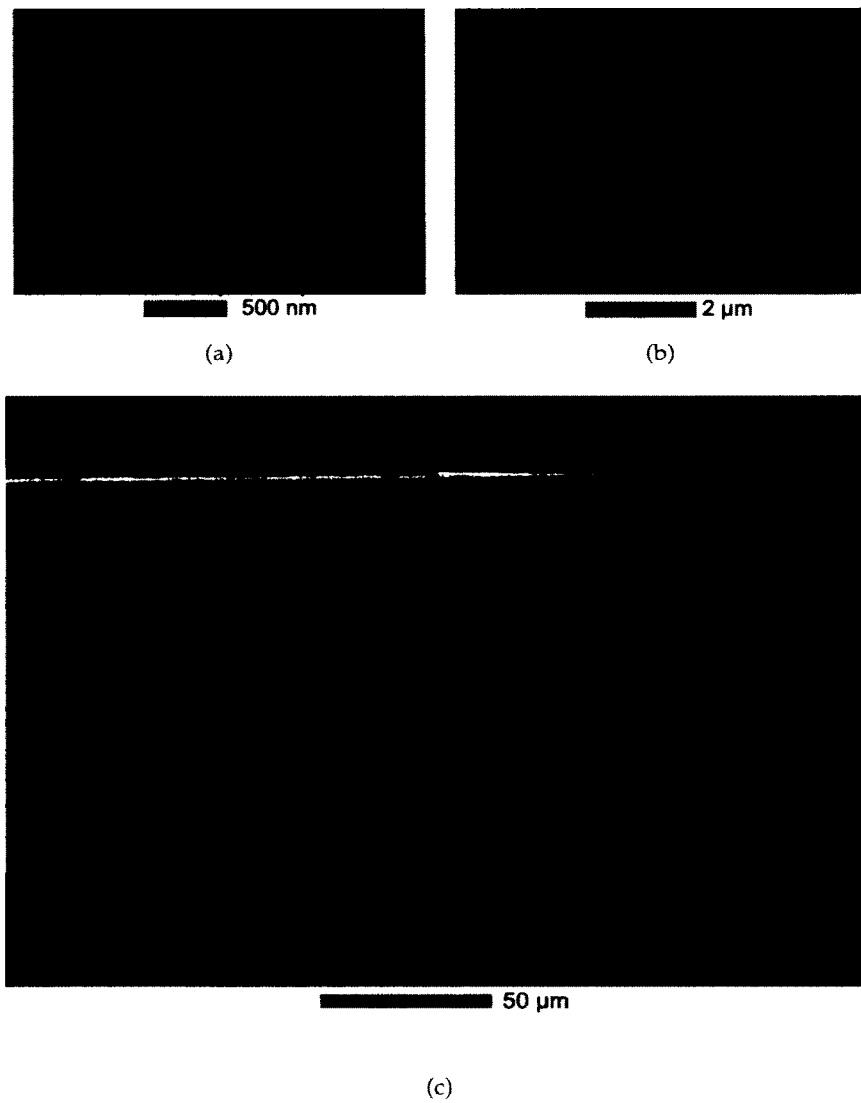


Figure 27: SEM images, in three different scales, confirms the presence of the SWCNT layer on the fibre surface

plate) to obtain polarized light (Figure 25a). Standard telecom fibre is not a polarization maintaining fibre, and hence the polarization vector changes its orientation as the light propagates. Due to bend, stress and other laboratory variables even knowing the exact position of the TFBG and the initial light vector orientation is not good enough to ensure the exact control of the vector. However, one can find the S- and P- resonances by rotating the vector of the core mode and seeking the maximum separation between a pair of resonances 25b). During the dipping cycle we constantly monitor the spectral response of the TFBG using Luna's Optical Vector Analyzer. We record the stable response of the TFBG after each cycle of deposition. Luna measures the complete Jones Matrix (2X2 complex matrix, with the phase and the amplitude, for each wavelength) for the full spectral range of the TFBG's response. The repeated deposition of CNT on the surface of the cladding of the fibre modifies the spectral response of the gratings by changing the wavelength location and the amplitude of each cladding mode resonance. The shift in the resonance location after each dipping cycle readily confirms the growth of the nanotube layer on the surface. Using the Jones matrix data the P- and S-polarized response of the gratings are then calculated using the following axis transformation rule (i.e. a linear polarizer):

$$J_{out} = J \cdot \begin{bmatrix} \cos^2 \theta & \cos \theta \sin \theta \\ \sin \theta \cos \theta & \sin^2 \theta \end{bmatrix} \quad (4.1.1)$$

where J is the Jones matrix, θ is the angle between the arbitrary eigenpolarization directions emitted by the LUNA and the X-axis of the fibre as defined by the direction of the grating tilt. This transmission extracts the X(P-polarized) and Y(S-polarized) transmission spectra. The angle is found by varying the value of θ and looking for the maximum wavelength separation between a pair S and P resonances within a spectral window. Figure 26 shows the recorded change of the cladding mode response of one pair of orthogonally polarized resonances for 23 subsequent dipping cycles for the Sample 1. The SEM images in Figure 27 obtained for the dip coating process show the random orientation of the CNT film growth on the fibre cladding

4.2 ANALYSIS

We are interested in the complete characterization of the SWCNT layers by extracting three parameters: the real and imaginary part of the index and the evolution of the average thickness of the CNT layers. Each dipping cycle changes the wavelength position and the amplitude of the cladding modes. In general, the Kramers-Kronig relationship suggests that the real and the imaginary parts of the index of any material are coupled. However, the dependence is very weak for weak

absorptions. It has been shown in Chapter 2 that since all cladding modes are strongly guided and carry very little power in the evanescent tail, the acquired imaginary part of the effective index is low even for highly absorptive homogeneous outer material. Moreover, in our case, the CNT layers are expected to be very thin and much smaller than the wavelength of light; thus each mode effectively interrogates a composite CNT-air structure. Under these circumstances it is reasonable to expect that the effective imaginary part of the guided modes is weak. For the purpose of this analysis we ignore the effect of the imaginary part while trying to extract the real part of the index and the thickness of the CNT layer. Once we determine these two parameters we proceed to extract the imaginary part of the index of the CNT layer.

The real part of the index is related to the absolute wavelength shift of a resonance. The Bragg mode is guided by the core-cladding boundary and is not perturbed by the outside index change. Moreover, the cladding mode resonances and the Bragg resonance have similar sensitivities to the temperature change and to any undue linear stress. Hence we use the Bragg resonance as internal reference and measure the relative shift of the cladding mode resonances with respect to the Bragg resonance to cancel all undue environmental effects [39]. The Figure 28 also shows the calculated dispersion compensated partial transmission spectrum for the resonances of interest. This response is calculated using the three layer model presented in the previous chapters. Here, we present the analysis of two samples. We prepare sample 1 by 23 dipping cycles and sample 2 by 10 dipping cycles.

From the three layer model we can find the effective guide indexes of the constitutive modes of these two resonances of interest. The choice of these two modes is not completely arbitrary. We have shown in the previous chapter that in the TFBG transmission spectrum even order azimuthal modes and odd order azimuthal modes form alternating resonances. We chose these two pairs since our analysis shows these two pairs are formed by the even order modes include $l = 0$ modes, i.e. TE_{0m} for the S-polarized case and TM_{0m} for the P-polarized case. The unperturbed effective guide indexes are 1.41699 (TM_{0m}), 1.4709 (TE_{0m}) for the Res_1 and 1.40077(TM_{0m}), 1.40094(TE_{0m}) for the Res_2 . Since the analytical expressions are considerably simpler for the transverse modes, our choice simplifies the subsequent calculations.

We calculate the evolution of these resonances using the three layer model presented in the previous chapter. By fitting the experimental data to the three layer structure we find the guide index of the transverse modes. We take material dispersion into account and use the Sellmeier dispersion relation developed by James Fleming in Ref. [80]. A mole fraction of .044% of GeO_2 . gives excellent agreement with

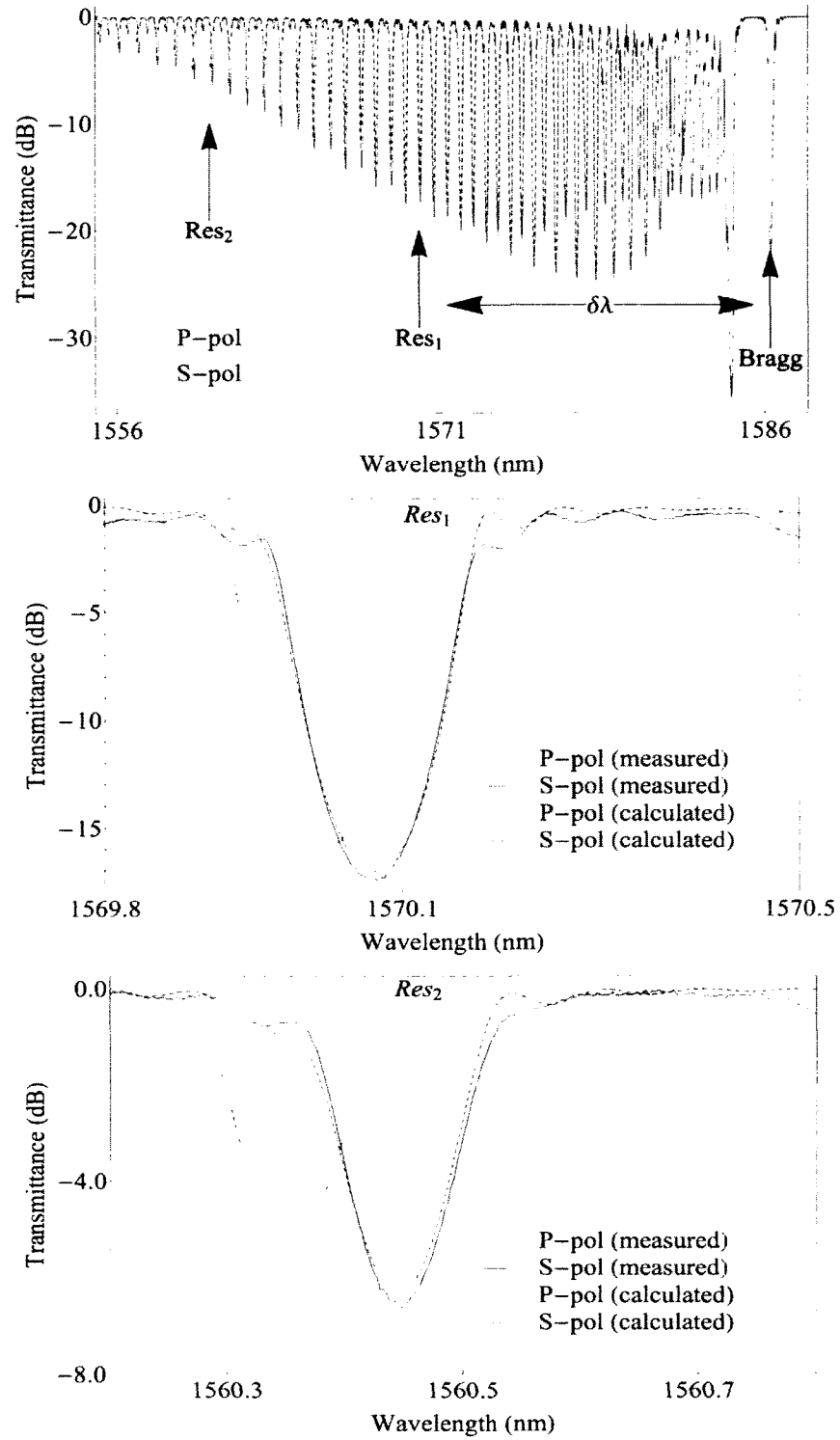


Figure 28: We measure the relative position of the cladding mode resonance ($\delta\lambda$) w.r.t. the Bragg. Res_1 and Res_2 are the two orthogonally polarized pairs of resonances of interest. All three spectra are for fibre with 4° TFBG in air with no CNT.

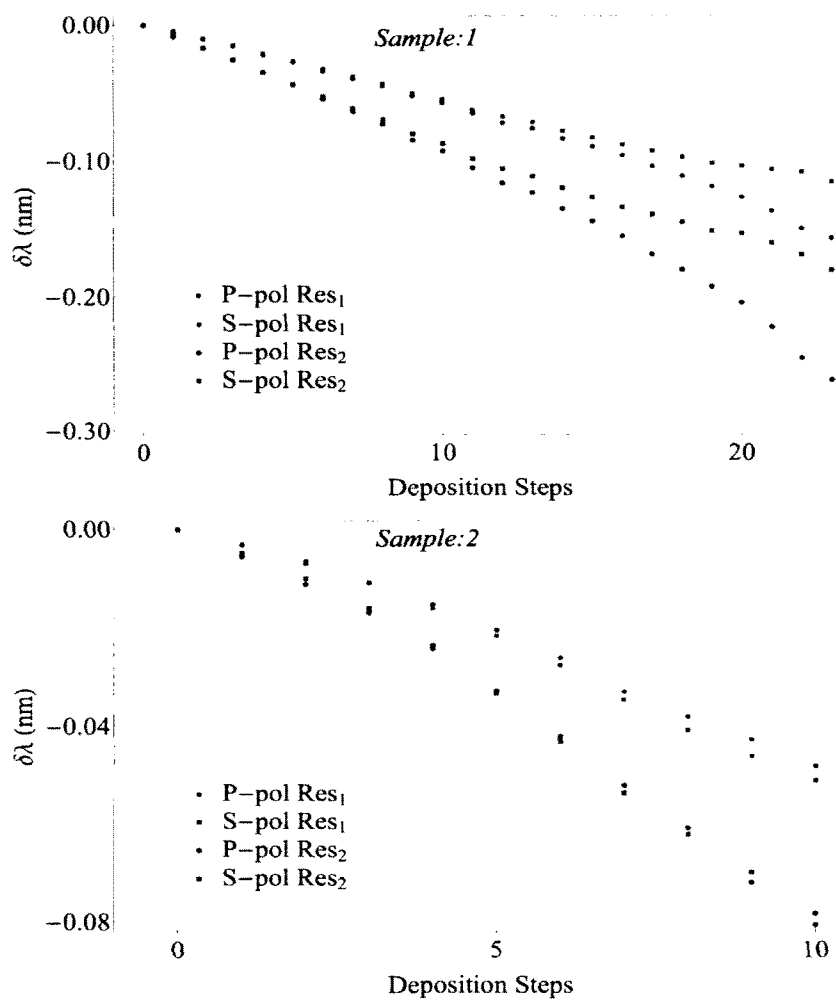


Figure 29: The evolution of the cladding mode resonance wavelength position for Res₁ and Res₂ for the orthogonal polarization. The positions are normalized to the Bragg and to their corresponding initial unperturbed position.

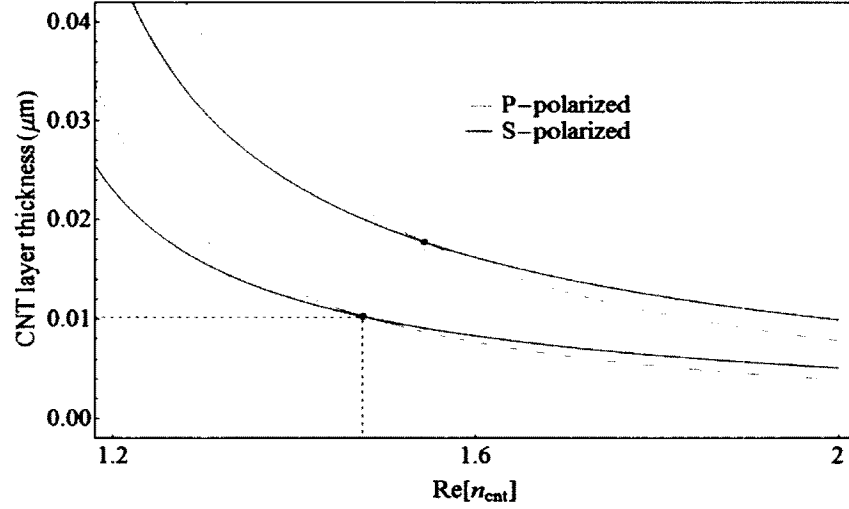
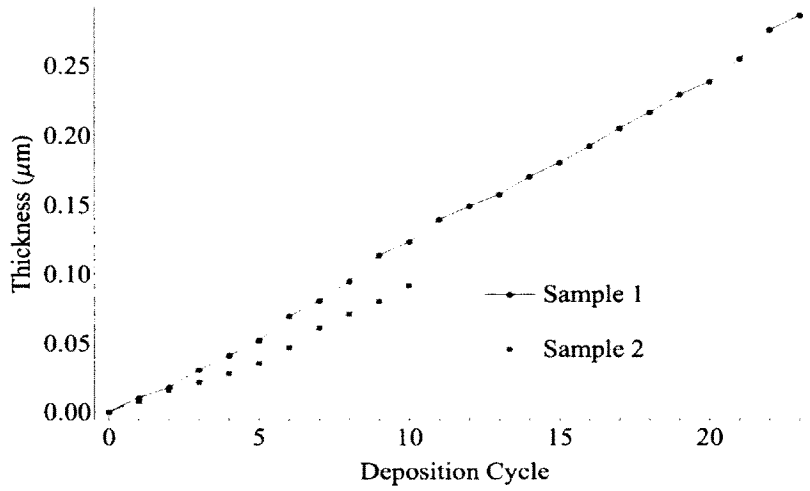
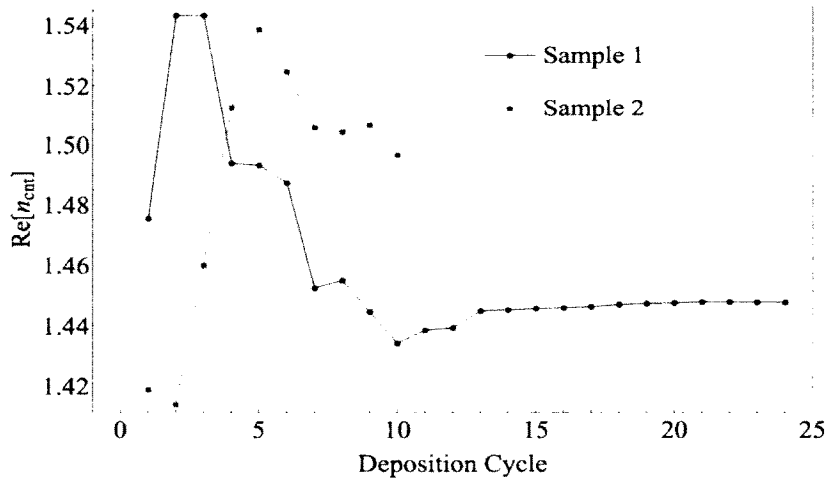


Figure 30: Figure shows the two solution points for the first two dipping cycles of the Sample 2. Each line corresponds to many solutions of the index-thickness pairs that have equal perturbative effect on the P- and S-polarized modes, TE_{0m} and TM_{0m} respectively. The intersection of two lines for each step gives the desired solution.

the experimental response of the TFBG. The other fibre parameters are: for $\lambda = 1586 \text{ nm}$ $n_1 = 1.4502$, $n_2 = 1.44359$, $n_{\text{effcore}} = 1.44683$ and for $\lambda = 1560 \text{ nm}$ $n_1 = 1.45051$, $n_2 = 1.4439$, the core radius $a_1 = 4.1 \mu\text{m}$, and the cladding radius $a_2 = 62.5 \mu\text{m}$. From this three layer model from the Res_1 we can readily find the wavelength location and guide index of each mode. For a non-trivial solution to exist, same mode effective index must also be a solution of the corresponding four layer structure: core, cladding, SWCNT layer, and air. Now for each polarization, using the eigenvalue equation of the four layer structure, and the wavelength and mode guide index obtained from the three layer structure, we seek for a pair of solution containing the thickness and the index of the CNT layer. This gives us a pair of hyperbolas containing all combinations of solution for both P- and S-polarized cases. The intersection of these two parabolas give us the index and thickness value of the CNT layer for which dispersion equation for both polarization satisfy at the wavelength of interest. Figure 30 shows the first two solution points. Figure 31 summarizes the result. At low thickness the index shows anomalous behaviour, however the index quickly goes down and stabilizes (Sample 1). It is important here to note that since our gratings are of 1cm in length and the fact that the TFBG response allows distributed sensing over the length of the gratings, hence the thickness and the index that we extract are average estimates over the length of 1cm. Therefore the values obtained for the small numbers of dipping cycles actually represent an average index for a very sparse distribution of CNTs. Our extracted index val-



(a)



(b)

Figure 31: Index grows linearly as a function of dipping cycle (a). Real part of index shows anomalous behaviour at low thickness, however quickly stabilizes to a bulk index

ues are within the range of the values reported elsewhere in literature. Sylvain et. al. in the ref. [59] very recently (in 2012) reported a value of the real part of the index over 1.4 around 1550nm for randomly oriented CNT deposited on a planar substrate. The index of the CNT layer necessarily depends on the packing density of tubes and the impurity concentration. According to our knowledge the only other reported effort in measuring the index of the SWCNT was done by Arcos et al. as reported in the ref [58]. However they measured the real part of the index of highly aligned SWCNT layer grown on the Si wafer using the chemical vapour deposition technique. They reported an effective index using the Bruggeman approximation for a low density CNT forest on the Si substrate and found the index to be close to 1.1. By controlling the density of vertically aligned Multi-wall Carbon Nanotubes Shi et. al. showed that the real part of the index can be as small as 1.0 [81].

Once the real part and the thickness are extracted we can easily calculate the imaginary part of the index. A number of techniques exist for this purpose. We adopt the group index method as generalized by Qing et al. in ref. [82, 83]. They have shown that the bulk absorption coefficient of a thin layer and the imaginary part of the complex index of the guided mode are related through the following relation

$$\text{Im}[n_{\text{eff}}] = \text{Im}[n_{\text{CNT}}] \frac{n_{g,\text{CNT}}}{n_{\text{CNT}}} F_{\text{CNT}} \quad (4.2.1)$$

where n_g is the group index of the mode in the CNT layer and F_{CNT} is the fraction of the total power, i.e. magnitude of the Poynting vector, in the CNT layer, n_{eff} is the modal effective index and n_{CNT} is the nanotubes index. The group index is the ratio between the speed of light and the group velocity. The group velocity of a mode in a particular layer is the ratio of the modal power to the total stored energy, electric and magnetic, per unit length of the waveguide layer [76]. Fibre is not highly dispersive; moreover, each set of modal resonances are quite narrow and hence we can locally ignore the effect of the dispersion. The group index of the mode in the CNT layer then is [76]

$$n_{g,\text{CNT}} = n_{\text{eff}} \frac{\int_{\text{CNT}} E_{\text{CNT}} \times H_{\text{CNT}}^* \cdot \hat{z} dA}{\int_{\text{CNT}} n_{\text{CNT}}^2 E_{\text{CNT}} \times H_{\text{CNT}}^* \cdot \hat{z} dA} \quad (4.2.2)$$

Now by knowing the $\text{Im}[n_{\text{eff}}]$ of the guided mode of interest we can use equations (4.2.2) and (4.2.1) to readily find the $\text{Im}[n_{\text{CNT}}]$. In chapter 2 we have shown that, away from the cutoff conditions, the loss coefficient of a mode due to lossy outer medium depends primarily on the real part of the modal guide index. Since the constitutive

modes of each resonance are nearly degenerate, the effective modal loss coefficient, i.e. the imaginary part of the guide index can be easily estimated from the transmission depth of the resonances. Although we have shown that the coupling coefficient changes and also resonance amplitude may change purely due to the change in the index of the outer medium, for a 4° grating such changes are minor; and as a first principle approximation we ignore this subtle effect. Hence we are able to readily calculate the effective imaginary part of the modes using the analytical solution of the simple two mode coupling equation. In the presence of loss, the couple mode equation in equation (3.2.1) can be modified with a simple loss term [84, 85]. The value of the minimum linear transmission at the grating assisted phase matching wavelength for 1cm long grating can be expressed as:

$$T = \left| \frac{\sqrt{\alpha^2 + 4\kappa^2} \left(\cosh \frac{\alpha}{2} \right) + \sinh \frac{\alpha}{2}}{\sqrt{\alpha^2 + 4\kappa^2} \cosh 0.5\sqrt{\alpha^2 + 4\kappa^2} + \alpha \sinh 0.5\sqrt{\alpha^2 + 4\kappa^2}} \right|^2 \quad (4.2.3)$$

Since we assume the coupling coefficient κ to be constant, from the grating transmission we can readily calculate the loss coefficient. For this purpose we use the values obtained from Resonance₂ (Figure 28). We present the result of this calculation in Figure 32. Finally we present the thickness vs. the total complex index in Figure 33.

It is not possible to selectively grow one type of nanotube of the same chirality [10]. Hence, our sample is a mixture of semiconducting and metallic nanotube of many kinds and with certain amount of impurities. For any mixture of nanotubes, the effective optical response depends on the distribution of the nanotubes' diameter in the mixture. The mean diameter of our sample is around 1 nm. Due to the extreme structural anisotropy of the CNT (length to diameter ratio) it is expected that nanotubes exhibits high anisotropy [54]. High anisotropy in absorption has been reported by a lot of studies [55, 56, 58, 86]. In 2012 Ren et. al. exploited the high polarization dependent absorption anisotropy of carbon nanotubes by designing a high quality polarizer [87]. However, in all of these cases, the carbon nanotubes were highly aligned. In our sample the carbon nanotubes are randomly oriented and - as one would expect and as is confirmed by our experimental evidence - the nanotube films show no anisotropy in the real part of the index. Hence our result of high polarization dependent absorption anisotropy is very surprising. In fact, Figure 33 shows that at high enough thickness this anisotropy almost disappears. We found no reported case of such behaviour in any existing literature. Moreover, S. Yamashita, a pioneer in the field of carbon nanotube optics, has categorically indicated the non-existence of the absorption anisotropy in a random CNT film in a very recent review paper [10]. This is expected, since high anisotropy in absorption would also mean high anisotropy in propagation. However, the reported thickness of most CNT thin-film optics, random or not, are

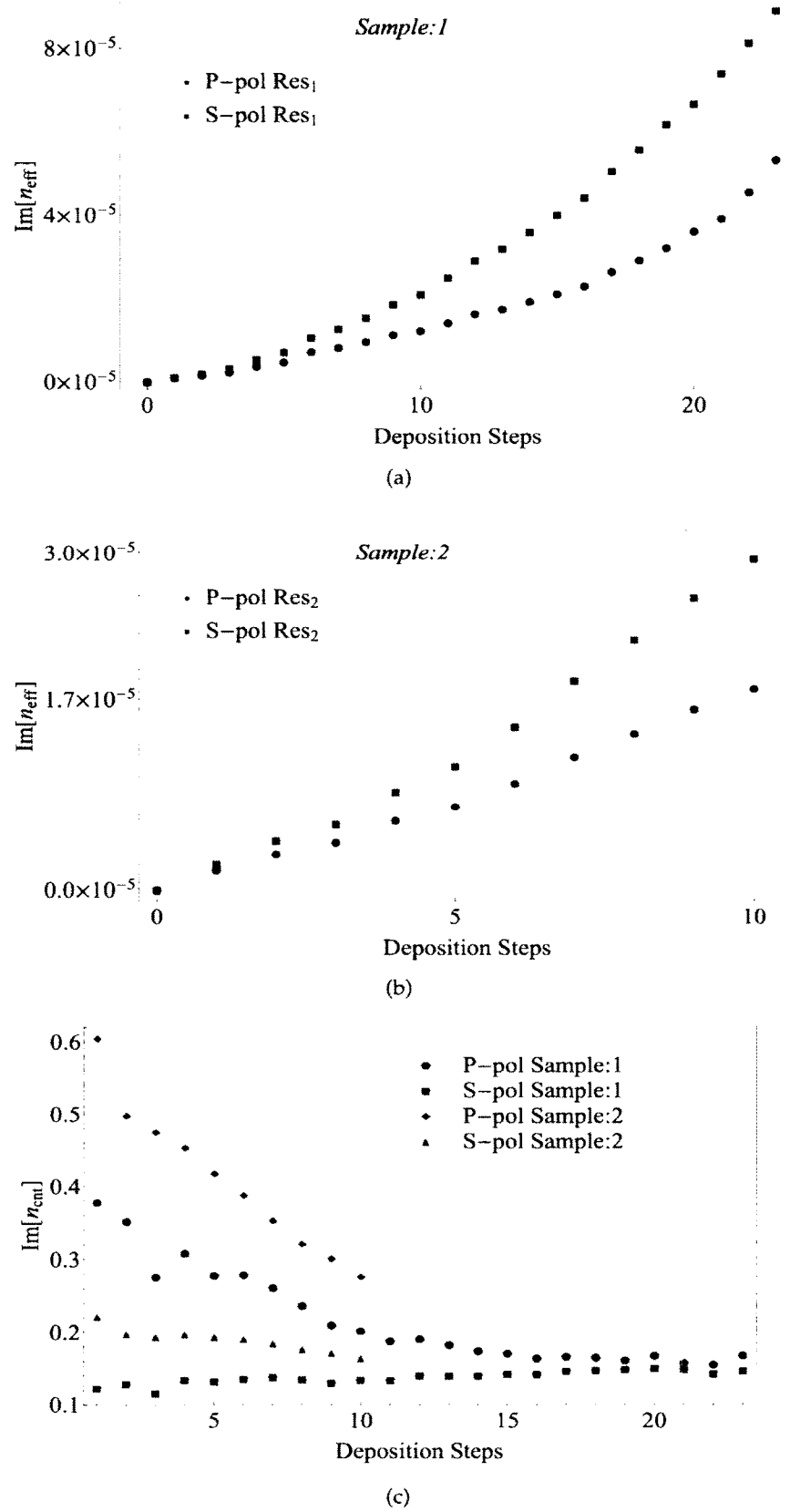
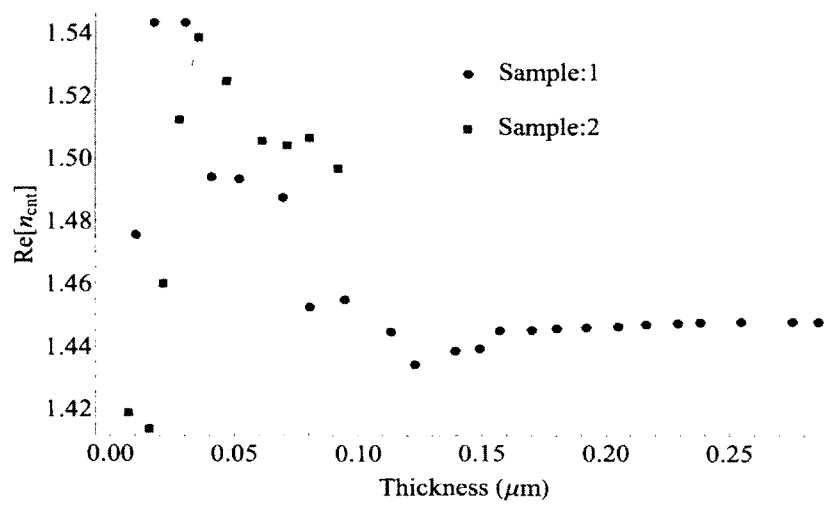
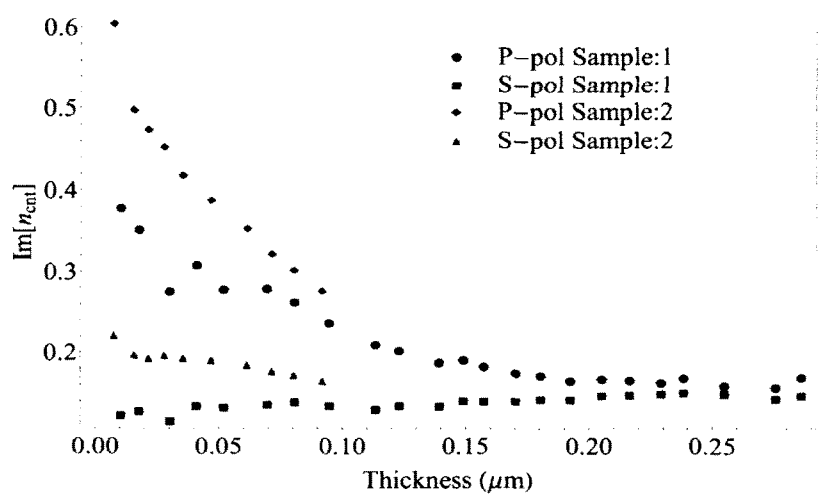


Figure 32: Panel (a) and (b) shows the effective imaginary guide index of two samples under orthogonal Polarization. The CNT layers exhibit strong polarization dependent extinction coefficient with low dipping cycle



(a)



(b)

Figure 33: At low thickness SWCNT layer exhibits anomolous real part and strong polarization dependent absorption

on the order of $1\mu\text{m}$. Our results in high thickness limit ($> 150\text{nm}$), notwithstanding the variation of packing density and chirality, clearly agree with all reported measurements [59].

It is befitting to mention here that, in 2011 Bao et al. reported an in-fibre broadband TE-pass polarizer using a few layers of graphene, the fundamental constitutive structure of nanotube, deposited on the flat side of a D-Shaped fibre [88]. They concluded that the polarization effect is the manifestation of the high polarization dependent attenuation and reported an extinction ratio of 27dB. We also note that the isolated semiconducting carbon nanotube exhibits photo-luminescence, an effect directly related to the absorption response of the CNT, and shows a strong quenching effect for the bundled case due to the rapid charge transfer mechanism between semiconducting and the metallic nanotube [3, 10]. These reported results point to the fact that the optical property of a very thick nanotube film can be different than a thin film of nanometre scale

CONCLUSION

In this thesis we have presented two key results: first, we have theoretically shown that by precisely controlling the linear vector orientation of the core mode with respect to the grating tilt, we can excite one of the two polarization types of cladding modes. P-polarized core mode couples primarily to the odd EH_{lm} and TM_{0m} modes whereas S-polarized core mode couples to the even HE_{lm} and TE_{0m} modes. We have further shown that apart from the few low radial order modes, the rest of the EH_{lm} modes can be approximated as radially polarized and HE_{lm} modes as azimuthally polarized with respect to the cladding boundary. In the transmission spectra this polarization dependent coupling mechanism manifests as spectrally well separated resonances.

Second, we have used the polarization dependent model of TFBG to completely characterize the layer by layer growth of the SWCNT thin film on the cladding of the fibre. Interestingly, we have found that the thin film made of randomly oriented SWCNTs, counter intuitively, exhibit strong polarization dependent loss, although we have not observed any birefringence. We have shown that the thickness grows linearly. The values of the optical constants we have obtained matches very well with all the reported studies apart from one significant deviation and that is the strong polarization dependent loss observed for film thickness less than 50 nm. We have shown that below this thickness radially polarized TM_{0m} and EH_{lm} cladding modes experience loss which is a couple of times higher than the loss experienced by the azimuthally polarized TE_{0m} , and HE_{lm} modes. This is the first ever experimental demonstration of the absorption anisotropy in the randomly oriented SWCNT thin film.

It is important to note that the value of the optical constants obtained are average values over the length of the TFBG. One can readily think of another experiment using a multimode D-shaped fibre or a planar waveguide to further study the polarization dependent absorption property without the presence of the gratings to test the upper limit of the anisotropy. For this purpose we may also need to slow down the growth rate, i.e. thickness in each dipping cycle, of the CNT film. We have noted that the broadband TE pass polarizer using a few layers of graphene reported by Bao et al. [88] is an important work in this respect. We note that the key difference between the graphene and the SWCNT, which exhibits almost all exceptional properties of the monolayer graphene, is primarily due to the addi-

tional quantization arising from the confinement of the electron in the circumference of the nanotubes [10].

We have mentioned that we are interested in exploiting the exceptional optical nonlinear properties of the SWCNT. Members of our group have previously shown that TFBG can be used for the plasmonic excitation on the gold surface [89]. It has recently been reported that the integration of the carbon nanotubes with the plasmonic metamaterials increases the optical nonlinearity by an order of magnitude due to the resonant plasmon-exciton interactions [90]. Researchers have widely reported enhancement of the nonlinear processes in plasmonic composite structure made of metal nanoparticles due to the novel near field focusing mechanisms of these particles [91–94]. Therefore, it could be of high interest to study the behaviour of the metal- nanotube composite structure for nonlinear optical applications.

BIBLIOGRAPHY

- [1] S. Iijima, "Helical microtubules of graphitic carbon," *Nature*, vol. 354, pp. 56–58, 1991.
- [2] S. Iijima and T. Ichihashi, "Single-shell carbo nanotubes of 1-nm diameter," *Nature*, vol. 363, pp. 603–605, 1993.
- [3] P. Avouris, M. Freitag, and V. Perebeinos, "Carbon-nanotube photonics and optoelectronics," *Nature Photonics*, vol. 2, pp. 341–350, June 2008.
- [4] A. Javey, J. Guo, Q. Wang, M. Lundstrom, and H. Dai, "Ballistic carbon nanotube field-effect transistors," *Nature*, vol. 424, pp. 654–7, Aug. 2003.
- [5] R. Chau, S. Datta, M. Doczy, B. Doyle, B. Jin, J. Kavalieros, A. Majumdar, M. Metz, and M. Radosavljevic, "Benchmarking Nanotechnology for Logic Transistor Applications," *IEEE Transactions on Nanotechnology*, vol. 4, no. 2, pp. 153–158, 2005.
- [6] A. D. Franklin and Z. Chen, "Length scaling of carbon nanotube transistors," *Nature Nanotechnology*, vol. 5, pp. 858–62, Dec. 2010.
- [7] A. D. Franklin, M. Luisier, S.-J. Han, G. Tulevski, C. M. Breslin, L. Gignac, M. S. Lundstrom, and W. Haensch, "Sub-10 nm carbon nanotube transistor," *Nano Letters*, vol. 12, pp. 758–62, Feb. 2012.
- [8] F. Wang, G. Dukovic, L. E. Brus, and T. F. Heinz, "The optical resonances in carbon nanotubes arise from excitons," *Science*, vol. 308, pp. 838–41, May 2005.
- [9] D. Y. Joh, J. Kinder, L. H. Herman, S.-Y. Ju, M. a. Segal, J. N. Johnson, G. K.-L. Chan, and J. Park, "Single-walled carbon nanotubes as excitonic optical wires," *Nature Nanotechnology*, vol. 6, pp. 51–6, Jan. 2011.
- [10] S. Yamashita, "A tutorial on nonlinear photonic applications of carbon nanotube and graphene," *Journal of Lightwave Technology*, vol. 30, no. 4, pp. 427–447, 2012.
- [11] R. W. Boyd, *Nonlinear optics*. Academic Press, 2003.
- [12] Y. Sakakibara, A. G. Rozhin, H. Kataura, Y. Achiba, and M. Tokumoto, "Carbon nanotube-poly(vinylalcohol) nanocomposite film devices: applications for femtosecond fiber laser mode lockers and optical amplifier noise suppressors," *Japanese Journal of Applied Physics*, vol. 44, pp. 1621–1625, Apr. 2005.

- [13] S. Set, H. Yaguchi, Y. Tanaka, and M. Jablonski, "Laser mode locking using a saturable absorber incorporating carbon nanotubes," *Journal of Lightwave Technology*, vol. 22, pp. 51–56, Jan. 2004.
- [14] S. Set, H. Yaguchi, Y. Tanaka, and M. Jablonski, "Ultrafast fiber pulsed lasers incorporating carbon nanotubes," *IEEE Journal of Selected Topics in Quantum Electronics*, vol. 10, pp. 137–146, Jan. 2004.
- [15] T. Schibli, K. Minoshima, H. Kataura, E. Itoga, N. Minami, S. Kazaoui, K. Miyashita, M. Tokumoto, and Y. Sakakibara, "Ultrashort pulse-generation by saturable absorber mirrors based on polymer-embedded carbon nanotubes," *Optics Express*, vol. 13, pp. 8025–31, Oct. 2005.
- [16] F. Wang, a. G. Rozhin, V. Scardaci, Z. Sun, F. Hennrich, I. H. White, W. I. Milne, and a. C. Ferrari, "Wideband-tuneable, nanotube mode-locked, fibre laser," *Nature Nanotechnology*, vol. 3, pp. 738–42, Dec. 2008.
- [17] Z. Sun, T. Hasan, F. Wang, A. G. Rozhin, I. H. White, and A. C. Ferrari, "Ultrafast stretched-pulse fiber laser mode-locked by carbon nanotubes," *Nano Research*, vol. 3, pp. 404–411, May 2010.
- [18] A. Martinez and S. Yamashita, "Multi-gigahertz repetition rate passively modelocked fiber lasers using carbon nanotubes," *Optics Express*, vol. 19, no. 7, pp. 21350–21355, 2011.
- [19] D.-P. Zhou, L. Wei, B. Dong, and W.-K. Liu, "Tunable passively Q-switched erbium-doped fiber laser with carbon nanotubes as a saturable absorber," *IEEE Photonics Technology Letters*, vol. 22, no. 1, pp. 9–11, 2010.
- [20] K. K. Chow, M. Tsuji, and S. Yamashita, "Single-walled carbon-nanotube-deposited tapered fiber for four-wave mixing based wavelength conversion," *Applied Physics Letters*, vol. 96, no. 6, p. 061104, 2010.
- [21] Y.-Z. Ma, J. Stenger, J. Zimmermann, S. M. Bachilo, R. E. Smalley, R. B. Weisman, and G. R. Fleming, "Ultrafast carrier dynamics in single-walled carbon nanotubes probed by femtosecond spectroscopy," *The Journal of chemical physics*, vol. 120, pp. 3368–73, Feb. 2004.
- [22] K. K. Chow, S. Yamashita, and Y. W. Song, "A widely tunable wavelength converter based on nonlinear polarization rotation in a carbon-nanotube-deposited D-shaped fiber," *Optics Express*, vol. 17, pp. 7664–9, Apr. 2009.

- [23] Y. Song, S. Set, and S. Yamashita, "Novel Kerr shutter using carbon nanotubes deposited onto a 5-cm D-shaped fiber," in *Conference on Lasers and Electro-Optics*, vol. 1, pp. 5–6, Optical Society of America, 2006.
- [24] S. Y. Ryu, K.-S. Kim, J. Kim, and S. Kim, "Degradation of optical properties of a film-type single-wall carbon nanotubes saturable absorber (SWNT-SA) with an Er-doped all-fiber laser," *Optics Express*, vol. 20, pp. 12966–74, June 2012.
- [25] G. Villanueva, M. Jakubinek, B. Simard, C. Oton, J. Matres, L. Shao, P. Pérez Millán, and J. Albert, "Linear and nonlinear optical properties of carbon nanotube-coated single-mode optical fiber gratings," *Optics Letters*, vol. 36, no. 11, pp. 2104–2106, 2011.
- [26] L.-Y. Shao, M. B. Jakubinek, T. Sun, B. Simard, and J. Albert, "Four-wave mixing in carbon nanotube-coated optical fiber gratings," *Applied Physics Letters*, vol. 100, no. 7, p. 071108, 2012.
- [27] K. Hill and G. Meltz, "Fiber Bragg grating technology fundamentals and overview," *Journal of Lightwave Technology*, vol. 15, no. 8, pp. 1263–1276, 1997.
- [28] K. O. Hill, B. Malo, F. Bilodeau, D. C. Johnson, and J. Albert, "Bragg gratings fabricated in monomode photosensitive optical fiber by UV exposure through a phase mask," *Applied Physics Letters*, vol. 62, no. 10, p. 1035, 1993.
- [29] K. O. Hill, Y. Fujii, D. C. Johnson, and B. S. Kawasaki, "Photosensitivity in optical fiber waveguides: Application to reflection filter fabrication," *Applied Physics Letters*, vol. 32, no. 10, p. 647, 1978.
- [30] G. Meltz, W. W. Morey, and W. H. Glenn, "Formation of Bragg gratings in optical fibers by a transverse holographic method," *Optics Letters*, vol. 14, pp. 823–5, Aug. 1989.
- [31] T. Erdogan and J. E. Sipe, "Tilted fiber phase gratings," *Journal of the Optical Society of America A*, vol. 13, p. 296, Feb. 1996.
- [32] R. Kashyap, R. Wyatt, and R. J. Campbell, "Wideband gain flattened erbium fibre amplifier using a photosensitive fibre blazed grating," *Electronics Letters*, vol. 29, no. 2, pp. 154–156, 1993.
- [33] I. Riant, L. Gasca, P. Sansonetti, G. Bourret, and J. Chesnoy, "Gain equalization with optimized slanted Bragg grating on adapted fibre for multichannel long-haul submarine transmission," in *Optical Fiber Communication Conference, 1999, and the International Conference on Integrated Optics and Optical Fiber Communication. OFC/IOOC '99. Technical Digest*, vol. 3, pp. 147–149, 1999.

- [34] K. Zhou, X. Chen, and L. Zhang, "High extinction ratio in-fiber polarizer based on a 45°-tilted fiber Bragg grating," *Optics Letters*, vol. 30, no. 11, pp. 1285–1287, 2005.
- [35] K. S. Lee and T. Erdogan, "Fiber mode conversion with tilted gratings in an optical fiber," *Journal of the Optical Society of America. A*, vol. 18, pp. 1176–85, May 2001.
- [36] K. Feder, P. Westbrook, J. Ging, P. Reyes, and G. Carver, "In-fiber spectrometer using tilted fiber gratings," *IEEE Photonics Technology Letters*, vol. 15, pp. 933–935, July 2003.
- [37] G. Laffont and P. Ferdinand, "Tilted short-period fibre-Bragg-grating-induced coupling to cladding modes for accurate refractometry," *Measurement Science and Technology*, vol. 12, pp. 765–770, 2001.
- [38] X. Chen, K. Zhou, L. Zhang, and I. Bennion, "Optical chemsensor based on etched tilted Bragg grating structures in multimode fiber," *IEEE Photonics Technology Letters*, vol. 17, no. 4, pp. 864–866, 2005.
- [39] C.-F. Chan, C. Chen, A. Jafari, A. Laronche, D. J. Thomson, and J. Albert, "Optical fiber refractometer using narrow-band cladding-mode resonance shifts," *Applied Optics*, vol. 46, pp. 1142–9, Mar. 2007.
- [40] L.-Y. Shao, A. Laronche, M. Smietana, P. Mikulic, W. J. Bock, and J. Albert, "Highly sensitive bend sensor with hybrid long-period and tilted fiber Bragg grating," *Optics Communications*, vol. 283, pp. 2690–2694, July 2010.
- [41] L.-Y. Shao and J. Albert, "Compact fiber-optic vector inclinometer," *Optics Letters*, vol. 35, pp. 1034–6, Apr. 2010.
- [42] T. Guo, L. Shao, H.-Y. Tam, P. A. Krug, and J. Albert, "Tilted fiber grating accelerometer incorporating an abrupt biconical taper for cladding to core recoupling," *Optics Express*, vol. 17, pp. 20651–60, Nov. 2009.
- [43] T. Allsop, M. Dubov, and A. Martinez, "Long period grating directional bend sensor based on asymmetric index modification of cladding," *Electronics Letters*, vol. 41, no. 2, pp. 5–6, 2005.
- [44] T. Allsop, R. Neal, S. Rehman, D. Webb, D. Mapps, and I. Bennion, "Generation of infrared surface plasmon resonances with high refractive index sensitivity utilizing tilted fiber Bragg gratings," *Applied Optics*, vol. 46, no. 22, pp. 5456–5460, 2007.
- [45] Y. Shevchenko, C. Chen, M. Dakka, and J. Albert, "Polarization-selective grating excitation of plasmons in cylindrical optical fibers," *Optics Letters*, vol. 35, pp. 637–9, Mar. 2010.

- [46] A. Bialaiyeu, C. Caucheteur, N. Ahamad, A. Ianoul, and J. Albert, "Self-optimized metal coatings for fiber plasmonics by electroless deposition.," *Optics Express*, vol. 19, pp. 18742–53, Sept. 2011.
- [47] Y. Li, M. Froggatt, and T. Erdogan, "Volume current method for analysis of tilted fiber gratings," *IEEE Journal of Lightwave Technology*, vol. 19, no. 10, pp. 1580–1591, 2001.
- [48] Y. Li and T. G. Brown, "Radiation modes and tilted fiber gratings," *Journal of the Optical Society of America B*, vol. 23, no. 8, p. 1544, 2006.
- [49] L. Dong, B. Ortega, and L. Reekie, "Coupling characteristics of cladding modes in tilted optical fiber bragg gratings.," *Applied Optics*, vol. 37, pp. 5099–105, Aug. 1998.
- [50] K. S. Lee and T. Erdogan, "Fiber mode coupling in transmissive and reflective tilted fiber gratings.," *Applied Optics*, vol. 39, pp. 1394–404, Mar. 2000.
- [51] Y.-C. Lu, W.-P. Huang, and S.-S. Jian, "Full vector complex coupled mode theory for tilted fiber gratings.," *Optics Express*, vol. 18, pp. 713–26, Jan. 2010.
- [52] H. Su, J. Ye, Z. Tang, and K. Wong, "Resonant second-harmonic generation in monosized and aligned single-walled carbon nanotubes," *Physical Review B*, vol. 77, pp. 1–4, Mar. 2008.
- [53] H. Kim, T. Sheps, P. G. Collins, and E. O. Potma, "Nonlinear optical imaging of individual carbon nanotubes with four-wave-mixing microscopy.," *Nano Letters*, vol. 9, pp. 2991–5, Aug. 2009.
- [54] F. García Vidal, J. Pitarke, and J. Pendry, "Effective medium theory of the optical properties of aligned carbon nanotubes," *Physical Review Letters*, vol. 78, pp. 4289–4292, June 1997.
- [55] Y. Murakami, "Growth of vertically aligned single-walled carbon nanotube films on quartz substrates and their optical anisotropy," *Chemical Physics Letters*, vol. 385, pp. 298–303, Feb. 2004.
- [56] Y. Murakami, E. Einarsson, T. Edamura, and S. Maruyama, "Polarization dependence of the optical absorption of single-walled carbon nanotubes," *Physical Review Letters*, vol. 94, pp. 1–4, Mar. 2005.
- [57] X. J. Wang, J. D. Flicker, B. J. Lee, W. J. Ready, and Z. M. Zhang, "Visible and near-infrared radiative properties of vertically aligned multi-walled carbon nanotubes.," *Nanotechnology*, vol. 20, p. 215704, May 2009.

- [58] T. D. L. Arcos, P. Oelhafen, and D. Mathys, "Optical characterization of alignment and effective refractive index in carbon nanotube films," *Nanotechnology*, vol. 18, p. 265706, July 2007.
- [59] S. Maine, C. Koechlin, S. Rennesson, J. Jaeck, S. Salort, B. Chasagne, F. Pardo, J.-L. Pelouard, and R. Häidar, "Complex optical index of single wall carbon nanotube films from the near-infrared to the terahertz spectral range.," *Applied Optics*, vol. 51, pp. 3031–5, May 2012.
- [60] C. Tsao, *Optical Fibre Waveguide Analysis*. Oxford University Press, 1991.
- [61] A. P. Belanov, E. Dianov, G. Ezhov, "Propagation of normal modes in multilayer optical waveguides. II. Energy characteristics," *Soviet Journal of Quantum Electronics*, vol. 6, no. 8, pp. 915–920, 1976.
- [62] A. P. Belanov, E. Dianov, G. Ezhov, "Propagation of normal modes in multilayer optical waveguides I. Component fields and dispersion characteristics," *Soviet Journal of Quantum Electronics*, vol. 6, no. 1, pp. 43–50, 1976.
- [63] C. Yeh and G. Lindgren, "Computing the propagation characteristics of radially stratified fibers: an efficient method," *Applied Optics*, vol. 16, no. 2, pp. 483–493, 1977.
- [64] C. Tsao, D. Payne, and W. Gambling, "Modal characteristics of three-layered optical fiber waveguides: a modified approach," *Journal of the Optical Society of America A*, vol. 6, no. 4, pp. 555–563, 1989.
- [65] T. Erdogan, "Cladding-mode resonances in short- and long-period fiber grating filters," *Journal of the Optical Society of America A*, vol. 14, p. 1760, Aug. 1997.
- [66] D. Gloge, "Weakly guiding fibers.," *Applied Optics*, vol. 10, pp. 2252–8, Oct. 1971.
- [67] D. Marcuse, *Theory Of Dielectric Optical Waveguides*. Academic Press, 1974.
- [68] E. Snitzer, "Cylindrical dielectric waveguide modes," *Journal of the Optical Society of America*, vol. 51, no. 5, pp. 491–498, 1961.
- [69] D. Calvetti, G. H. Golub, W. B. Gragg, and L. Reichel, "Computation of Gauss-Kronrod quadrature rules," *Mathematics of Computation*, vol. 69, pp. 1035–1053, Feb. 2000.
- [70] A. Safaai Jazi and G. L. Yip, "Classification of hybrid modes in cylindrical dielectric optical waveguides," *Radio Science*, vol. 12, no. 4, pp. 603–609, 1977.

- [71] K. Morishita, "Hybrid modes in circular cylindrical optical fibers," *IEEE Transactions on Microwave Theory and Techniques*, vol. 31, no. 4, pp. 344–350, 1983.
- [72] C. Yeh, "Guided-wave modes in cylindrical optical fibers," *Education, IEEE Transactions on*, vol. E-30, no. 1, pp. 43–51, 1987.
- [73] A. Kapoor and G. Singh, "Mode classification in cylindrical dielectric waveguides," *Journal of Lightwave Technology*, vol. 18, no. 5, p. 849, 2000.
- [74] V. Lucarini, J. Saarinen, K.-E. Peiponen, and E. Vartiainen, *Kramers-kronig relations in optical materials research*, vol. 110. Springer Verlag, 2005.
- [75] H. Gnewuch and H. Renner, "Mode-independent attenuation in evanescent-field sensors.," *Applied Optics*, vol. 34, pp. 1473–83, Mar. 1995.
- [76] A. Snyder and J. Love, *Optical Waveguide Theory*. Springer, 1983.
- [77] P. Taylor and M. Hashimoto, "Propagation of inhomogeneous waves in cladde optical fibres," *International Journal of Electronics Theoretical and Experimental*, vol. 46, no. 2, pp. 125–139, 1979.
- [78] T. Erdogan, "Cladding-mode resonances in short-and long-period fiber grating filters: errata," *J. Opt. Soc. Am. A*, vol. 14627, no. 1997, p. 112113, 2000.
- [79] M. B. Jakubinek, M. B. Johnson, M. A. White, J. Guan, and B. Simard, "Novel method to produce single-walled carbon nanotube films and their thermal and electrical properties," *Journal of Nanoscience and Nanotechnology*, vol. 10, pp. 8151–8157, Dec. 2010.
- [80] J. W. Fleming, "Dispersion in GeO_2 - SiO_2 glasses," *Applied Optics*, vol. 23, no. 24, pp. 4486–4493, 1984.
- [81] H. Shi, J. G. Ok, H. Won Baac, and L. Jay Guo, "Low density carbon nanotube forest as an index-matched and near perfect absorption coating," *Applied Physics Letters*, vol. 99, no. 21, p. 211103, 2011.
- [82] D.-K. Qing, X.-M. Chen, K. Itoh, and M. Murabayashi, "A theoretical evaluation of the absorption coefficient of the optical waveguide group index method," *Journal of Lightwave Technology*, vol. 14, no. 8, pp. 1907–1917, 1996.
- [83] D.-K. Qing and I. Yamaguchi, "Analysis of the sensitivity of optical waveguide chemical sensors for TM modes by the group-index method," *Journal of the Optical Society of America B*, vol. 16, p. 1359, Sept. 1999.

- [84] A. Hardy and W. Streifer, "Coupled mode theory of parallel waveguides," *Lightwave Technology, Journal of*, vol. LT-3, no. 5, pp. 1135–1146, 1985.
- [85] E. Kapon, A. Hardy, and A. Katzir, "The effect of complex coupling coefficients on distributed feedback lasers," *Quantum Electronics, IEEE Journal of*, vol. 18, no. 1, pp. 66–71, 1982.
- [86] M. Islam, D. Milkie, C. Kane, A. Yodh, and J. Kikkawa, "Direct Measurement of the Polarized Optical Absorption Cross Section of Single-Wall Carbon Nanotubes," *Physical Review Letters*, vol. 93, pp. 3–6, July 2004.
- [87] L. Ren, C. L. Pint, T. Arikawa, K. Takeya, I. Kawayama, M. Tonouchi, R. H. Hauge, and J. Kono, "Broadband terahertz polarizers with ideal performance based on aligned carbon nanotube stacks," *Nano Letters*, vol. 12, pp. 787–90, Feb. 2012.
- [88] Q. Bao, H. Zhang, B. Wang, Z. Ni, and C. Lim, "Broadband graphene polarizer," *Nature Photonics*, vol. 5, no. 7, pp. 411–415, 2011.
- [89] Y. Y. Shevchenko and J. Albert, "Plasmon resonances in gold-coated tilted fiber Bragg gratings," *Optics Letters*, vol. 32, pp. 211–3, Feb. 2007.
- [90] A. E. Nikolaenko, F. De Angelis, S. A. Boden, N. Papasimakis, P. Ashburn, E. Di Fabrizio, and N. I. Zheludev, "Carbon nanotubes in a photonic metamaterial," *Physical Review Letters*, vol. 104, pp. 3–6, Apr. 2010.
- [91] M. Danckwerts and L. Novotny, "Optical frequency mixing at coupled gold nanoparticles," *Physical Review Letters*, vol. 98, pp. 1–4, Jan. 2007.
- [92] S. Palomba, M. Danckwerts, and L. Novotny, "Nonlinear plasmonics with gold nanoparticle antennas," *Journal of Optics A: Pure and Applied Optics*, vol. 11, p. 114030, Nov. 2009.
- [93] K. Wang, H. Long, M. Fu, G. Yang, and P. Lu, "Size-related third-order optical nonlinearities of Au nanoparticle arrays," *Optics Express*, vol. 18, pp. 13874–9, June 2010.
- [94] Y. Luo, D. Lei, S. Maier, and J. Pendry, "Broadband light harvesting nanostructures robust to edge bluntness," *Physical Review Letters*, vol. 108, pp. 1–5, Jan. 2012.

A

APPENDIX

This appendix contains some of the Mathematica© codes I have developed for calculating the results included in this thesis. Codes begin in the next page.

```

(*Dispersion value Calculation*)
SA1 = 0.69616630;
S11 = 0.068404300;
SA2 = 0.40794260;
S12 = 0.11624140;
SA3 = 0.89747940;
S13 = 0.98961610 * 10;
GA1 = 0.80686642;
G11 = 0.068972606;
GA2 = 0.71815848;
G12 = 0.15396605;
GA3 = 0.85416831;
G13 = 0.11841931 * 100;
X = 0.044; (*mole Fraction of Ge*)

nclad[λ_] :=  $\sqrt{\left(1 + \frac{SA1 \lambda^2}{\lambda^2 - S11^2} + \frac{SA2 \lambda^2}{\lambda^2 - S12^2} + \frac{SA3 \lambda^2}{\lambda^2 - S13^2}\right)}$ ;

(*gives clad index at λ in μm*)
ncore[λ_] :=  $\sqrt{\left(1 + \frac{(SA1 + X (GA1 - SA1)) \lambda^2}{\lambda^2 - (S11 + X (G11 - S11))^2} + \frac{(SA2 + X (GA2 - SA2)) \lambda^2}{\lambda^2 - (S12 + X (G12 - S12))^2} + \frac{(SA3 + X (GA3 - SA3)) \lambda^2}{\lambda^2 - (S13 + X (G13 - S13))^2}\right)}$ ; (*gives core index at λ in μm*)

(*Returns Core mode index at λ*)
coreModeIndex[λ_] :=
Block[{coreindexFunction, l, Z0, a1, a2, n1, n2, u0, v, b, pHE, seeds},
  a1 = 4.1; a2 = 62.5; (*use SMF 28 value*)
  Z0 = 377.0;
  l = 1.0; (*azimuthal mode index*)
  n1 = ncore[λ]; n2 = nclad[λ];
  (*Calculate core mode effective index*)
  u0[neffcore_Real] :=  $\sqrt{((2 \pi) / \lambda)^2 (n1^2 - neffcore^2)}$ ;
  v =  $((2 \pi) / \lambda) a1 \sqrt{(n1^2 - n2^2)}$ ;
  b[neffcore_Real] :=  $(neffcore^2 - n2^2) / (n1^2 - n2^2)$ ;
  coreindexFunction[x_] := Evaluate $\left[v \sqrt{(1 - b[x])} \frac{BesselJ[1, v \sqrt{(1 - b[x])}]}{BesselJ[0, v \sqrt{(1 - b[x])}]}$ 
    - v  $(\sqrt{b[x]}) \frac{BesselK[1, v \sqrt{b[x]}}{BesselK[0, v \sqrt{b[x]}]}\right]$ ;
  pHE = Plot[Re[coreindexFunction[x]], {x, n2, n1},
    Mesh → {{0}}, MeshFunctions → {coreindexFunction[#] &}];
  seeds = Cases[Normal[pHE], Point[z_] → z[[1], ∞];
  Return[Flatten[Table[x /. FindRoot[coreindexFunction[x],
    {x, s}], {s, seeds}]] ∪ (SameTest → (Re[#1 - #2] < 10-6 &))]]];

```

```

(*Solving the Cladding mode dispersion relation*)
(*findModeSolutionEH[nefflow, neffhigh, wavelength, lorder, nout]
  returns all EH (and TM) modes for which nefflow ≤ neff ≤ neffhigh*)
(*findModeSolutionHE[nefflow, neffhigh, wavelength, lorder, nout]
  returns all HE (and TE) modes for which nefflow ≤ neff ≤ neffhigh*)


$$\xi_0 = \frac{p_1 u_2 \left( J K + \frac{u_{21} u_{32} \sigma_1 \sigma_2}{a_1 a_2 n_2^2} \right) + q_1 (-K) + J r_1 - \frac{s_1}{u_2}}{\sigma_2 \left( p_1 (-u_2) \left( \frac{J u_{32}}{a_2 n_2^2} - \frac{u_{21} K}{a_1 n_1^2} \right) + \frac{r_1 u_{21}}{a_1 n_1^2} + \frac{q_1 u_{32}}{a_2 n_1^2} \right)}$$



$$\xi_{0prime} = \frac{\sigma_1 \left( p_1 u_2 \left( \frac{J u_{32}}{a_2} - \frac{(n_3^2 u_{21}) K}{a_1 n_2^2} \right) - \frac{r_1 u_{21}}{a_1} - \frac{q_1 u_{32}}{a_2} \right)}{p_1 u_2 \left( \frac{n_3^2 J K}{n_2^2} + \frac{u_{21} u_{32} \sigma_1 \sigma_2}{a_1 a_2 n_1^2} \right) - \frac{n_3^2 q_1 K}{n_1^2} + J r_1 - \frac{n_2^2 s_1}{n_1^2 u_2}}$$


f =  $\xi_0 - \xi_{0prime}$ ;
sol = K /. Simplify[Solve[f == 0, K]];


$$u_1 = \sqrt{\left( \frac{2\pi}{\lambda} \right)^2 (n_1^2 - x^2)};$$



$$u_2 = \sqrt{\left( \frac{2\pi}{\lambda} \right)^2 (n_2^2 - x^2)};$$



$$w_3 = \sqrt{\left( \frac{2\pi}{\lambda} \right)^2 (x^2 - n_3^2)};$$



$$u_{21} = \left( \frac{1}{u_2^2} - \frac{1}{u_1^2} \right);$$



$$u_{32} = \left( \frac{1}{u_2^2} + \frac{1}{w_3^2} \right);$$


DBesselJ[1_, arg_] = 1/2 (BesselJ[-1+1, arg] - BesselJ[1+1, arg]);
DBesselK[1_, arg_] = 1/2 (-BesselK[-1+1, arg] - BesselK[1+1, arg]);
DBesselY[1_, arg_] = 1/2 (BesselY[-1+1, arg] - BesselY[1+1, arg]);


$$J = \frac{DBesselJ[1, a_1 u_1]}{u_1 BesselJ[1, u_1 a_1]};$$


p1 = BesselY[1, u_2 a_1] BesselJ[1, u_2 a_2] - BesselJ[1, u_2 a_1] BesselY[1, u_2 a_2];
q1 = BesselJ[1, u_2 a_2] DBesselY[1, a_1 u_2] - BesselY[1, u_2 a_2] DBesselJ[1, a_1 u_2];
r1 = BesselY[1, u_2 a_1] DBesselJ[1, a_2 u_2] - BesselJ[1, u_2 a_1] DBesselY[1, a_2 u_2];
s1 = DBesselY[1, a_1 u_2] DBesselJ[1, a_2 u_2] - DBesselJ[1, a_1 u_2] DBesselY[1, a_2 u_2];


$$\sigma_1 = \frac{i l x}{Z_0};$$



$$\sigma_2 = i l x Z_0;$$


fEH = sol[[1]] -  $\frac{DBesselK[1, a_2 w_3]}{w_3 BesselK[1, w_3 a_2]};$ 

```

```

fHE = sol[[2]] -  $\frac{DBesselK[1, a2 w3]}{w3 BesselK[1, w3 a2]}$ ;

(*convert the solutions into function*)
modeEH[neff_] := fEH /. x -> neff;
modeHE[neff_] := fHE /. x -> neff;

(*Declare compiled function*)
HEmodes = Compile[{{x, _Real}}, Evaluate[modeHE[x]],
  (*{{x, _Real}}, *) RuntimeAttributes -> {Listable}, Parallelization -> True,
  CompilationTarget -> "C", "RuntimeOptions" -> "Speed",
  CompilationOptions -> {"ExpressionOptimization" -> True},
  RuntimeOptions -> {"EvaluateSymbolically" -> False}];

(*HEmodes[x_] := Evaluate[modeHE[x]];
EHmodes[x_] := Evaluate[modeEH[x]];*)

EHmodes = Compile[{{x, _Real}}, Evaluate[modeEH[x]],
  (*{{x, _Real}}, *) RuntimeAttributes -> {Listable}, Parallelization -> True,
  CompilationTarget -> "C", "RuntimeOptions" -> "Speed",
  CompilationOptions -> {"ExpressionOptimization" -> True},
  RuntimeOptions -> {"EvaluateSymbolically" -> False}];
modePlotsHE[nefflow_, neffhigh_] :=
  Block[{},
    (*Declare the functions that plots
    the mode within a specific range of effective index*)
    pHE = Plot[Re[Evaluate[HEmodes[x]]], {x, nefflow, neffhigh},
      Mesh -> {{0}}, MeshFunctions -> {HEmodes[#] &}];];
modePlotsEH[nefflow_, neffhigh_] :=
  Block[{},
    (*Declare the functions that plots
    the mode within a specific range of effective index*)
    pEH = Plot[Re[Evaluate[EHmodes[x]]], {x, nefflow, neffhigh},
      Mesh -> {{0}}, MeshFunctions -> {EHmodes[#] &}];];

(*Declare the functions that finds
the effective indices within a range range*)
roots =.;
SetSharedVariable[rootsHE];
SetSharedVariable[rootsEH];
findModeSolutionHE[nefflow_, neffhigh_, wavelength_, lorder_, nout_] :=
  Block[{n1, n2, λ, rootsHE, 1, n3},
    n3 = nout;
    1 = lorder;
    λ = wavelength;
    n1 = ncore[λ];
    n2 = nclad[λ];
    rootsHE = {};

```

```

MapThread[modePlotsHE, {{nefflow}, {neffhigh}}];
seeds = Cases[Normal[pHE], Point[z_]  $\Rightarrow$  z[[1]],  $\infty$ ];
rootsHE = Reap[Sow[Table[
    x /. FindRoot[Re[HEmodes[x]], {x, s}, AccuracyGoal  $\rightarrow$  8], {s, seeds}]]];
rootsHE = Select[Sort[Flatten[rootsHE]]  $\cup$  {SameTest  $\rightarrow$  (Re[#1 - #2]  $< 10^{-7}$  &)},
    Re[#]  $\leq$  n2 &];
Return[rootsHE];
]

```

```

findModeSolutionEH[nefflow_, neffhigh_, wavelength_, lorder_, nout_] :=
Block[{n1, n2,  $\lambda$ , rootsEH, l, n3},
    n3 = nout;
    l = lorder;
     $\lambda$  = wavelength;
    n1 = ncore[ $\lambda$ ];
    n2 = nclad[ $\lambda$ ];
    rootsEH = {};
    MapThread[modePlotsEH, {{nefflow}, {neffhigh}}];
    seeds = Cases[Normal[pEH], Point[z_]  $\Rightarrow$  z[[1]],  $\infty$ ];
    rootsEH = Reap[Sow[Table[
        x /. FindRoot[Re[EHmodes[x]], {x, s}, AccuracyGoal  $\rightarrow$  8], {s, seeds}]]];
    rootsEH = Select[Sort[Flatten[rootsEH]]  $\cup$  {SameTest  $\rightarrow$  (Re[#1 - #2]  $< 10^{-7}$  &)},
        Re[#]  $\leq$  n2 &];
    Return[rootsEH];
]

```

```

(*CouplingHybrid[lnumber, wavelength, neff, indexout, PorS]
returns coupling coefficient of a hybrid mode*)
(*l = lnumber,  $\lambda$  = wavelength in  $\mu\text{m}$ , neff = neff, clad, indexout = n3,
PorS = "p" or "s" of the core mode polarization*)
CouplingHybrid[lnumber_, wavelength_, neff_, indexout_, PorS_] :=
Module[{Kg,  $\theta$ , a1, a2,  $\Lambda$ ,  $\xi_0$ ,  $\sigma_1$ ,  $\sigma_2$ ,
    u1, u2, u21, w3, l = lnumber,
     $\lambda$  = wavelength, n3 = indexout, n1,
    n2, u32, J, K, p1, q1, r1, s1, u0,
    w0, Ec1lvP, Ec1lvS, U, W, n, B2,
    Ercore, Hrcore, E $\phi$ core, H $\phi$ core,
    Erclad, Hrclad, E $\phi$ clad, H $\phi$ clad },
    n1 = ncore[ $\lambda$ ]; n2 = nclad[ $\lambda$ ]; neffcore = coreModeIndex[ $\lambda$ ];

```

```

Kg =  $\frac{\pi}{\Lambda}$ ;
 $\theta = 10$  Degree;
a1 = 4.1; a2 = 62.5; Z0 = 377;

 $\Lambda = N\left[\frac{1.604}{2 \text{ coreModeIndex}[1.604]}\right][[1]]$ ; (*set the Bragg at 1.586*)

 $\xi_0[x_] := \left( p_1[x, a_2] u_2[x] \left( J[x] K[x] + \frac{u_{21}[x] u_{32}[x] \sigma_1[x] \sigma_2[x]}{a_1 a_2 n_2^2} \right) \right.$ 
 $\quad \left. + q_1[x, a_2] (-K[x]) + J[x] r_1[x, a_2] - \frac{s_1[x, a_2]}{u_2[x]} \right) /$ 
 $\left( \sigma_2[x] \left( p_1[x, a_2] (-u_2[x]) \left( \frac{J[x] u_{32}[x]}{a_2 n_2^2} - \frac{u_{21}[x] K[x]}{a_1 n_1^2} \right) \right. \right.$ 
 $\quad \left. \left. + \frac{r_1[x, a_2] u_{21}[x]}{a_1 n_1^2} + \frac{q_1[x, a_2] u_{32}[x]}{a_2 n_1^2} \right) \right)$ ;

 $\sigma_1[x_] := (i \, 1 \, x) / Z_0$ ;
 $\sigma_2[x_] := i \, 1 \, x \, Z_0$ ;
 $u_1[x_] := \sqrt{((2 \pi) / \lambda)^2 (n_1^2 - x^2)}$ ;
 $u_2[x_] := \sqrt{((2 \pi) / \lambda)^2 (n_2^2 - x^2)}$ ;
 $w_3[x_] := \sqrt{((2 \pi) / \lambda)^2 (x^2 - n_3^2)}$ ;
 $u_{32}[x_] := \left( \frac{1}{u_2[x]^2} + \frac{1}{w_3[x]^2} \right)$ ;
 $u_{21}[x_] := \frac{1}{u_2[x]^2} - \frac{1}{u_1[x]^2}$ ;
J[x_] := DBesselJ[1, a1 u1[x]] / (u1[x] BesselJ[1, u1[x] a1]);
K[x_] := DBesselK[1, a2 w3[x]] / (w3[x] BesselK[1, w3[x] a2]);
DBesselJ[1_, arg_] = 1 / 2 (BesselJ[-1 + 1, arg] - BesselJ[1 + 1, arg]);
DBesselK[1_, arg_] = 1 / 2 (-BesselK[-1 + 1, arg] - BesselK[1 + 1, arg]);
DBesselY[1_, arg_] = 1 / 2 (BesselY[-1 + 1, arg] - BesselY[1 + 1, arg]);
p1[x_, r_] := BesselY[1, u2[x] a1] BesselJ[1, u2[x] r] -
BesselJ[1, u2[x] a1] BesselY[1, u2[x] r];
q1[x_, r_] := BesselJ[1, u2[x] r] DBesselY[1, a1 u2[x]] -
BesselY[1, u2[x] r] DBesselJ[1, a1 u2[x]];
r1[x_, r_] := BesselY[1, u2[x] a1] DBesselJ[1, r u2[x]] -
BesselJ[1, u2[x] a1] DBesselY[1, r u2[x]];
s1[x_, r_] := DBesselY[1, a1 u2[x]] DBesselJ[1, r u2[x]] -
DBesselJ[1, a1 u2[x]] DBesselY[1, r u2[x]];
F2[x_] := J[x] -  $\frac{u_{21}[x] \sigma_2[x] \xi_0[x]}{n_1^2 a_1}$ ;
G2[x_] :=  $\xi_0[x] J[x] + \frac{u_{21}[x] \sigma_1[x]}{a_1}$ ;

```

```

G3[x_] := - $\frac{n3^2}{n2^2} \left( G2[x] p1[x, a2] - \frac{n2^2 \zeta0[x]}{n1^2 u2[x]} q1[x, a2] \right);$ 

F3[x_] := -F2[x] p1[x, a2] +  $\frac{1}{u2[x]}$  q1[x, a2];

c = (Cos[l  $\phi$ ])2;
s = (Sin[l  $\phi$ ])2;

Ercl_core[x_] :=  $\frac{1 \text{ BesselJ}[1, r u1[x]]}{r} + \frac{u1[x] \zeta0[x] \sigma2[x] \text{DBesselJ}[1, r u1[x]]}{1 n1^2}$ ;

E $\phi$ cl_core[x_] :=  $\left( -\frac{\zeta0[x] \sigma2[x] \text{BesselJ}[1, r u1[x]]}{n1^2 r} - u1[x] \text{DBesselJ}[1, r u1[x]] \right)$ ;

Hrcl_core[x_] :=  $\left( \frac{1 \zeta0[x] \text{BesselJ}[1, r u1[x]]}{r} - \frac{1 u1[x] \sigma1[x] \text{DBesselJ}[1, r u1[x]]}{1} \right)$ ;

H $\phi$ cl_core[x_] :=  $-\left( \frac{1 \sigma1[x] \text{BesselJ}[1, r u1[x]]}{r} - u1[x] 1 \zeta0[x] \text{DBesselJ}[1, r u1[x]] \right)$ ;

pltermsP[x_] = Evaluate[ $\left( \text{Ercl\_core}[x] \left( \pi + \frac{\text{Sin}[4 l \pi]}{4 l} \right) \text{Conjugate}[\text{H}\phi\text{cl\_core}[x]] \right.$ 
-  $\left. \text{Conjugate}[\text{Hrcl\_core}[x]] \text{E}\phi\text{cl\_core}[x] \left( \pi - \frac{\text{Sin}[4 l \pi]}{4 l} \right) \right) r$ ];

pltermsS[x_] = Evaluate[ $\left( \text{Ercl\_core}[x] \left( \pi - \frac{\text{Sin}[4 l \pi]}{4 l} \right) \text{Conjugate}[\text{H}\phi\text{cl\_core}[x]] \right.$ 
-  $\left. \text{Conjugate}[\text{Hrcl\_core}[x]] \text{E}\phi\text{cl\_core}[x] \left( \pi + \frac{\text{Sin}[4 l \pi]}{4 l} \right) \right) r$ ];

PlP[x_] :=  $\frac{1}{2} \text{Re}[\text{NIntegrate}[pltermsP[x], \{r, 0, a1\},$ 
Method  $\rightarrow \{$  "GlobalAdaptive",
Method  $\rightarrow$  "GaussKronrodRule", "SingularityDepth"  $\rightarrow$  Infinity  $\}]]$ ;

PlS[x_] :=  $\frac{1}{2} \text{Re}[\text{NIntegrate}[pltermsS[x], \{r, 0, a1\},$ 
Method  $\rightarrow \{$  "GlobalAdaptive",
Method  $\rightarrow$  "GaussKronrodRule", "SingularityDepth"  $\rightarrow$  Infinity  $\}]]$ ;

Ercl_clad[x_] :=  $\text{BesselJ}[1, a1 u1[x]] \left( -\frac{a1 F2[x] 1 \pi u1[x]^2 p1[x, r]}{2 r} + \frac{a1 1 \pi u1[x]^2 q1[x, r]}{2 r u2[x]} \right.$ 
-  $\left. \frac{a1 G2[x] \pi u1[x]^2 u2[x] \sigma2[x] r1[x, r]}{2 1 n2^2} + \frac{a1 \pi u1[x]^2 \zeta0[x] \sigma2[x] s1[x, r]}{2 1 n1^2} \right)$ ;

E $\phi$ cl_clad[x_] := BesselJ[1, a1 u1[x]]

```

$$\left(\frac{a1 G2[x] \pi u1[x]^2 \sigma2[x] p1[x, r]}{2 n2^2 r} - \frac{a1 \pi u1[x]^2 \zeta0[x] \sigma2[x] q1[x, r]}{2 n1^2 r u2[x]} + \frac{1}{2} a1 F2[x] \pi u1[x]^2 u2[x] r1[x, r] - \frac{1}{2} a1 \pi u1[x]^2 s1[x, r] \right);$$

$$Hrcl_{clad}[x_] :=$$

$$a1 \pi u1[x]^2 BesselJ[1, a1 u1[x]] \left(-\frac{i G2[x] l p1[x, r]}{2 r} + \frac{i l n2^2 \zeta0[x] q1[x, r]}{2 n1^2 r u2[x]} + \frac{i F2[x] u2[x] \sigma1[x] r1[x, r]}{2 l} - \frac{i \sigma1[x] s1[x, r]}{2 l} \right);$$

$$H\phi cl_{clad}[x_] := -\frac{1}{2} a1 \pi u1[x]^2 BesselJ[1, a1 u1[x]] \left(-\frac{F2[x] l \sigma1[x] p1[x, r]}{r} + \frac{l \sigma1[x] q1[x, r]}{r u2[x]} + i G2[x] u2[x] r1[x, r] - \frac{n2^2 l \zeta0[x] s1[x, r]}{n1^2} \right);$$

$$p2termsP[x_] := Evaluate \left[\left(Ercl_{clad}[x] \left(\pi + \frac{\sin[4 l \pi]}{4 l} \right) Conjugate[H\phi cl_{clad}[x]] - Conjugate[Hrcl_{clad}[x]] E\phi cl_{clad}[x] \left(\pi - \frac{\sin[4 l \pi]}{4 l} \right) \right) r \right];$$

$$p2termsS[x_] := Evaluate \left[\left(Ercl_{clad}[x] \left(\pi - \frac{\sin[4 l \pi]}{4 l} \right) Conjugate[H\phi cl_{clad}[x]] - Conjugate[Hrcl_{clad}[x]] E\phi cl_{clad}[x] \left(\pi + \frac{\sin[4 l \pi]}{4 l} \right) \right) r \right];$$

$$P2P[x_] := \frac{1}{2} \text{Re}[NIntegrate[p2termsP[x], \{r, a1, a2\},$$

$$\text{Method} \rightarrow \{\text{"GlobalAdaptive"},$$

$$\text{Method} \rightarrow \text{"GaussKronrodRule"}, \text{"SingularityDepth"} \rightarrow \text{Infinity}\}\}\];$$

$$P2S[x_] := \frac{1}{2} \text{Re}[NIntegrate[p2termsS[x], \{r, a1, a2\},$$

$$\text{Method} \rightarrow \{\text{"GlobalAdaptive"},$$

$$\text{Method} \rightarrow \text{"GaussKronrodRule"}, \text{"SingularityDepth"} \rightarrow \text{Infinity}\}\}\];$$

$$Ercl_{out}[x_] :=$$

$$\left(a1 \pi u1[x]^2 u2[x]^2 BesselJ[1, a1 u1[x]] \left(-\frac{F3[x] l BesselK[1, r w3[x]]}{2 r w3[x]^2} - \frac{G3[x] \sigma2[x] DBesselK[1, r w3[x]]}{2 l n3^2 w3[x]} \right) \right) / BesselK[1, a2 w3[x]];$$

$$E\phi cl_{out}[x_] :=$$

$$\left(a1 \pi u1[x]^2 u2[x]^2 BesselJ[1, a1 u1[x]] \left(\frac{G3[x] \sigma2[x] BesselK[1, r w3[x]]}{2 n3^2 r w3[x]^2} + \frac{F3[x] DBesselK[1, r w3[x]]}{2 w3[x]} \right) \right) / BesselK[1, a2 w3[x]];$$


```

Hrc1_out[x_] :=
  (a1 π u1[x]^2 u2[x]^2 BesselJ[1, a1 u1[x]] (
    -  $\frac{i G3[x] I BesselK[1, r w3[x]]}{2 r w3[x]^2}$ 
    +  $\frac{i F3[x] \sigma1[x] DBesselK[1, r w3[x]]}{2 I w3[x]}$ 
  )) / BesselK[1, a2 w3[x]];

Hφcl_out[x_] :=
  - (a1 π u1[x]^2 u2[x]^2 BesselJ[1, a1 u1[x]] (
    -  $\frac{F3[x] I \sigma1[x] BesselK[1, r w3[x]]}{2 r w3[x]^2}$ 
    +  $\frac{I G3[x] DBesselK[1, r w3[x]]}{2 w3[x]}$ 
  )) / BesselK[1, a2 w3[x]];

p3termsP[x_] := Evaluate[
  (Ercl_out[x] (π +  $\frac{\sin[4 I \pi]}{4 I}$ ) Conjugate[Hφcl_out[x]]
  - Conjugate[Hrc1_out[x]] Eφcl_out[x] (π -  $\frac{\sin[4 I \pi]}{4 I}$ )) r];

p3termsS[x_] := Evaluate[
  (Ercl_out[x] (π -  $\frac{\sin[4 I \pi]}{4 I}$ ) Conjugate[Hφcl_out[x]]
  - Conjugate[Hrc1_out[x]] Eφcl_out[x] (π +  $\frac{\sin[4 I \pi]}{4 I}$ )) r];

P3P[x_] :=  $\frac{1}{2}$  Re[NIntegrate[p3termsP[x], {r, a2, ∞},
  Method → {"GlobalAdaptive",
    Method → "GaussKronrodRule", "SingularityDepth" → Infinity}]];

P3S[x_] :=  $\frac{1}{2}$  Re[NIntegrate[p3termsS[x], {r, a2, ∞},
  Method → {"GlobalAdaptive",
    Method → "GaussKronrodRule", "SingularityDepth" → Infinity}]];

u0 =  $\sqrt{\left(\frac{2 \pi}{\lambda}\right)^2 (n1^2 - neffcore^2)}$ ;

Ec11vP[x_] :=  $\sqrt{\frac{1}{P1P[x] + P2P[x] + P3P[x]}}$ ;

Ec11vS[x_] :=  $\sqrt{\frac{1}{P1S[x] + P2S[x] + P3S[x]}}$ ;

(*core mode normalization calculation in HE11 mode*)
(*core mode field description x polarized*)

w0 =  $\sqrt{\left(\frac{2 \pi}{\lambda}\right)^2 (neffcore^2 - n2^2)}$ ;

U = u0 a1;

```

```

W = w0 a1;
n = n1;
B2 =  $\left( -\frac{U^2 \text{BesselJ}[1, U]}{W^2 \text{BesselK}[1, W]} \right) (*A1*)$ ;

Ercore = u0 BesselJ[0, u0 r] ;
Eφcore = - u0 BesselJ[0, u0 r] ;
Hrcore =  $\frac{n1}{Z0}$  u0 BesselJ[0, u0 r];
Hφcore =  $\frac{n1}{Z0}$  u0 BesselJ[0, u0 r];

Erclad = B2 w0 (-BesselK[0, w0 r]) ;
Eφclad = - B2 w0 (- BesselK[0, w0 r]) ;
Hrclad =  $\frac{n2}{Z0}$  B2 w0 (- BesselK[0, w0 r]);
Hφclad =  $\frac{n2}{Z0}$  B2 w0 (- BesselK[0, w0 r]);

integrationTermP[x_] := ( Ercore Cos[φ] Erclcore[x] Cos[1 φ]
+ Eφcore Sin[φ] Eφclcore[x] Sin[1 φ] ) r Exp[+2 I Kg r Cos[φ] Sin[θ]];

gclminusP[x_] :=  $\frac{\pi}{4 \lambda Z0}$  n1 E0lcoExact Ec1lvP[x]
NIntegrate[integrationTermP[x], {r, 0, a1}, {φ, 0, 2 π},
Method → {"GlobalAdaptive",
Method → "GaussKronrodRule", "SingularityDepth" → Infinity}];

integrationTermS[x_] :=  $\left( \text{Ercore Cos}\left[\phi + \frac{\pi}{2}\right] \text{Erclcore}[x] \text{Cos}\left[1 \phi + \frac{\pi}{2}\right] \right.$ 
 $\left. + \text{E}\phi\text{core Sin}\left[\phi + \frac{\pi}{2}\right] \text{E}\phi\text{clcore}[x] \text{Sin}\left[1 \phi + \frac{\pi}{2}\right] \right) r \text{Exp}[+2 I Kg r \text{Cos}[\phi] \text{Sin}[\theta]]$ ;

gclminusS[x_] :=  $\frac{\pi}{4 \lambda Z0}$  n1 Ec1lvS[x] E0lcoExact NIntegrate[
integrationTermS[x], {r, 0, a1}, {φ, 0, 2 π}, Method → {"GlobalAdaptive",
Method → "GaussKronrodRule", "SingularityDepth" → Infinity}];

Pcoremode =
 $\frac{1}{2} \text{Re}\left[\text{NIntegrate}\left[\left(\text{Ercore H}\phi\text{core Cos}[\phi]^2 - \text{Hrcore E}\phi\text{core Sin}[\phi]^2\right) r, \{\phi, 0, 2 \pi\}, \right.\right.$ 
 $\left.\left.\{r, 0, a1\}, \text{Method} \rightarrow \{\text{"GlobalAdaptive"}, \text{Method} \rightarrow \text{"GaussKronrodRule"}, \right.\right.$ 
 $\left.\left.\text{"SingularityDepth"} \rightarrow \text{Infinity}\right]\right] +$ 
 $\frac{1}{2} \text{Re}\left[\text{NIntegrate}\left[\left(\text{Erclad H}\phi\text{clad Cos}[\phi]^2 - \text{Hrclad E}\phi\text{clad Sin}[\phi]^2\right) r,$ 

```

```

    {φ, 0, 2 π}, {r, a1, a2}, Method → {"GlobalAdaptive",
      Method → "GaussKronrodRule", "SingularityDepth" → Infinity}]]];

E0lcoExact =  $\sqrt{\frac{1}{P_{\text{coremode}}}}$ ; (*note E0lcoExact* u0 = E0lco*)

If[PorS == ToString[p], Return[gclminusP[neff]], Return[gclminusS[neff]]];
SetAttributes[CouplingHybrid, Listable];

(*couplingCoefficientTE[λC, lorder, neff, indexout]
  returns coupling coefficient of a TE mode*)
(*l = 0, λC= wavelength in μm, neff = neff, clad, indexout = n3,
  only works assuming core mode is S polarized*)
couplingCoefficientTE[λC_, lorder_, neff_, indexout_] := Block[{l = lorder, λ = λC,
  n3 = indexout, n1, n2, neffcore,
  u1, u2, w3, u32, u21, J, K,
  p1, q1, r1, s1, P1, P2, P3, P,
  E0vte, u0, w0, U, W, n, B2, Pcoremode},

  u1[x_] :=  $\sqrt{((2 \pi) / \lambda)^2 (n1^2 - x^2)}$ ;
  u2[x_] :=  $\sqrt{((2 \pi) / \lambda)^2 (n2^2 - x^2)}$ ;
  w3[x_] :=  $\sqrt{((2 \pi) / \lambda)^2 (x^2 - n3^2)}$ ;
  u32[x_] :=  $\left( \frac{1}{u2[x]^2} + \frac{1}{w3[x]^2} \right)$ ;
  u21[x_] :=  $\frac{1}{u2[x]^2} - \frac{1}{u1[x]^2}$ ;
  J[x_] := DBesselJ[1, a1 u1[x]] / (u1[x] BesselJ[1, u1[x] a1]);
  K[x_] := DBesselK[1, a2 w3[x]] / (w3[x] BesselK[1, w3[x] a2]);
  DBesselJ[1_, arg_] = 1 / 2 (BesselJ[-1 + 1, arg] - BesselJ[1 + 1, arg]);
  DBesselK[1_, arg_] = 1 / 2 (-BesselK[-1 + 1, arg] - BesselK[1 + 1, arg]);
  DBessely[1_, arg_] = 1 / 2 (Bessely[-1 + 1, arg] - Bessely[1 + 1, arg]);
  p1[x_, r_] :=
    Bessely[0, u2[x] a1] BesselJ[0, u2[x] r] - BesselJ[0, u2[x] a1] Bessely[0, u2[x] r];
  q1[x_, r_] := BesselJ[0, u2[x] r] DBessely[0, a1 u2[x]] -
    Bessely[0, u2[x] r] DBesselJ[0, a1 u2[x]];
  r1[x_, r_] := Bessely[0, u2[x] a1] DBesselJ[0, r u2[x]] -
    BesselJ[0, u2[x] a1] DBessely[0, r u2[x]];
  s1[x_, r_] := DBessely[0, a1 u2[x]] DBesselJ[0, r u2[x]] -
    DBesselJ[0, a1 u2[x]] DBessely[0, r u2[x]];
  a1 = 4.1; a2 = 62.5; (*use SMF 28 value*)
  n1 = ncore[λC]; n2 = nclad[λC];
  Z0 = 377.0;
  θ = 10 Degree;

```

```

neffcore = coreModeIndex[λC];
Λ = N[ $\frac{1.604}{2 \text{ coreModeIndex}[1.604]}$ ] [[1]]; (*period in nm*)
Kg =  $\frac{\pi}{\Lambda}$ ;
Ertecore[x_] := 0;
Eφtecore[x_] := -u1[x] DBesselJ[0, u1[x] r];
Hrtecore[x_] := u1[x]  $\frac{x}{Z0}$  (DBesselJ[0, u1[x] r]);
Erteclad[x_] := 0;
Eφteclad[x_] :=
 $\frac{1}{2} a1 \pi u1[x]^2 \text{BesselJ}[0, a1 u1[x]] (J[x] u2[x] r1[x, r] - s1[x, r])$ ;
Hrteclad[x_] := - $\frac{1}{2 Z0} a1 x \pi u1[x]^2 \text{BesselJ}[0, a1 u1[x]]$ 
(J[x] u2[x] r1[x, r] - s1[x, r]);
Erteouter[x_] := 0;
Eφteouter[x_] := - (a1 π u1[x]^2 u2[x] BesselJ[0, a1 u1[x]] (J[x] u2[x] p1[x, a2]
- q1[x, a2]) DBesselK[0, rw3[x]]) / (2 w3[x] BesselK[0, a2 w3[x]]);
Hrteouter[x_] := (a1 x π u1[x]^2 u2[x] BesselJ[0, a1 u1[x]] (J[x] u2[x] p1[x, a2]
- q1[x, a2]) DBesselK[0, rw3[x]]) / (2 w3[x] Z0 BesselK[0, a2 w3[x]]);
P1[x_] :=
 $\frac{1}{2} \text{Re}[\text{NIntegrate}[\text{Integrate}[-\text{Conjugate}[\text{Hrtecore}[x]] \text{Eφtecore}[x] r, \{\phi, 0, 2 \pi\}],$ 
{r, 0, a1}, Method → {"GlobalAdaptive",
Method → "GaussKronrodRule", "SingularityDepth" → Infinity}]]];
P2[x_] :=  $\frac{1}{2} \text{Re}[\text{NIntegrate}[\text{Integrate}[-\text{Conjugate}[\text{Hrteclad}[x]] \text{Eφteclad}[x] r,$ 
{φ, 0, 2 π}], {r, a1, a2}, Method → {"GlobalAdaptive",
Method → "GaussKronrodRule", "SingularityDepth" → Infinity}]]];
P3[x_] :=  $\frac{1}{2}$ 
Re[NIntegrate[Integrate[-Conjugate[Hrteouter[x]] Eφteouter[x] r, {φ, 0, 2 π}],
{r, a2, ∞}, Method → {"GlobalAdaptive", Method → "GaussKronrodRule",
"SingularityDepth" → Infinity}]]];
P[x_] := P1[x] + P2[x] + P3[x];
EOvte[x_] :=  $\frac{1}{\sqrt{P1[x + I 0.] + P2[x + I 0.0] + P3[x + I 0.0]}}$ ;
u0 =  $\sqrt{((2 \pi) / \lambda)^2 (n1^2 - \text{neffcore}^2)}$ ;
w0 =  $\sqrt{\left(\frac{2 \pi}{\lambda}\right)^2 (\text{neffcore}^2 - n2^2)}$ ;
U = u0 a1;
W = w0 a1;

```

```

n = n1;

B2 =  $\left( -\frac{U^2 \text{BesselJ}[1, U]}{W^2 \text{BesselK}[1, W]} \right) (*A1*)$ ;

Ercore = u0 (*A1*) BesselJ[0, u0 r];
Eφcore = - u0 (*A1*) BesselJ[0, u0 r];
Hrcore =  $\frac{n1}{Z0}$  u0 (*A1*) BesselJ[0, u0 r];
Hφcore =  $\frac{n1}{Z0}$  u0 (*A1*) BesselJ[0, u0 r];

Erclad = B2 w0 (-BesselK[0, w0 r]);
Eφclad = - B2 w0 (-BesselK[0, w0 r]);
Hrclad =  $\frac{n1}{Z0}$  B2 w0 (-BesselK[0, w0 r]);
Hφclad =  $\frac{n1}{Z0}$  B2 w0 (-BesselK[0, w0 r]);

Pcoremode =
 $\frac{1}{2} \text{Re}[\text{NIntegrate}[(\text{Ercore Hφcore Cos}[\phi]^2 - \text{Hrcore Eφcore Sin}[\phi]^2) r, \{\phi, 0, 2\pi\},$ 
     $\{r, 0, a1\}, \text{Method} \rightarrow \{\text{"GlobalAdaptive"}, \text{Method} \rightarrow \text{"GaussKronrodRule"},$ 
     $\text{"SingularityDepth"} \rightarrow \text{Infinity}\}]] +$ 
 $\frac{1}{2} \text{Re}[\text{NIntegrate}[(\text{Erclad Hφclad Cos}[\phi]^2 - \text{Hrclad Eφclad Sin}[\phi]^2) r,$ 
     $\{\phi, 0, 2\pi\}, \{r, a1, a2\}, \text{Method} \rightarrow \{\text{"GlobalAdaptive"},$ 
     $\text{Method} \rightarrow \text{"GaussKronrodRule"}, \text{"SingularityDepth"} \rightarrow \text{Infinity}\}]]];$ 

E0lcoExact =  $\sqrt{\frac{1}{\text{Pcoremode}}}$ ;

integrationTermTEs[x_] :=  $\left( \text{Ercore Cos}\left[\phi + \frac{\pi}{2}\right] \text{Ertecore}[x] \right.$ 
     $\left. + \text{Eφcore Sin}\left[\phi + \frac{\pi}{2}\right] \text{Eφtecore}[x] \right) r \text{Exp}[+2 \text{I Kg } r \text{Cos}[\phi] \text{Sin}[\theta]];$ 

gclminusTEs[x_] :=
 $\frac{\pi}{4 \lambda Z0} n1 \text{E0lcoExact E0vte}[x] \text{NIntegrate}[\text{integrationTermTEs}[x],$ 
     $\{\phi, 0, 2\pi\}, \{r, 0, a1\}, \text{Method} \rightarrow \{\text{"GlobalAdaptive"},$ 
     $\text{Method} \rightarrow \text{"GaussKronrodRule"}, \text{"SingularityDepth"} \rightarrow \text{Infinity}\}];$ 
Return[gclminusTEs[neff]];

```

```
(*couplingCoefficientTM[λC, lorder, neff, indexout]
```

```

returns coupling coefficient of a TM mode*)
(*l = 0, λC= wavelength in μm, neff = neff, clad, indexout = n3,
only works assuming core mode is P polarized*)
couplingCoefficientTM[λC_, lorder_, neff_, indexout_] := Block[{l = lorder, λ = λC,
  n3 = indexout, n1, n2, neffcore, u1, u2,
  w3, u32, u21, J, K, p1, q1, r1, s1,
  P1, P2, P3, P, E0vte, u0, w0, U, W,
  n, B2, Pcoremode },

u1[x_] :=  $\sqrt{((2\pi)/\lambda)^2 (n1^2 - x^2)}$ ;
u2[x_] :=  $\sqrt{((2\pi)/\lambda)^2 (n2^2 - x^2)}$ ;
w3[x_] :=  $\sqrt{((2\pi)/\lambda)^2 (x^2 - n3^2)}$ ;
J[x_] := DBesselJ[0, a1 u1[x]] / (u1[x] BesselJ[0, u1[x] a1]);
K[x_] := DBesselK[0, a2 w3[x]] / (w3[x] BesselK[0, w3[x] a2]);
DBesselJ[l_, arg_] = 1/2 (BesselJ[-1+l, arg] - BesselJ[1+l, arg]);
DBesselK[l_, arg_] = 1/2 (-BesselK[-1+l, arg] - BesselK[1+l, arg]);
DBesselY[l_, arg_] = 1/2 (BesselY[-1+l, arg] - BesselY[1+l, arg]);
p1[x_, r_] :=
  BesselY[0, u2[x] a1] BesselJ[0, u2[x] r] - BesselJ[0, u2[x] a1] BesselY[0, u2[x] r];
q1[x_, r_] := BesselJ[0, u2[x] r] DBesselY[0, a1 u2[x]] -
  BesselY[0, u2[x] r] DBesselJ[0, a1 u2[x]];
r1[x_, r_] := BesselY[0, u2[x] a1] DBesselJ[0, r u2[x]] -
  BesselJ[0, u2[x] a1] DBesselY[0, r u2[x]];
s1[x_, r_] := DBesselY[0, a1 u2[x]] DBesselJ[0, r u2[x]] -
  DBesselJ[0, a1 u2[x]] DBesselY[0, r u2[x]];
Ertmcore[x_] := - $\frac{x u1[x] Z0 DBesselJ[0, r u1[x]]}{n1^2}$ ;
(*-multiplier[x]  $\frac{x Z0}{n1^2}$  u1[x] DBesselJ[0, u1[x] r];*)
Eφtmcore[x_] := 0;
Hφtmcore[x_] := - u1[x] DBesselJ[0, u1[x] r];
Ertmclad[x_] :=  $\frac{1}{2 n1^2 n2^2}$ 
  a1 x π u1[x]^2 Z0 BesselJ[0, a1 u1[x]] (J[x] n1^2 u2[x] r1[x, r] - n2^2 s1[x, r]);
Eφtmclad[x_] := 0;
Hφtmclad[x_] :=
   $\frac{1}{2 n1^2}$  a1 π u1[x]^2 BesselJ[0, a1 u1[x]] (J[x] n1^2 u2[x] r1[x, r] - n2^2 s1[x, r]);
Ertmouter[x_] := (a1 x π u1[x]^2 Z0 BesselJ[0, a1 u1[x]] (J[x] n1^2 u2[x] r1[x, a2]
  - n2^2 s1[x, a2]) DBesselK[0, r w3[x]]) /
  (2 K[x] n1^2 n3^2 w3[x] BesselK[0, a2 w3[x]]);
Eφtmouter[x_] := 0;
Hφtmouter[x_] := (a1 π u1[x]^2 BesselJ[0, a1 u1[x]] (J[x] n1^2 u2[x] r1[x, a2]
  - n2^2 s1[x, a2]) DBesselK[0, r w3[x]]) /
  (2 K[x] n1^2 w3[x] BesselK[0, a2 w3[x]]);

```

```

P1[x_] :=  $\frac{1}{2}$  Re[NIntegrate[Integrate[Ertmcore[x] Conjugate[Høtmcore[x]] r,
    {φ, 0, 2 π}], {r, 0, a1}, Method → "GaussKronrodRule"]];
P2[x_] :=  $\frac{1}{2}$  Re[NIntegrate[Integrate[Ertmclad[x] Conjugate[Høtmclad[x]] r,
    {φ, 0, 2 π}], {r, a1, a2}, Method → "GaussKronrodRule"]];
P3[x_] :=  $\frac{1}{2}$  Re[NIntegrate[Integrate[Ertmouter[x] Conjugate[Høtmouter[x]] r,
    {φ, 0, 2 π}], {r, a2, ∞}, Method → "GaussKronrodRule"]];
P[x_] := P1[x] + P2[x] + P3[x];
E0vtm[x_] :=  $\frac{1}{\sqrt{P1[x + I 0.] + P2[x + I 0.] + P3[x + I 0.]}}$ ;
a1 = 4.15; a2 = 62.5; (*use SMF 28 value*)
n1 = ncore[λC]; n2 = nclad[λC];
Z0 = 377.0;
θ = 10 Degree;
neffcore = coreModeIndex[λC];
Λ = N[ $\frac{1.604}{2 \text{ coreModeIndex}[1.604]}$ ] [[1]]; (*period in nm*)
Kg =  $\frac{\pi}{\Lambda}$ ;
u0 =  $\sqrt{\left(\frac{2 \pi}{\lambda}\right)^2 (n1^2 - \text{neffcore}^2)}$ ;
(*core mode normalization calculation in HE11 mode*)
(*core mode field description x polarized*)
w0 =  $\sqrt{\left(\frac{2 \pi}{\lambda}\right)^2 (\text{neffcore}^2 - n2^2)}$ ;
U = u0 a1;
W = w0 a1;
n = n1;
B2 =  $\left(-\frac{U^2 \text{BesselJ}[1, U]}{W^2 \text{BesselK}[1, W]}\right) (*A1*)$ ;
Ercore = u0 (*A1*) BesselJ[0, u0 r];
Eφcore = - u0 (*A1*) BesselJ[0, u0 r];
Hrcore =  $\frac{n1}{Z0}$  u0 (*A1*) BesselJ[0, u0 r];
Hφcore =  $\frac{n1}{Z0}$  u0 (*A1*) BesselJ[0, u0 r];
Erclad = B2 w0 (-BesselK[0, w0 r]);
Eφclad = - B2 w0 (-BesselK[0, w0 r]);

```

```

Hrclad =  $\frac{n1}{Z0}$  B2 w0 (- BesselK[0, w0 r]);
Hφclad =  $\frac{n1}{Z0}$  B2 w0 (- BesselK[0, w0 r]);

Pcoremode =
 $\frac{1}{2}$  Re[NIntegrate[(Ercore Hφcore Cos[φ]2 - Hrcore Eφcore Sin[φ]2) r, {φ, 0, 2 π},
  {r, 0, a1}, Method → {"GlobalAdaptive", Method → "GaussKronrodRule",
    "SingularityDepth" → Infinity}]] +
 $\frac{1}{2}$  Re[NIntegrate[(Erclad Hφclad Cos[φ]2 - Hrclad Eφclad Sin[φ]2) r,
  {φ, 0, 2 π}, {r, a1, a2}, Method → {"GlobalAdaptive",
    Method → "GaussKronrodRule", "SingularityDepth" → Infinity}]];

E0lcoExact =  $\sqrt{\frac{1}{Pcoremode}}$ ;
integrationTermTMp[x_] := (Ercore Cos[φ] Ertmcore[x] +
  Eφcore Sin[φ] Eφtmcore[x])
  r Exp[+2 I Kg r Cos[φ] Sin[θ]];
gclminusTMp[x_] :=  $\frac{\pi}{(4 \lambda Z0)}$  n1 E0lcoExact E0vtm[x + I 0.] NIntegrate[
  integrationTermTMp[x], {φ, 0, 2 π}, {r, 0, a1}, Method → {"GlobalAdaptive",
    Method → "GaussKronrodRule", "SingularityDepth" → Infinity}];
Return[gclminusTMp[neff]];

```